

MONITORING THE GALACTIC CENTER AT 3MM
Study of Flaring of Sagittarius A* and SiO Masers in the Central Parsec

INAUGURAL-DISSERTATION

zur
Erlangung des Doktorgrades
der Mathematisch-Naturwissenschaftlichen Fakultät
der Universität zu Köln



vorgelegt von

ABHIJEET PRAMOD BORKAR
aus Pune, Indien

Köln 2015

Berichterstatter:

Prof. Dr. Andreas Eckart
Prof. Dr. Anton Zensus

Tag der letzten mündlichen Prüfung: 3 November 2015

ABSTRACT

The center of the Milky Way Galaxy is a complex environment, with a super-massive black hole, Sagittarius A* (Sgr A*), at its heart, which is a bright radio source. It undergoes regular bursts of variability, known as flaring. The flaring is also observed in near-IR and X-ray observations. This flaring activity is thought to arise from the innermost region of the accretion flow. One aim of this thesis is to analyze the observations of the Galactic Center at millimeter wavelength to observe and study the flaring activity of Sgr A*. In part these observations were carried out by myself. For this, I have observed the GC at 3 mm wavelength between 2010–2014 with Australia Telescope Compact Array (ATCA). The observations in 2013 – 2014 were also carried out to study the flyby of the dusty S-cluster object (DSO/G2) that was supposed to have its periape passage in 2014, and its effects on the flaring activity of Sgr A*.

I obtain the radio light curves of Sgr A* from interferometer data by subtracting the contributions from the surrounding extended emission and correcting the elevation and time dependent gains of the telescope. The observations detect three instances of significant variability in the flux density of Sgr A*, with variations between 0.5 to 1.0 Jy, lasting for 1.5 – 3 hours. I use the adiabatically expanding plasmon model to analyze the flux density variations. We derive the physical quantities of the modelled flare emission, which give a source expansion speed of $\nu_{\text{exp}} \sim 0.013 - 0.025 c$, source sizes of $\sim 1 - 3$ Schwarzschild radii, spectral indices of $\alpha_{\text{synch}} = 0.5 - 0.8$, with the peak of the synchrotron radiation occurring at frequencies of few hundred GHz. These parameters suggest that the expanding source components are either confined to the neighbourhood of Sgr A* by contributing to the corona or the disc, or have a bulk motion greater than ν_{exp} . I do not detect exceptional flux density variation on short flare time-scales during the approach and the flyby of the DSO which is consistent with its observed compactness and the absence of a large bow shock.

I also present the observations of SiO maser sources observed in the central parsec of the GC. SgrA* was observed with two intermediate frequencies (IFs) centered at 86.243 GHz and 85.640 GHz corresponding to the two rotational transition lines of the SiO molecule with 2 GHz bandwidth each, and 1 MHz frequency resolution, which corresponds to 3.477 km s^{-1} velocity resolution. Our spatial resolution is limited by the available baselines with best resolution of 0.2arcsec. These are the most comprehensive observations of the central parsec of the GC at 3mm, with wide band that allow us to investigate high velocity stars. In the thesis, I present the method to detect the maser sources. In total, 11 sources were detected, of which 8 are previously known sources, like: IRS 1W, IRS 2L, IRS 7, IRS 9, IRS 10EE, IRS 12N, IRS 28 and IRS 34. Three new sources were detected. I present the method to calculate the accurate positions and proper motions of the maser sources. The proper motions of strong sources IRS 7 & IRS 12N are calculated precisely and are in agreement with previous results. Comparative study of the relative strength of the SiO transition lines indicates that the 86.243 GHz line is stronger than the 85.640 GHz line. Among the detected stars, 3 are cool stars, 2 HE I stars, 1 AGB star and 1 red giant. I also present an upper limit on the detection of several maser sources which have been detected in previous studies but were not detected in my dataset. This is most likely due to the strong variability of the maser emission.

ZUSAMMENFASSUNG

Das Zentrum der Milchstraße stellt eine komplexe Umgebung dar, die in ihrem Zentrum ein supermassives schwarzes Lochs, die helle Radioquelle Sagittarius A* (SgrA*), aufweist. Diese variable Quelle durchläuft regelmäßige Flußdichteausbrüche, die 'flares' genannt werden. Diese Ausbrüche werden auch im nahen Infraroten und im Röntgenbereich beobachtet. Man vermutet, dass diese Flußdichtevariationen aus dem innersten Bereich des Akkretionsstromes auf das schwarze Loch entstehen. Ein Ziel dieser Arbeit ist, die Beobachtungsergebnisse des Galaktischen Zentrums bei Millimeterwellenlängen zu untersuchen und die 'flare'-Aktivität von SgrA* zu studieren. Dafür haben wir zwischen 2010 und 2014 das Galaktische Zentrum bei 3 mm Wellenlänge mit dem Australia Telescope Compact Array (ATCA) beobachtet. Die Beobachtungen in 2013-2014 wurden auch durchgeführt, um den Vorbeiflug des staubigen S-Cluster-Objekt (DSO alias G2) an SgrA* zu studieren. Dessen Periaps-Durchgang wurde für das Jahr 2014 erwartet. Ziel ist auch die möglichen Auswirkungen dieses Ereignisses auf die 'flare'-Aktivität von SgrA* zu analysieren.

Aus den interferometrischen Radiodaten erhalte ich die Lichtkurven von Sgr A* durch Subtraktion der Beiträge der ausgedehnten Emission der Umgebung, sowie durch Korrektur der Elevations- und zeitabhängigen Verstärkungsgewinne des Teleskops. Die Beobachtungen enthalten drei Phasen signifikanter Veränderung der Flussdichte von SgrA*, mit Variationen zwischen 0,5-1,0 Jy, die 1,5 bis 3 Stunden andauern. Ich verwende ein Model eines sich adiabatisch expandierenden Plasmons, um die kurzzeitigen Schwankungen der Flussdichte zu erklären. Dann leite ich die physikalischen Größen der modellierten 'flare'-Emission ab. Hierbei ergibt sich eine typische Expansionsgeschwindigkeit der Quelle von $v_{\text{exp}} \sim 0.013 - 0.025 c$, eine Quellgrößen von etwa einem Schwarzschild-Radius und ein typischer Spektralindex von $\alpha_{\text{synch}} = 0.5 - 0.8$. Der maximale Fluß der Synchrotronstrahlung tritt bei Frequenzen von einigen hundert GHz auf. Diese Parameter implizieren, dass die sich

ausdehnende Quellkomponenten auf die direkte Umgebung von SgrA* beschränkt sind und entweder zu einer Korona oder einer Akkretionsscheibe betragen. Alternativ weisen sie eine Gesamtgeschwindigkeit von mehr als ν_{exp} auf. Während der Annäherung und des Vorbeiflugs des staubigen S-Cluster-Objekts (DSO) wurde keine außergewöhnliche Änderung der Flusssdichte auf kurzen 'flare'-Zeitskalen beobachtet. Dies stimmt mit ihrer Kompaktheit und dem Fehlen einer signifikanten und großen Bugstoßwelle überein.

Ich präsentiere auch die Beobachtungen von SiO Maserquellen, die in dem zentralen Parsek des Galaktischen Zentrums gefunden werden. In meinen Beobachtungen habe ich mit zwei Zwischenfrequenzen (Zfs), zentriert auf 86,243 GHz und 85,640 GHz, entsprechend der beiden Rotationslinienübergänge des SiO-Moleküls, je mit 2-GHz-Bandbreite und 1 MHz Frequenzauflösung beobachtet. Dies entspricht einer Geschwindigkeitsauflösung von 3.477 km s^{-1} . Unsere räumliche Auflösung wird durch die längsten verfügbaren Basislinien auf etwa 0.2 arcsec begrenzt. Damit gehören unsere Beobachtungen zu den umfassendsten, die vom zentralen Parsek des Galaktischen Zentrums bei 3mm mit dieser großen Bandbreite durchgeführt wurden und uns somit die SiO Emission von Sternen mit hohen Geschwindigkeiten untersuchen lassen. In meiner Doktorarbeit, präsentiere ich eine Methode, um die Maserquellen zu erkennen. Insgesamt wurden 10 Quellen erfasst, davon sind 8 bekannten Quellen, nämlich IRS 1W, IRS 2L, IRS 7, IRS 9, IRS 10EE, IRS 12N, IRS 28 und IRS 34. Drei Quellen wurden von mir neu entdeckt. Ich stelle eine Methode vor, um die genauen Positionen und Eigenbewegungen der Maserquellen zu berechnen. Die Eigenbewegungen von starken Quellen, wie IRS 7 und IRS 12N, sind genau berechnet und sind in Übereinstimmung mit früheren Ergebnissen. Eine vergleichende Studie über die relative Stärke der SiO Linienübergänge zeigt, dass die 86,243 GHz Linie stärker als die 85,640 GHz Linie ist. Unter den nachgewiesenen Masersternen sind 3 kühle Sterne, 2 He I Sternen, 1 AGB-Stern und 1 roter Riese. Ich gebe auch eine obere Grenze für den Nachweis mehrerer potentieller Maserquellen an, die in vorherigen Studien gefunden, aber durch meinem Datensatz nicht erfasst wurden. Dies ist vermutlich eine Folge der hohen Variabilität der Maseremission.

CONTENTS

Contents	vii
1 Introduction	1
1.1 The Milky Way	2
1.2 The Center of the Milky Way	5
1.2.1 The Galactic Center Interstellar Medium	5
1.2.2 The Star Clusters	7
1.2.3 Sagittarius A*	10
1.2.4 Flaring of Sgr A*	13
1.3 Outline	14
2 Radio Interferometry, Observations, and Data Reduction	17
2.1 Radio Astronomy	17
2.1.1 Emission mechanisms	18
2.1.2 Thermal emission	19
2.1.3 Non-thermal emission	21
2.1.4 Line emission	23
2.2 Radio Telescopes	24
2.2.1 Interferometry and aperture synthesis	26
2.3 Observations	29
2.3.1 The Telescope	29
2.3.2 Observation details	30
2.3.3 Data reduction	31
3 Breakfast habits of the Beast: Flaring of Sagittarius A*	35
3.1 Introduction	35
3.2 Models	36
3.2.1 The Synchrotron and SSC model	36

3.2.2	The adiabatic expanding plasmon model	38
3.2.3	The Hot Spot model	39
3.2.4	The Jet model	40
3.3	Obtaining the light curves	42
3.4	Results	44
3.4.1	Uncertainties	46
3.4.2	Flare events	46
3.5	Flare analysis	47
3.6	Discussion	50
3.6.1	No detection of DSO-induced activity	50
4	The Villain’s Minions: SiO masers in the Central Parsec	55
4.1	Introduction	55
4.2	Data Analysis	58
4.2.1	Calculating positions and proper motions	58
4.3	Discussion	59
4.3.1	Variability of SiO masers	63
5	Summary	69
A	Appendix	73
	Bibliography	91
	List of Figures	105
	List of Tables	108
	List of Acronyms	109
	Acknowledgements	111
	Erklärung	113

INTRODUCTION

“Far out in the uncharted backwaters of the unfashionable end of the western spiral arm of the Galaxy lies a small unregarded yellow sun. Orbiting this at a distance of roughly ninety-two million miles is an utterly insignificant little blue green planet whose ape-descended life forms are so amazingly primitive that they still think digital watches are a pretty neat idea.”

— Douglas Adams, *The Hitchhiker’s Guide to the Galaxy*

Since the dawn of humanity, we have looked up at the sky and wondered about the mysteries that the heavens held. Starting from the tracking of the motions of the Sun and the Moon, we have come to realize our place in the Universe, and along the way, we have uncovered some exotic objects, the secrets of the stars, the ways of the galaxies, and the mysteries of Universe. We have measured the motions of the planets, and formulated the evolution of the Universe. With each discovery, we have understood more about the working of the Universe. It is an achievement that the primitive ape-descended life forms have managed to grasp it. And yet, with each discovery we have come across phenomena that have challenged our theories. We found that we really know only 5% of the Universe, and that too not very well, and the rest is mostly unknown *Dark Matter* and *Dark Energy*. But it is the human nature to want to explore our surroundings, *Brahma Jidnyasa* — as it is

called in *Sanskrit* — the urge to understand the Universe, that motivates us to keep going in the face of unknown. This thesis is my attempt to understand a very small part of the Universe, and take our knowledge further by a tiny step. Here in this chapter I will introduce the Galactic Center environment.

1.1 THE MILKY WAY



Figure 1.1: The Milky Way across the night sky as seen at the ATCA site. Image credit: Alex Cherney (terraastro.com).

On the edge of the newly discovered “*Laniakea*” supercluster of galaxies (Tully et. al. 2014) lies the Milky Way Galaxy (also known as *the Galaxy*), a barred spiral galaxy host to 300 billion stars, including our own Sun, and the Solar system, which is located in its outskirts at a distance of 27,000 light years ($\sim 8kpc$) from the center in the Orion-Cygnus Arm. The Milky Way gets its name from its appearance in the night sky as a dim fuzzy glowing band stretching across the night sky, as seen in Fig. 1.1. It is made up of a disk of stars which is 100,000 light years in diameter, and only 1000 light years thick near the position of the Sun, decreasing away from the center. The disk contains most of the Milky Way’s stars and all of its gas and dust, with the total mass of $10^{11} M_{\odot}$. The spiral arms are located in this disk and are traced by the molecular clouds. These arms are thought to have formed because of the density waves from the interaction between the stars and the gas in the disk orbiting the Galaxy. As the molecular clouds are home to massive star formation,

the star clusters near the spiral arms have relatively young massive stars. The HII regions, illuminated by the massive young stars also run across the spiral arms. Periodic supernova explosions from the dying OB stars create expanding shells of material and fill the interstellar medium with hot ($\sim 10^6 K$) X-ray emitting gas. The stars eventually disperse from their birth environment, and thus the disk contains a mix of young and old stars.

The disk of the Galaxy is surrounded by a spherical halo of stars. This halo is sparsely populated and contains stars worth total mass of $\sim 10^9 M_\odot$ and virtually no gas and dust, and thus no star formation. Due to this, the halo stars are quite old and appear reddish in color. The small, spherical, densely packed globular clusters of about $10^5 - 10^6$ stars contain about 1% of the halo stars. Some of the oldest stars in the Galaxy can be found in these 150 globular clusters. This halo of the stars and the Galaxy are embedded in the spherical dark matter halo extending for hundreds of kiloparsecs, which has a mass of $\sim 10^{12} M_\odot$.

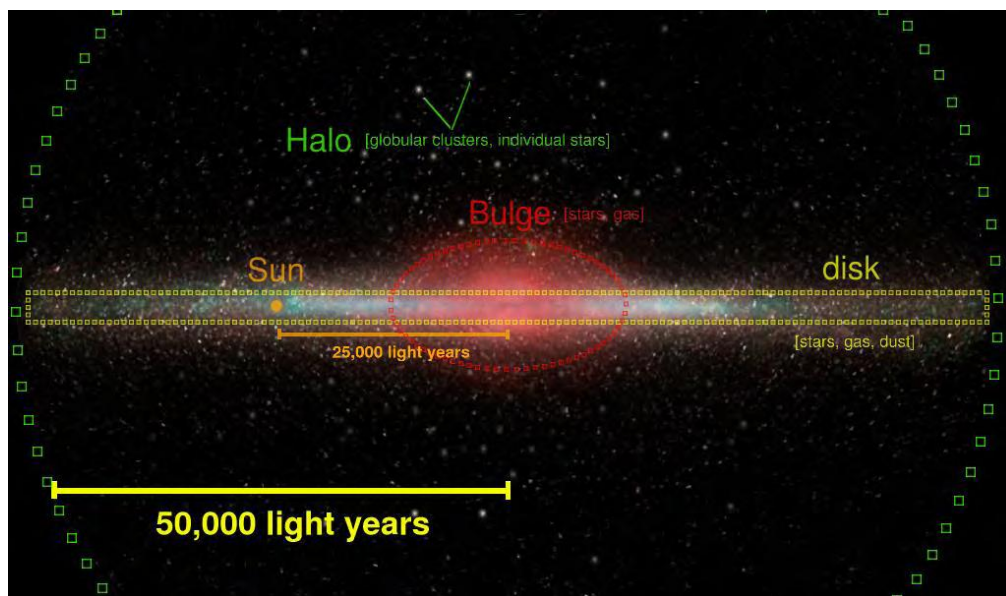


Figure 1.2: A sketch of our Galaxy showing different structural components, the disk, the bulge, and the halo. Image: Ka Chun Yu, *Introduction to Astronomy*.

Towards the center of the Galaxy is the flattened, elongated collection of stars known as the Galactic Bulge. The bulge stars away from the center are older. They have highly elliptical orbits, with largely random inclinations, although their aver-

age stellar motion is net rotation around the Galactic center. The center also contains a faint bar of the length of $1 - 5 kpc$. The nature of the bar is highly debated, with suggestions of a single bar, triaxial bulge, or two distinct nested bars. At the very center of the Galaxy lies a supermassive black hole (SMBH) Sagittarius A* (Sgr A*) with a mass of 4 million solar masses, the protagonist of this thesis. The center of the Galaxy is shrouded in the intervening gas and dust. Thus it remains obscured in the visible light, and cannot be observed. But it appears bright in other wavelengths of the spectrum, which can pierce through the dust, and provide us with the landscape of the central region.

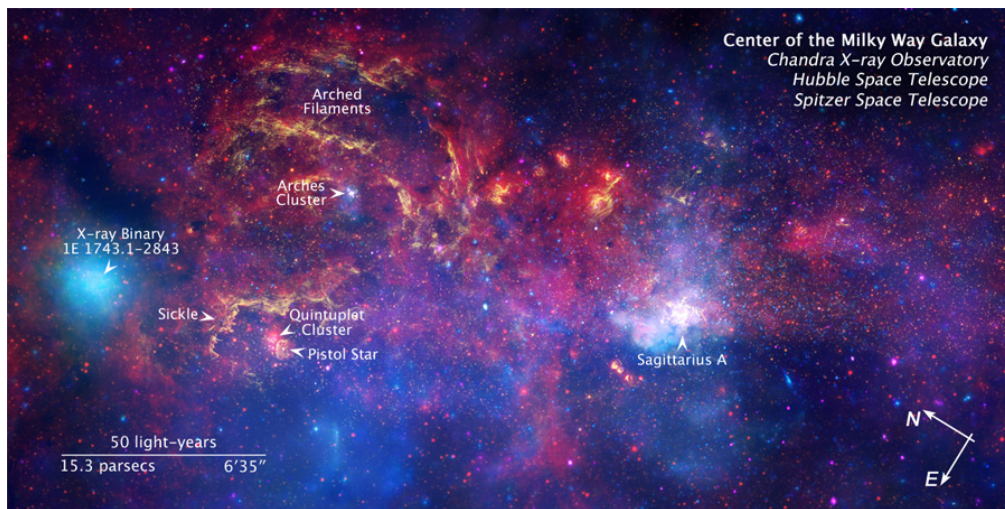


Figure 1.3: A combined image of the Galactic Center as seen from the Hubble Space Telescope in near-infrared, Spitzer Space Telescope in infrared, and Chandra X-ray Observatory in X-ray light. (Image credit: NASA/ESA/Spitzer/CXC/STScI).

The nucleus of the Milky Way is 100 pc across, which contains several stellar clusters, such as the Arches Cluster and the Quintuplet Cluster, as well as filaments of dust and gas which are heated up by the radiation from the stars, and are birthplaces of young stars (yellow in color as seen fig. 1.3). The X-ray traces the high energy emission from the accretion of material on compact sources and black holes. Sagittarius A complex is the brightest region in X-ray light, arising from the diffused gas that has been heated to several million degrees of temperature by stellar winds, and outflows from stellar explosions and from the supermassive black hole.

1.2 THE CENTER OF THE MILKY WAY

The inner few parsecs of the Milky Way galaxy is a complex and dynamic environment, with Sgr A*, the supermassive black hole at the dynamic center, and surrounded by the stellar cluster of young and evolved stars, interstellar medium with diffuse hot gas, molecular dusty ring and supernova-like remnants. It is a unique environment which allows for the study of the interplay of several phenomena, from star formation in the vicinity of the SMBH, physics of interstellar medium, to high energy emission processes associated with the accretion onto the black hole. Being the closest available galactic nucleus environment, it can be studied with the resolution that isn't possible to achieve with other galaxies. At a distance of ~ 8 kpc, one arcsecond corresponds to 0.04 pc ($\sim 1.2 \times 10^{17}$ cm). Thus the Galactic Center has been actively explored in radio, submillimeter, infrared, X-ray and γ -ray wavelength with high angular and spectral resolution.

1.2.1 The Galactic Center Interstellar Medium

The interstellar medium in the GC region is mostly distributed in giant molecular clouds. The central few parsecs of the GC consist of a circumnuclear disk (CND) of neutral atomic gas, enclosing a cavity of relatively less density containing atomic and ionized gas. Close to Sgr A* within 1 – 1.5 pc lies a region called Sgr A West, which contains the mini-spiral. These are ionized clumpy filaments or streamers that orbit Sgr A*. 1.3 cm and 3.6 cm observations with Very Large Array (VLA) telescope have identified the features of the mini-spiral, viz. the Western arc, the Northern and Eastern arms, and an extended bar, as seen in fig. 1.4 (Ekers *et al.*, 1983; Lo and Claussen, 1983; Serabyn and Lacy, 1985; Serabyn *et al.*, 1988; Schwarz *et al.*, 1989; Lacy *et al.*, 1991; Herbst *et al.*, 1993; Roberts and Goss, 1993; Liszt, 2003; Paumard *et al.*, 2004; Zhao *et al.*, 2009). The Western arc of the streamer is most likely on a circular orbit, while the other components, i.e. the Northern, and Eastern arms and the bar penetrate deep into the central region within few arcsecond from Sgr A* and have highly elliptical orbits.

These filaments are ionized by the ultraviolet radiation from the massive young stars. Of the $300 M_{\odot}$ neutral atomic gas and few M_{\odot} of warm dust, large fraction is associated with the mini-spiral streamers, while the ionizing fronts may be interfaces between the low density and high density regions described by the neutral ring (CND) (Paumard *et al.*, 2004). In the central parsec, the average gas density is lower than the surrounding CND. Study of the orbital motion of the streamers us-

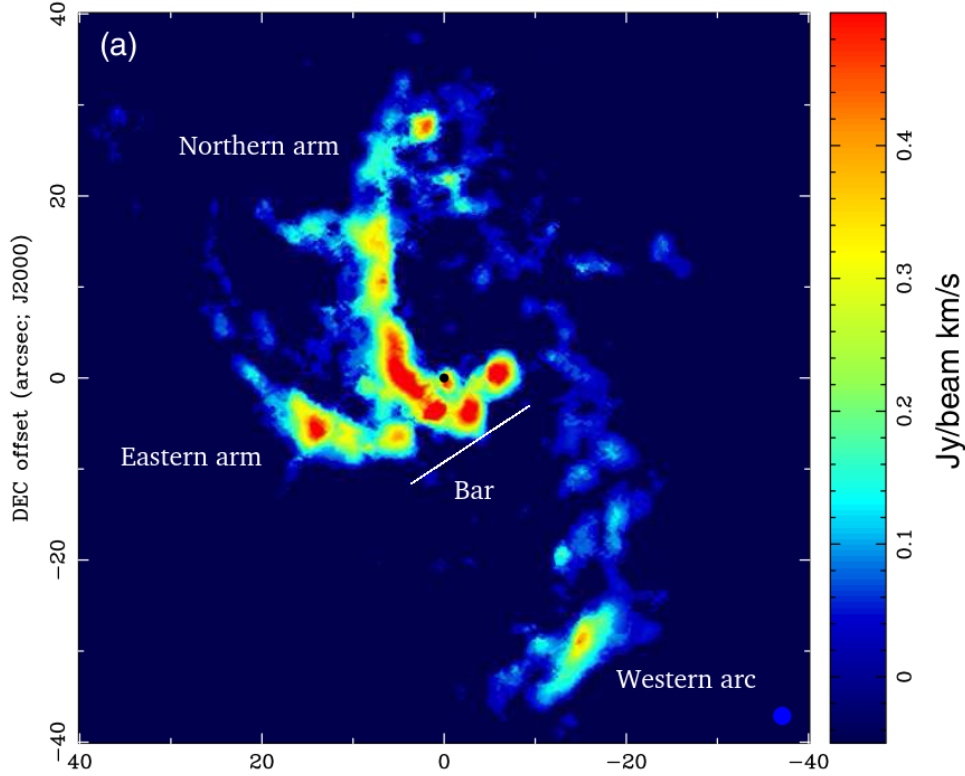


Figure 1.4: Integrated 8.3 GHz image of the mini-spiral with marked components, the Western arc, the Northern and Eastern arms, and the extended bar. (Image: Zhao *et al.* (2009)).

ing the VLA by Zhao *et al.* (2009) suggests that the CND and the enclosing streamers have their orbits at the same inclination relative to the plane of the sky. It is also suggested that these streamers are part of the inflow of gas due to dissipative loss of angular momentum from friction.

The circumnuclear disk is a dense torus-like ring or a disk surrounds the central parsec of the GC. It consists of clouds of dense molecular gas (Wright *et al.*, 2001; Herrnstein and Ho, 2002) and warm dust (Zylka *et al.*, 1995) of about 10^4 solar mass of gas and dust. It rotates around the center in a circular orbit, with a sharp edge at 1.5 pc and extends up to 5 – 7 pc from the center (Becklin *et al.*, 1982; Guesten *et al.*, 1987; Christopher *et al.*, 2005; Montero-Castaño *et al.*, 2009). The Western arc of the mini-spiral is thought to be the inner ionized surface of the CND. The studies of

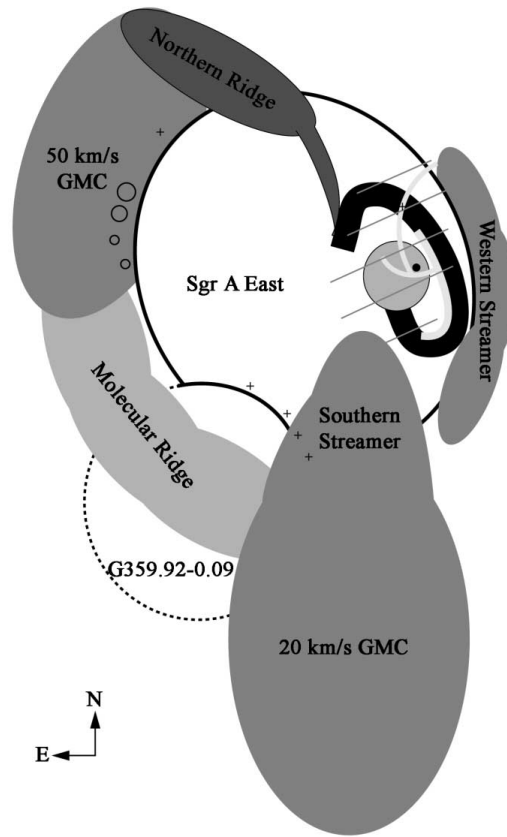


Figure 1.5: Schematic diagram of the Sgr A Complex as seen in the plane of the sky. (Image: Herrnstein and Ho (2005)).

the velocity field and line emission, and the clumpiness of the CND suggest that the CND may be a transient structure, although there is no conclusive evidence for it (Guesten *et al.*, 1987). Figure 1.5 shows the schematic of the larger scale structure of the interstellar medium in the Sgr A Complex, where the CND is surrounded by several thermal and non-thermal features, such as Sgr A East and the giant molecular clouds (GMCs).

1.2.2 The Star Clusters

The central parsec of the Galactic Center contains a dense star cluster, with Sgr A* at the dynamical center. The observations of the GC stellar cluster at IR and radio wavelengths over two decades have shown some intriguing characteristics. It is

an extremely dense cluster that contains mainly late-type red giants, including the asymptotic giant branch (AGB) stars. The spectroscopic observations also reveal hot early-type stars with strong winds exhibiting helium and hydrogen emission lines (“He stars”) (Krabbe *et al.*, 1995; Genzel *et al.*, 1996; Paumard *et al.*, 2006; Tanner *et al.*, 2006). These stars are generally characterized as the post main sequence Ofpe/WN9 stars, while some show characteristics of luminous blue variable (LBV) stars and Wolf-Rayet stars (Clénet *et al.*, 2001; Eckart *et al.*, 2004b; Moultaqa *et al.*, 2005).

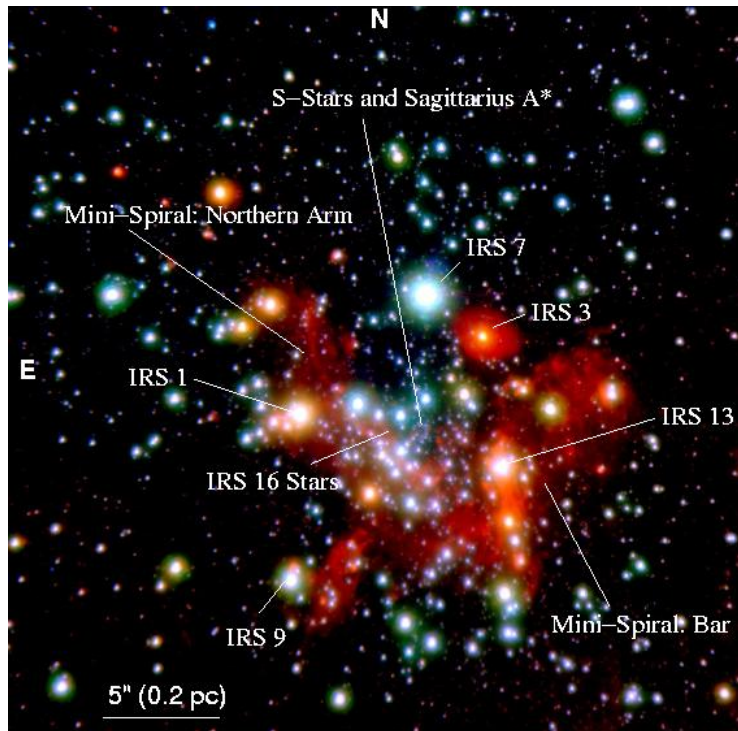


Figure 1.6: A composite NIR image ($\lambda = 1.5 - 4\mu\text{m}$) of the GC environment within the central parsec with the most prominent sources. The image is taken with NACO instrument at European Southern Observatory’s Very Large Telescope. Image: GC webpage of I. Physikalisches Institut, University of Cologne.

The presence of such young stars in the immediate vicinity of the SMBH is not completely understood. These stars are too young to have formed away from the center and migrated inwards while it is thought that the extreme tidal forces due to the presence of the supermassive black hole, the strong magnetic fields and stellar wind may make star formation impossible in the region. But recent study

of hydrodynamical simulations of the IRS stellar cluster 13 complex by [Jalali et al. \(2014\)](#) has shown that orbital compression of the clumps orbiting the SMBH on the elliptical orbit can not only not hinder but even assist the star formation by increasing the gas densities in the clump to critical limit and overcoming the tidal density of the black hole. Potentially younger objects have been discovered in the central parsec of Sgr A* that hint towards very recent or ongoing star formation ([Eckart et al., 2003, 2004b, 2005](#); [Moultaka et al., 2004a,b](#); [Mužić et al., 2008](#)). The GC also contains several luminous extended sources, which have now been known as bow shock sources, such as IRS 1W, 2, 5, 10W, and 21. These are caused by bright stars expelling strong winds through the ambient gas and dust of the northern arm ([Tanner et al., 2002, 2003, 2005](#); [Rigaut et al., 2003](#); [Eckart et al., 2004b](#); [Geballe et al., 2004](#)). Some of these stellar sources will be discussed later in detail in chapter 4.

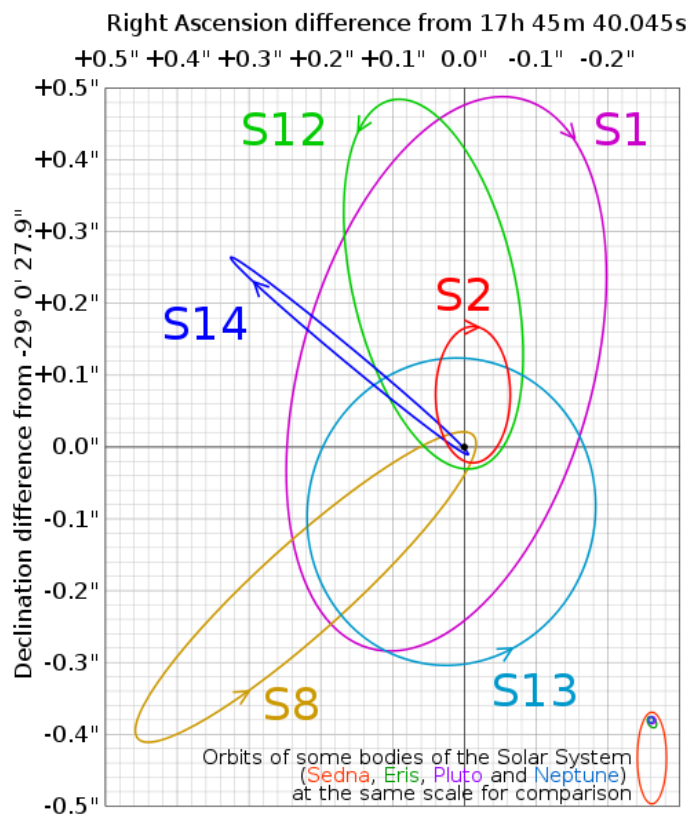


Figure 1.7: Inferred orbits of S-cluster objects around the supermassive black hole Sgr A* obtained from the data from [Eisenhauer et al. \(2005\)](#).

The central arcsecond near to Sgr A* has a star cluster containing high velocity stars called the S-star Cluster. The NIR observations from 8 – 10 m class telescopes equipped with adaptive optics have enabled to identify and study closely the stars in the extreme vicinity of the SMBH. These S-stars orbit around Sgr A* at extremely high velocities in highly eccentric and inclined orbits. The precise measurements of the positions and proper motions of these stars has allowed for the determination of trajectories of 20 stars, which has been used for the calculation of the mass of the SMBH as well as relativistic effects on the central stellar cluster due the the black hole (Genzel *et al.*, 1997; Schödel *et al.*, 2002; Ghez *et al.*, 2003; Gillessen *et al.*, 2009a,b). Of these S-stars, S2 is the brightest star with the shortest orbital period of ~ 15.9 years. Its motion was tracked for its full orbital period and was used to confirm the presence of the supermassive black hole and precisely determine its exact mass (Schödel *et al.*, 2002; Ghez *et al.*, 2003).

In 2012, a faint, dusty object was discovered in the S-star cluster, approaching Sgr A*, which is now called DSO/G2 (Gillessen *et al.*, 2012, 2013; Eckart *et al.*, 2013). From the first observations, the object was thought to be made up of pure dust and gas, with a mass 3 times the mass of the Earth. Further observations and analysis pointed towards presence of stellar source at the center that is surrounded by a cloud of gas and dust. It was supposed to undergo its closest approach passage to the SMBH during Spring of 2014 at a distance of 200 AU. The discovery raised several questions. Would the object be destroyed by the tidal forces of the SMBH or would it survive the closest approach? How much of its mass would get accreted on to the black hole, and will it be enough to cause large variations in the flux density to brighten up Sgr A* across all wavelengths? This sparked a frenzy of observations from multiple telescopes (including observations I performed in 2013 & 2014, see section 2.3.2 for details). In section 3.6.1, I will discuss in details the results of the observations and conclusions of the DSO flyby.

1.2.3 Sagittarius A*

In 1971, Lynden-Bell and Rees (1971), by applying the then speculative black hole model for quasars to the Milky Way, pointed out that the Galaxy should contain a supermassive black hole at its center, which might be detectable with radio interferometry. A compact radio source was subsequently observed by Balick and Brown (1974) using the Green Bank Telescope of the National Radio Astronomy Observatory (NRAO). It was then later confirmed by Westerbork and Very Large Baseline Interferometry (VLBI) observations (Ekers *et al.*, 1975; Lo *et al.*, 1975), and

was named as Sagittarius A*. It was discovered that Sgr A* was located near the dynamical center of the streamers in the nucleus from the high resolution VLA observation [Brown et al. \(1981\)](#).

Sgr A* is one of the brightest radio source in the sky. It is always visible in this wavelength regime as its intensity never falls below the detection limit. Thus it can be monitored continuously in the radio regime. In contrast, Sgr A* is not detectable in IR and X-ray regime in its quiescent state and becomes visible only in its flaring state. Thus radio interferometric observations, thanks to the radio brightness of Sgr A*, allow us to study the SMBH at very high resolution.

One of the important question — how well does Sgr A* actually coincide with the dynamical center of the stellar cluster — was answered by radio observations. The detection of SiO masers in the IR stars in both NIR and millimeter wavelengths within central arcsecond of Sgr A* led to the precise calculation of NIR reference frame, and the location of Sgr A* to within 30 mas in the NIR frame (See chapter 4 for details). The radio interferometric observations of the GC by [Reid et al. \(1999, 2003\)](#) with the Very Long Baseline Array (VLBA) have provided an accurate measure of the position and proper motion of Sgr A* with respect to the extragalactic sources. From these observations they estimate that Sgr A* has a peculiar motion of $-18 \pm 7 \text{ km s}^{-1}$ towards positive galactic longitude and $-0.4 \pm 0.9 \text{ km s}^{-1}$ towards the north Galactic Pole ([Reid and Brunthaler, 2004](#)). No significant acceleration was detected in the motion of Sgr A*. These values are consistent with the zero proper motion. The simulations of the stellar motions of the central star cluster and the proper motion of Sgr A*, the estimated lower limit on the mass of Sgr A* is $0.4 \times 10^6 M_{\odot}$ within few AU. This result, along with the IR observations of the proper motions of S-cluster stars around Sgr A* has led to the conclusion that the radio source Sgr A* is associated with a supermassive black hole with a mass of $4 \times 10^6 M_{\odot}$, which is at the dynamical center of the central stellar cluster.

Thanks to multiwavelength observations of the GC, the spectrum of Sgr A* is well-known. Sgr A* is known to be extremely dim compared to other objects in the same class, radiating at roughly nine orders of magnitude lower than the Eddington limit, which is the theoretical maximum limit at which black holes can accrete given mass. The low luminosity of Sgr A* can be partly explained by the accretion rate, which is significantly lower than the possible Eddington accretion rate. [Fig. 1.9](#) shows the spectral energy distribution (SED) of Sgr A* in its quiescent phase across

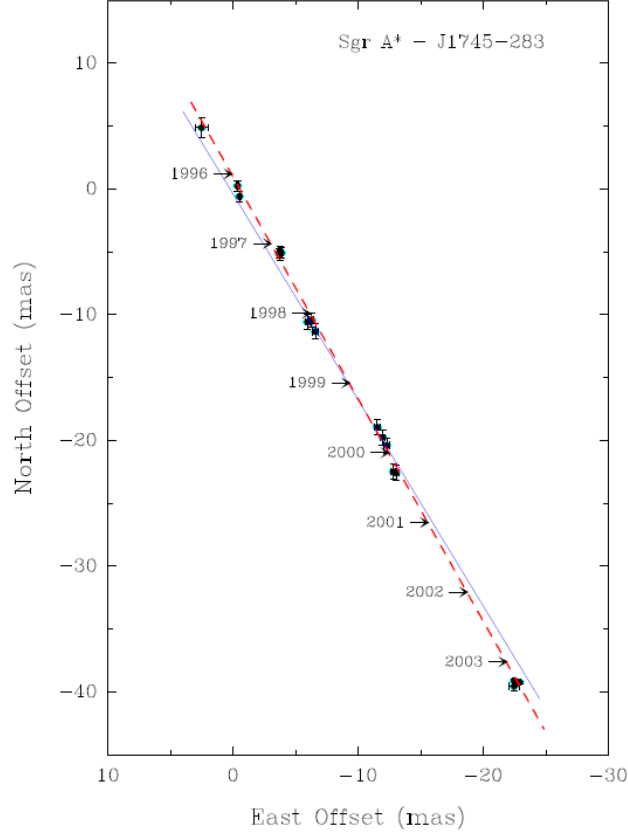


Figure 1.8: The figure shows apparent motion of Sgr A* on the plane of the sky. Position residuals of Sgr A* relative to extragalactic source J1745 – 283 is plotted along with $1 - \sigma$ error bars. The dashed line represents the variance-weighted best-fit proper motion, and the solid line gives the orientation of the Galactic plane. Image: Reid and Brunthaler (2004).

radio, near-infrared and X-ray wavelengths. The low frequency spectrum at centimeter wavelength rises slowly with spectral index of $\alpha = 0.1 - 0.3$ (the spectral index α is given as $S_\nu \propto \nu^\alpha$). The spectral index increases to $\alpha = 0.5$ at higher frequencies, and peaking at $\alpha = 0.7$ at 2 – 3 mm. This is known as the ‘submillimeter bump’. This excess is probably due to the synchrotron self-absorption radiation from the innermost optically thick region of the accretion disk. The turnover at the submillimeter wavelengths happens as a result of the transition from optically thick to optically thin, and the inner accretion region becomes transparent to the synchrotron radiation. The spectral index of this part of the spectrum is negative

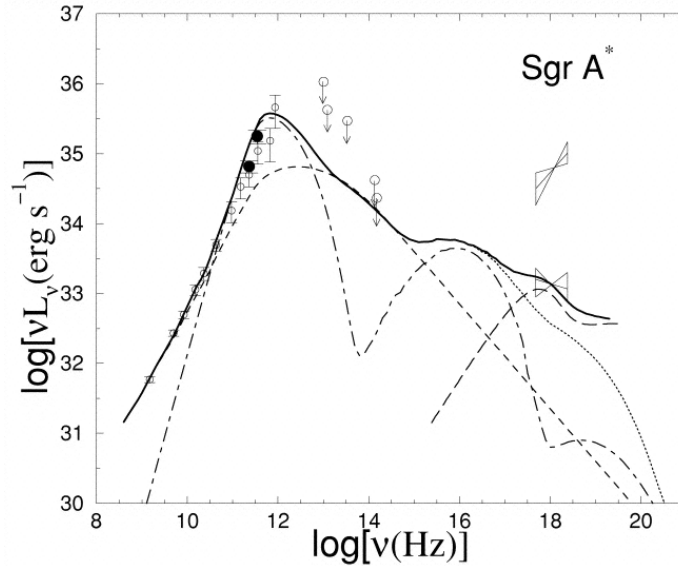


Figure 1.9: Spectrum of Sgr A*. Image: [Yuan et al. \(2003b\)](#).

($\alpha < 0$), though the measurement of the index value of the quiescent spectrum at infrared & X-ray wavelength is not possible as the value varies with flux.

The models for the SED of Sgr A* have to explain the discrepancy between the Eddington luminosity and the observed luminosity. The most successful model to explain the low luminosity was the advection dominated accretion flow model (ADAF) which assumes a radiatively inefficient accretion flow. It involves an optically thin, but geometrically thick accretion disk. Since the accretion disk is thick, the radial velocity and temperature are much larger and density of accretion flow is lower. Estimates from the observations of radio and submillimeter polarization ([Bower et al. 2003](#); [Marrone et al. 2006](#)) predict significantly lower electron densities in the accretion region of Sgr A*, implying that most of the material does not reach the central black hole. This leads to the radiative time scales to be longer than the accretion time scale. Thus the accretion flow energy is not radiated away, but stored as thermal energy, thus leading to observed low efficiency.

1.2.4 Flaring of Sgr A*

Observations of the flux density of Sgr A* over different wavelength regimes have shown that it is a highly variable source in all wavelengths, from NIR & X-ray to

radio and submm (Baganoff *et al.*, 2001; Genzel *et al.*, 2003; Eckart *et al.*, 2006b, 2008, 2012; Yusef-Zadeh *et al.*, 2006a,b; Li *et al.*, 2009; Dodds-Eden *et al.*, 2009; Kunneriath *et al.*, 2010). This variability has been observed over wide range of time periods, from few minutes to few hours to few days. The first simultaneous multiwavelength observations were carried out by Eckart *et al.* (2004a). Since then, several such observations have been carried out, in which variations in the flux density of Sgr A* (called flares) were detected in NIR, X-ray, as well as in radio and submm regime. The radio/submm flares have been demonstrated to follow the brightest simultaneous NIR/X-ray flares with a delay of ~ 100 min, indicating a link between flaring activity in different regions (Eckart *et al.* 2004a, 2006b, 2008; Marrone *et al.* 2008; Yusef-Zadeh *et al.* 2006b, 2008).

Several models have been proposed to explain the flaring activity of Sgr A* with varying merits. Some of the prominent models are the adiabatically expanding plasmon model, the Jet-model with a weak jet, and the rotating hotspot model. The study of the variability of Sgr A* can be helpful in understanding the physical processes in the vicinity of the SMBH, and understand the basic emission mechanisms of the accretion disk. The flaring activity of Sgr A* at mm wavelength will be discussed in detail in chapter 3.

1.3 OUTLINE

In this thesis, I will present the radio interferometric observations of the GC with Australia Telescope Compact Array (ATCA) at 3mm, which were carried out between 2010 – 2014. In chapter 2, I will introduce the basics of radio interferometry, as well as provide the details of observations and data reduction. This thesis consists of two main parts:

- **The flaring activity of Sgr A*** In this part (Chapter 3) I will discuss the results of the monitoring of flaring activity of Sgr A* at 3mm wavelength. I will present the methods used to obtain flux and light curves, and calculating the variability of Sgr A*. I will present the results of the modeling of the observed flares with the expanding plasmon model, and the analysis of the individual flares. I will also discuss various models that have been used to study the flaring of Sgr A*.

- **SiO maser sources in the central parsec** In Chapter 4, I will present the SiO maser sources that were detected within the central parsec of the Galactic Center during the 3mm observations with ATCA. I will describe the technique used to detect the maser sources, and the method to compute the precise positions and proper motions of the detected sources. I will then discuss the results and properties of the SiO masers.

In Chapter 5, I will present the summary and conclusions of the thesis.

RADIO INTERFEROMETRY, OBSERVATIONS, AND DATA REDUCTION

“There is a theory which states that if ever anyone discovers exactly what the Universe is for and why it is here, it will instantly disappear and be replaced by something even more bizarre and inexplicable.

There is another theory which states that this has already happened.”

— Douglas Adams, *The Restaurant at the End of the Universe*

2.1 RADIO ASTRONOMY

For most of the human existence, the view of the Universe was restricted to the visible light. With the advances in electromagnetic theory in the 19th century, it was understood that objects could emit radiation apart from optical light. Radio waves were first postulated from the electromagnetic equations of James Clerk Maxwell and were subsequently discovered by Heinrich Hertz in 1887. The first practical radio transmitters and receivers were developed by Guglielmo Marconi in mid-1890s. The first astronomical discovery of radio source was done by Karl Jansky in 1933 when his antenna serendipitously discovered the radiation from Milky Way, and is now considered as the birth of radio astronomy. The field of radio astronomy gained momentum when scientists and engineers, who had carried out research

on radar technology during the World War II, turned their attention to astronomy to develop observational and instrumentation techniques. It led to the discovery of 21-cm hydrogen line, the pulsars, the quasars, and the cosmic microwave background radiation. And now radio astronomy has become one of the most important tools in astronomy and has been used complimentary to other wavelength astronomy.

The Earth's atmosphere is opaque to most of the electromagnetic spectrum, with two main windows, the optical-infrared band and the radio band, where it is transparent. This allows us to observe astronomical sources from the ground, as opposed to other wavelengths where satellite or balloon observations become necessary. The opacity of the atmosphere is shown in fig. 2.1. As seen from the figure the optical-NIR band is very narrow. Compared to that, radio wavelength can be useful between the wide window of wavelengths between 10 meters (30 GHz) to 0.3 millimeter (1 THz), which allows for the observations of wide range of astronomical sources, such as molecular gas, galaxies, active galactic nuclei etc. The radio regime is divided into several bands: HF (below 30 MHz), VHF (30 – 300 MHz), UHF (300 – 1000 MHz), microwaves (1000 – 30000 MHz), millimeter-wave, and sub-millimeter-wave. At wavelengths smaller than 1 cm, only specific bands are available for observations as atmospheric absorption from vibrational transition from atmospheric molecules such as CO_2 , O_2 , and H_2O noise and attenuation creates limitations for observations. At wavelengths longer than 10 meters, the atmosphere is completely opaque due to reflection from ionosphere.

The exceptionally broad frequency band of five orders of magnitude has two main consequences. The wide band allows for observations of a variety of astronomical sources, which arise from different thermal and non-thermal mechanism. These include non-thermal radiation from galaxies, the strong radiation from the radio galaxies and quasars powered by SMBHs, thermal emission from cold interstellar gas, continuum emission from stars & pulsars, extrasolar planets and so on. It also means different observation telescopes and techniques need to be developed to cover various bands of the radio spectrum.

2.1.1 Emission mechanisms

Electromagnetic theory describes two main types of emission processes: continuum emission and line emission. The continuum emission process is further divided into thermal and non-thermal emission. A continuum emission occurs when

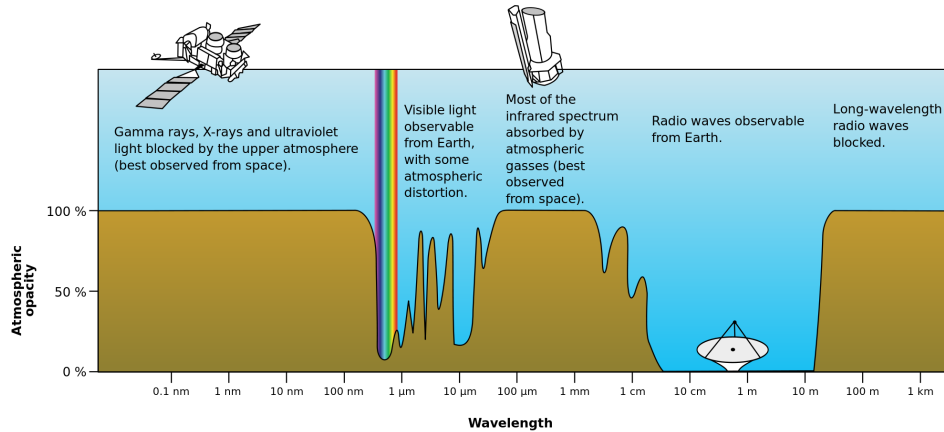


Figure 2.1: Electromagnetic transmittance of the atmosphere of the Earth over different parts of the electromagnetic spectrum. Image: NASA/jpl.nasa.gov

a source emits light in a continuous spectrum, as opposed to the line emission, which is quantized emission that gives rise to discrete lines or spectrum.

2.1.2 Thermal emission

Thermal radiation is the most basic form of radiation. All objects with a temperature emit continuous radiation that is proportional to the fourth power of their absolute temperature ($\propto T^4$, Stefan-Boltzmann Law). There are two main types of thermal emission: the blackbody radiation, and the free-free emission.

Blackbody radiation:

A blackbody is an object that absorbs all the radiation incident on it and radiates a smooth spectrum of radiation. The peak of the radiation occurs at a frequency that is proportional to its temperature (see fig. 2.2) given by the Wien's displacement law:

$$\nu_{max} = 5.879 \times 10^{10} T \text{ Hz}$$

The power emitted per unit area per unit frequency is given by the Planck's law:

$$B(\nu, T) = \frac{2h\nu^3}{c^2} \frac{1}{e^{h\nu/k_B T} - 1} \quad (2.1)$$

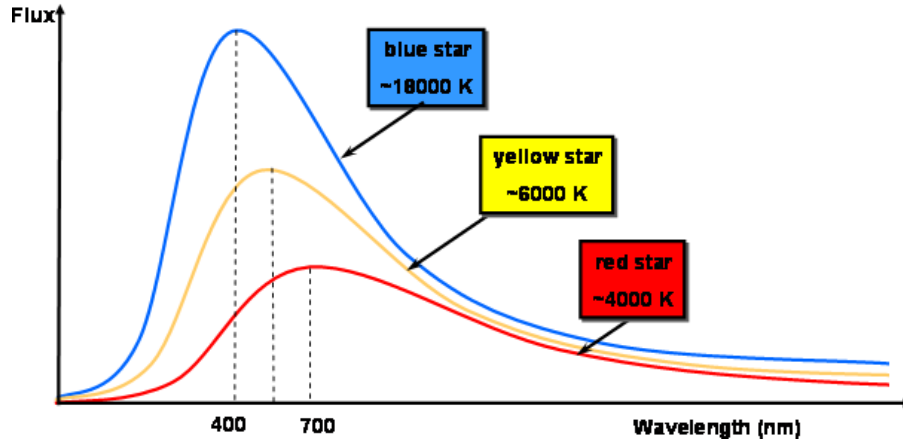


Figure 2.2: Blackbody radiation curves at different temperatures. Image: astronomy.swin.edu.au.

where ν is the frequency, k_B is the Boltzmann constant, T is the absolute temperature, and c is the speed of light. For radio wavelength region, the energy of photons is very low ($h\nu \ll k_B T$), and thus the Rayleigh-Jeans limit is relevant over all of the radio window. The emitted power is then given by:

$$B(\nu, T) = \frac{2h\nu^2 k_B T}{c^2} \quad (2.2)$$

The first examples of black bodies at radio wavelength were solar system planets and asteroids. Stars, dust emission from interstellar medium, the cosmic microwave background emission are some other examples of thermal blackbody radiation.

Bremsstrahlung:

Another form of thermal emission occurs from electrons traveling in ionized gas or plasma (HII region). It is produced by free electrons scattering off ions without being captured, hence called free-free emission or *bremsstrahlung*. In a plasma, the heavy immobile ions continuously cause slight deviations in the path of fast moving electrons. Since any charged particle that is accelerating also radiates, each deviation produces broad spectrum, and the power of the radiation emitted by the particle is given by the Larmor's formula:

$$P = \frac{2}{3} \frac{q^2 \dot{v}^2}{c^3} \quad (2.3)$$

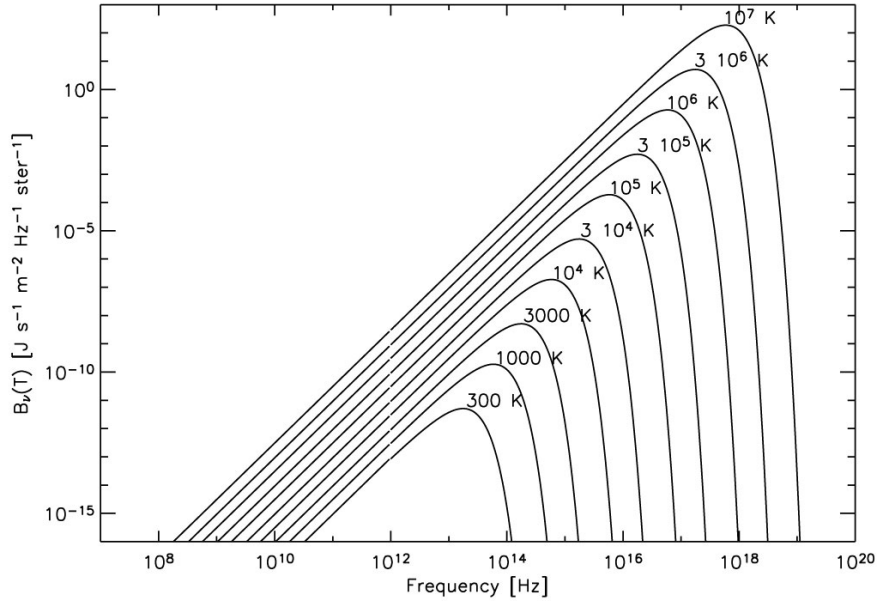


Figure 2.3: Log-log plot of the blackbody curves for different temperatures. The straight line slope of the curve below THz (10^{12} Hz) frequency shows that the Rayleigh-Jeans approximation for the Planck law is valid for the radio frequencies. Image: web.njit.edu.

An inverse process to the free-free emission is the thermal bremsstrahlung absorption, i.e., the absorption of energy from free-moving electron. An astronomical source radiating bremsstrahlung will show both the effects in its spectrum, the emission and absorption. Assuming a Maxwell-Boltzmann distribution of velocities, the optical depth of the region is

$$\tau_\nu \propto \int T^{-3/2} \nu^{-2} n_e^2 ds \quad (2.4)$$

where n_e is the electron number density. At low frequencies, $\tau_\nu \gg 1$, the HII region is optically thick, its spectrum approaches blackbody spectrum with temperature T , and its flux density varies as the square of the frequency. At high frequencies, the HII region is optically thin with $\tau_\nu < 1$ and its flux density changes as $S_\nu \propto \nu^{-0.1}$.

2.1.3 Non-thermal emission

If the characteristics of the emitted radiation are independent of the temperature of the source, the radiation is known as non-thermal radiation.

Synchrotron emission:

Synchrotron radiation is a process that dominates much of high energy astrophysics. It is caused by the acceleration of charged particle moving at relativistic speeds in a magnetic field. It was first observed in early betatron experiments where the electrons were first accelerated to relativistic energies. In astronomy, only the radiation from an ensemble of electrons with a wide energy distribution is observed. Thus many of the details of the radiation are lost in the averaging process. In many cases, the synchrotron radiation is emitted by electrons which have power-law distribution:

$$N(\gamma)d\gamma \propto \gamma^{-p}d\gamma$$

We can then express the emissivity as

$$\epsilon_\nu \propto B^{(p+1)/2} \nu^{-(p-1)/2}$$

where B is the magnetic field. For the electron energy spectrum with power law index p , the spectral index of the synchrotron radiation, defined by $\epsilon_\nu \propto \nu^{-\alpha}$, is $\alpha = (p-1)/2$. The spectral shape is thus determined by the shape of electron energy spectrum, rather than the shape of emission spectrum from individual electrons.

The radio emission from the Galaxy, supernova remnants, and extragalactic radio sources is a result of synchrotron radiation.

Synchrotron self-absorption:

For every emission process, there is an absorption process. The process of scattering of emitted photons off of synchrotron electrons is known as synchrotron self-absorption. If the scattering process occurs many times, only the emission from the thin surface layer is observed, and the total flux observed is much smaller. For sufficient low frequencies and homogeneous source, the source becomes optically thick, and the flux density can be given by $S_\nu \sim \nu^{5/2}$. At higher frequencies, the source is optically thin. The frequency at which the source changes from optically thick to optically thin is known as the turnover frequency, where the optical depth $\tau = 1$.

Inverse Compton scattering:

Inverse Compton scattering is the scattering of low energy photons to high energies by relativistic electrons so that the photons gain while the electrons lose the

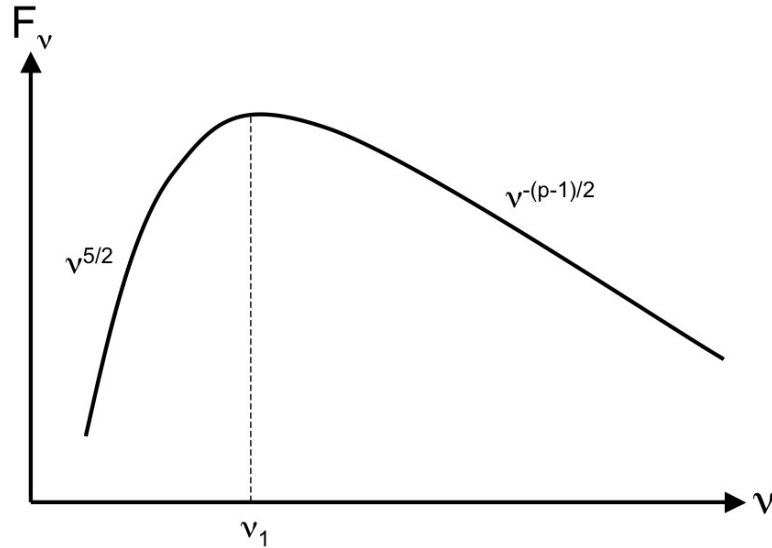


Figure 2.4: The spectrum of a homogeneous cylindrical synchrotron source for optically thick and thin region, with the turnover frequency ν_1 . Image: ifa.hawaii.edu

energy. The inverse-Compton scattering is important for astronomy, especially active galactic nuclei and black holes, whose accretion disks produce a thermal spectrum. The low energy photons produced in the accretion disk can be up-scattered to high energies by the high-Lorentz-factor electrons. In AGN and blazars, the synchrotron processes produce such low speed photons. These photons can then be up-scattered by the same electrons that produced them. This process is then called *synchrotron self-Compton (SSC)*. Energy losses due to the inverse-Compton process are referred to as electron cooling.

The gamma ray bubbles arising from the center of the Milky Way observed with the Fermi-Gamma ray space telescope are thought to be due to the inverse Compton scattering of synchrotron radiation [Su et al. \(2010\)](#).

2.1.4 Line emission

Spectral lines are narrow emission or absorption features in the spectra of gases which appear at discrete frequencies. The spectral lines are a quantum phenomena. The quantization of angular momentum gives rise to discrete energy levels in atoms and molecules. The transitions between these discrete energy states in the physical

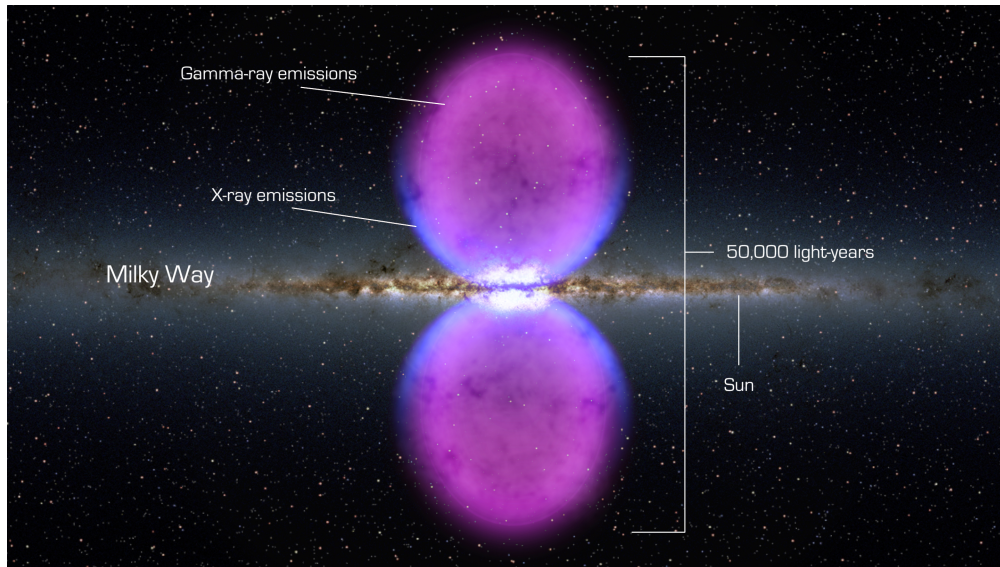


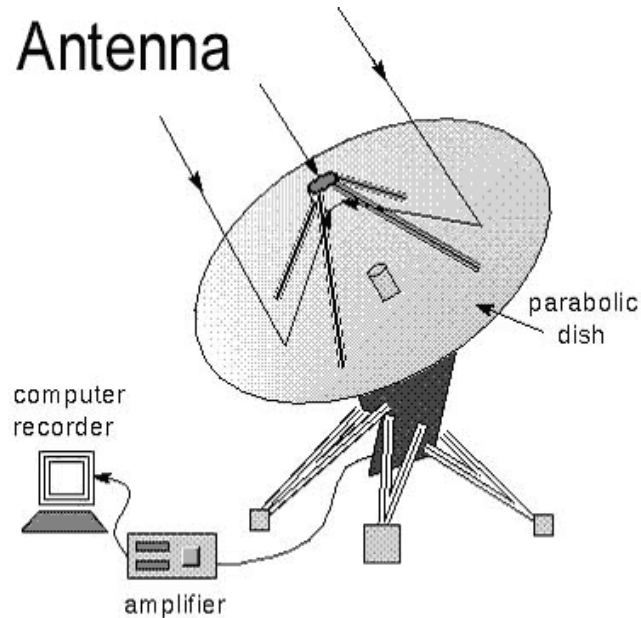
Figure 2.5: The illustration of the Gamma-ray bubbles arising from the GC. Image: Fermi telescope website.

systems result in spectral line emission and absorption. At radio wavelengths, the main sources of spectral line emission are the rotational transitions of molecules, such as CO, NH₃ etc. The 21-cm emission from the hydrogen line is the hyperfine transition between the two levels of the ground state of the electron in hydrogen atom.

Another type of emission that is important at the radio wavelengths is the naturally occurring stimulated emission in molecules, called as maser (microwave amplification by stimulated emission of radiation). It is produced by the population inversion of the transition. The spectral lines are an important tool to study then physical and chemical properties of their sources. Hydroxyl (OH), water (H₂O), and silicon oxide (SiO) masers are some of the most prominent sources of maser emission in millimeter astronomy. The SiO maser emission will be discussed in details in chapter 4.

2.2 RADIO TELESCOPES

Radio telescopes are the instruments used to detect the electromagnetic radiation at radio wavelengths. Most modern radio telescopes are antennas with parabolic



A radio telescope reflects radio waves to a focus at the antenna.

Figure 2.6: A simple sketch showing different components of a single dish radio telescope. Image: <http://www.haystack.edu/>

reflecting dishes that can be pointed to the direction of the source of radiation. The parabolic dish reflects the radio waves to a *subreflector* located close to the prime focus, which then reflects the waves to the *feed* at the center of the reflector. The Radio telescopes generally have a Cassegrain subreflector system. The signal from the feed is then sent to the receiver and amplifier system, which magnifies the faint radio signals. Throughout this process, the signal remains proportional to the strength of the incoming radiation, so that the resulting map is a true representation of the emission from the source. The amplifiers are extremely sensitive and are normally cooled to very low temperatures to minimize interference due to the thermal noise. The spectral power received by the detector of unit projected area is called the source flux density S_ν , given by

$$S_\nu = \int_{source} I_\nu d\Omega \quad (2.5)$$

here I_ν is the specific intensity or the spectral brightness of the source, in the units of $\text{Wm}^{-2}\text{Hz}^{-1}\text{sr}^{-1}$, and $d\Omega$ is the solid angle between the observer and the source.

The flux density is measured in the units of *Jansky* (with $1 \text{ Jy} = 10^{-26} \text{ Wm}^{-2} \text{ Hz}^{-1}$). If we assume that the incident radiation is thermal in nature (even when it is actually not), we can express the specific intensity in terms of brightness temperature T_B which is given by

$$T_B(\nu) = \frac{I_\nu c^2}{2k_B \nu^2} = \frac{S_\nu \lambda^2}{2k_B d\Omega} \quad (2.6)$$

One of the important parameters of a telescope is its resolution. From the diffraction theory, the resolution of a single dish radio telescope is given by

$$\theta = 1.22\lambda/D \text{ (radian)} = 2.52 \times 10^5 \lambda/D \text{ (arcsec)}$$

where D is the diameter of the dish. The resolution of single dish telescopes is limited by the maximum size of the movable dish that can be constructed. The largest antenna also suffer from many issues such as tracking accuracy problem, gravitational distortion, solar heating etc. For example, a single dish telescope with aperture of 22 meters, operating at 3 mm wavelength will have a resolution of $\sim 35''$. This is very low resolution compared to optical telescopes. Thus for high resolution observations, single dish telescopes are not useful. To improve the resolution, single dish telescopes are combined to form an interferometer. Interferometry techniques combine several single antennas to synthesize a larger aperture, defined by the *baseline* B – the separation between the two antennas. Then the angular resolution is given as $\theta = 1.22\lambda/B$. Thus, larger the separation between the individual antennas, better will be the resolution of the interferometer.

2.2.1 Interferometry and aperture synthesis

The basics of interferometry come from the Young's double slit experiment, where coherent waves passing through two slits produce an interference pattern.

The van Cittert-Zernike theorem relates the spatial coherence function $V(r_1, r_2)$ to the distribution of intensity of the incoming radiation $I(s)$ received at two points r_1 and r_2 . It shows that the spatial correlation function $V(r_1, r_2)$ depends only on $r_1 - r_2$

$$V_v(\mathbf{r}_1, \mathbf{r}_2) = \int I_v(\mathbf{s}) e^{(-2\pi v \mathbf{s} \cdot (\mathbf{r}_1 - \mathbf{r}_2)/c)} d\Omega \quad (2.7)$$

Thus if one knows the mutual coherence function of the electric field, then the source brightness distribution can be measured by taking the Fourier transform.

Consider a two element interferometer, as shown in figure 2.7, with a separation of \mathbf{b} looking towards a point source in a direction $\hat{\mathbf{s}}$. Plane waves traveling from the

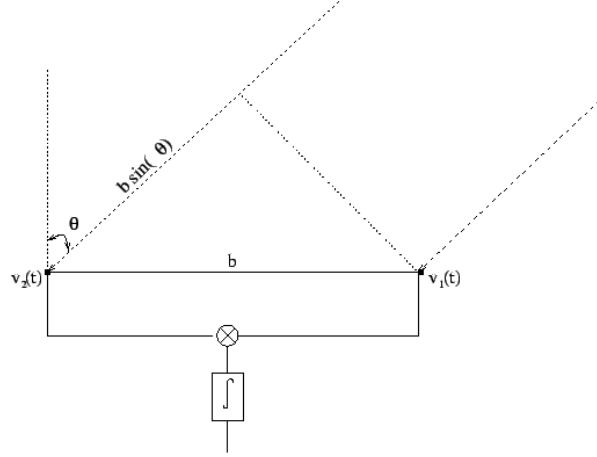


Figure 2.7: A block diagram showing a simple two element interferometer. Image: gmrt.ncra.tifr.res.in

distance source must travel extra distance of $b \sin \theta$ to reach antenna 2, so the output at both the antennas is the same but the output at antenna 2 lags behind by the geometric delay of $\tau_g = \mathbf{b} \cdot \hat{s} / c$. If the output voltage at antenna 1 is $V_1 = V \cos(2\pi\nu t)$ then the output voltage at antenna 2 is $V_2 = V \cos(2\pi\nu(t - \tau_g))$ where t is time and ν is the radiation frequency. These signals are first multiplied at the correlator which gives

$$V_1 \cdot V_2 = V^2 \cos(2\pi\nu t) \cos[2\pi\nu(t - \tau_g)] = \left(\frac{V^2}{2}\right) [\cos(2\pi\nu t - 2\pi\nu\tau_g) + \cos(2\pi\nu\tau_g)]$$

and then takes a time average which removes the high energy term $\cos(2\pi\nu t - 2\pi\nu\tau_g)$ so that the final output is

$$R = \langle V_1 V_2 \rangle = \left(\frac{V^2}{2}\right) \cos(2\pi\nu\tau_g)$$

The correlator output R varies sinusoidally with the rotation of the Earth. This sinusoidal pattern is called as the fringe pattern. The fringe phase depends on θ and is a sensitive measure of the source position for projected baselines $b \cos \theta$ longer than several wavelength distances. Thus interferometers can measure the positions

of compact radio sources with great accuracy, with errors as small as $\sim 10^{-3}$ arcsec. The response R of a two-element interferometer with directive antennas is the product of the power pattern of the individual antennas, and is known as the *primary beam*. The point-source response of an interferometer can be improved by adding more baselines. An interferometer with N antennas contains $N(N-1)/2$ baselines. Each of these can be connected together and the combined response is known as the *synthesized beam*.

The response of an interferometer to a spatially incoherent extended source with sky brightness distribution $I_\nu(\hat{s})$ can be obtained by assuming the extended source to be sum of independent point sources.

$$R(\mathbf{b}) = \int \int_{\Omega} A(\mathbf{s}) I_\nu(\mathbf{s}) e^{i2\pi\nu\tau_G} d\Omega d\nu$$

Here $A(\mathbf{s})$ is the effective collecting area of the antennas in the direction of \hat{s} . The coordinates of the antennas when projected onto a plane perpendicular to the line of sight form a plane with axes u and v , thus called the (u, v) plane and they describe the projected separation and orientation of the elements. The coordinates l and m are direction cosines towards the astronomical source. Then the visibility function measured by the interferometer is given by

$$V_\nu(u, v) = \int \int A_\nu(l, m) I_\nu(l, m) e^{-2\pi i(u l + v m)} dl dm \quad (2.8)$$

Taking the inverse Fourier transform of the above equation gives the source brightness distribution

$$I'(l, m) = A(l, m) I(l, m) = \int_{-\infty}^{\infty} V(u, v) e^{2\pi i(u l + v m)} du dv \quad (2.9)$$

Each observation of the source with a baseline and orientation forms a point in the $u-v$ plane, and a combined array of multiple baselines including the rotation of the Earth fills up the plane, as can be seen from fig. 2.8. This can then be used to construct the image of the source.

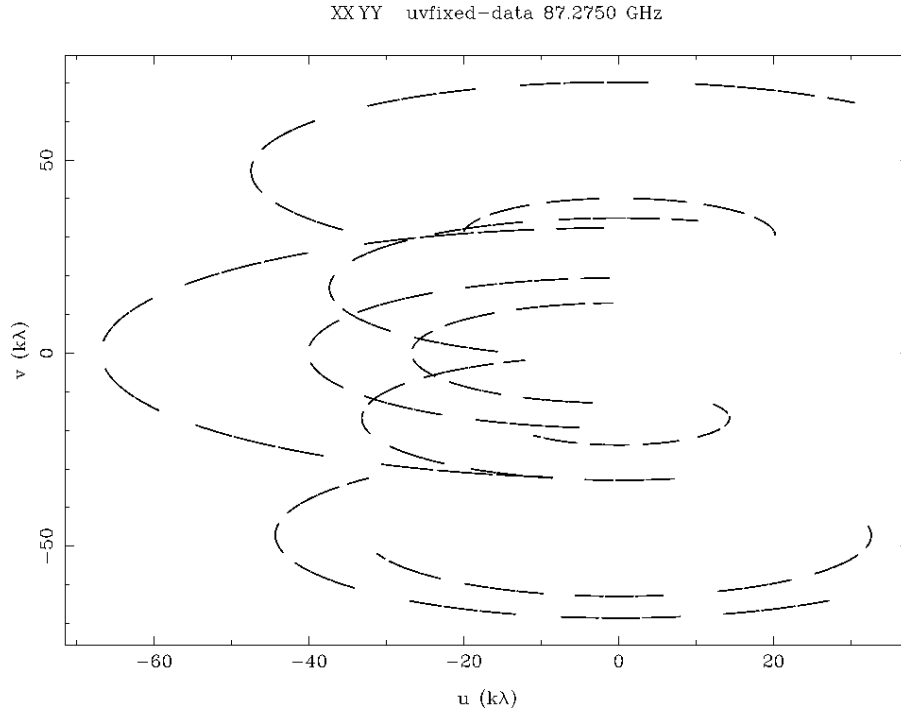


Figure 2.8: As an example of the $u - v$ coverage of telescope array – the $u - v$ coverage of Sgr A with ATCA*

2.3 OBSERVATIONS

2.3.1 The Telescope

We have used the Australia Telescope Compact Array (ATCA) for observing the Galactic Center at 3 mm. ATCA is an array of six 22-m telescopes located at the Paul Wild Observatory in Narrabri, New South Wales, about 550 km North-West of Sydney, in Australia. It is operated by the Australia Telescope National Facility (ATNF) of the Astronomy and Space Science division of the Commonwealth Scientific and Industrial Research Organisation (CSIRO). The telescope operates in seven observing bands: 20 cm, 13 cm, 6 cm, 1 cm, 7 mm, and 3 mm. The antenna 6 is permanently fixed in its location, which gives a maximum available baseline of 6 km, but it is available for only select few array combinations. It is also not fitted with a 3 mm receiver, and thus is unavailable for 3 mm observations. Thus at 3 mm, the angular resolution can range between $0.2''$ to $6''$.

2.3.2 Observation details

We have observed the GC at 3 mm wavelength with the ATCA between 2010 and 2014. Out of these, the observations in 2013 and 2014 were performed by me. The location of ATCA has an advantage, as the GC passes almost overhead in the southern hemisphere, it allows us to observe the GC for more than 8 hours a day. The Compact Array Broadband Backend (CABB) of the telescope was upgraded in 2007. This allows for observations with two 2048 MHz intermediate frequency (IF) bands. The observations were performed with the spectral line mode at two different frequency bands at 86.243 and 85.640 GHz. These frequencies correspond to two rotational transition lines of the SiO maser (SiO $J = 2 - 1$, $\nu = 1$ and $J = 2 - 1$, $\nu = 2$). The observations were conducted for approximately 10 – 12 hours per observation day. At the start of the observations, the bandpass calibrations were carried out for 30 min with PKS 1253 – 055, and flux calibration with Uranus at the end of the observations. We observed Sgr A* with three sets of 25 min on-source observations which are in-between the observations of gain calibrators (see Table 2.1). For phase calibrations we used Sgr A* as it is strong enough source that it can be used as a self calibrator. The details of the observations are summarized in Table 1. The mapping and data reduction of the interferometer data was performed using the MIRIAD data reduction package.

The primary beam size of the telescope is ~ 0.5 arcmin while the resultant secondary beam size of the telescope is 1.95×2.28 arcsec. The antenna gain of ATCA strongly varies with the elevation angle. It is most efficient at the elevation angle of 60° and has a minimum value of efficiency at the elevation of 90° . The gravitational distortion of the dish causes small deformations in the shape of the dish. This deformation is significant when observing sources closer to the horizon, and thus it limits the antenna efficiency at angles below 40° . Another factor to consider for the antenna gain is the angular separation between Sgr A* and the calibrator (Li *et al.* 2009). If we use a distant calibrator, the gain corrections resulting from it cannot fully compensate for the elevation effects. These effects show up in the light curve, and should be avoided. For this, the gain calibrators we used were nearby calibrators within 10° of Sgr A*, among them mainly PKS 1741 – 312, as it is only 2.29° away from Sgr A*. Some secondary gain calibrators were also used for consistency. As I have discussed in section 2.1, at millimeter wavelength, the atmosphere is not transparent for electromagnetic waves. This can result in large fluctuations in the gain. Especially for observations at lower elevation angles (less than 45°), we observe strong variation due to the thick atmosphere. For certain compact array



Figure 2.9: The Australia Telescope Compact Array during observations in 2013.

configurations of the telescope, some antennas suffer from the shadowing effect, and it is significant for elevations of $< 40^\circ$. Thus we only use the observational data above the elevation of 40° .

2.3.3 Data reduction

Once the observations are complete, the raw data obtained stored from the telescope needs to be processed. Data reduction is a procedure for processing the raw

Table 2.1: The Log of observations of Sgr A* taken during 2010 to 2014. The dashes represent the days on which observations were not made. See section 3.4 for details.

	Date	Array	Calibrators	Start Time UT	End Time UT
2010	May 13	H214	1741–312	2010 May 13 11:04:45	2010 May 13 21:50:25
	May 14		1622–297	2010 May 14 10:45:07	2010 May 14 22:07:40
	May 15		1741–312	2010 May 15 10:10:30	2010 May 15 22:30:10
	May 16		1622–297	2010 May 16 10:08:47	2010 May 16
2011	May 23	H214	1741–312	2011 May 23 09:57:43	2011 May 23 21:05:13
	May 24		1741–312	2011 May 24 09:56:05	2011 May 24 21:24:17
	May 25		1741–312	2011 May 25 10:01:13	2011 May 25 21:22:30
	May 26		1741–312	2011 May 26 10:03:01	2011 May 26 21:17:33
2012	May 15	H214	1714–336	2012 May 15 08:23:47	2012 May 15 21:51:35
	May 16		1714–336	2012 May 16 10:04:30	2012 May 16 21:45:22
	May 17		1714–336	2012 May 17 09:49:17	2012 May 17 21:52:18
	May 18		1714–336	2012 May 18 11:02:51	2012 May 18 21:56:46
2013	June 26	EW352	1741–312	2013 June 26 08:18:21	2013 June 26 20:44:37
	June 27	EW 352	1741–312	2013 June 27 ---	2013 June 27 ---
	August 31	1.5A	1741–312	2013 August 31 03:36:08	2013 August 31 14:57:04
	September 1	1.5A	1741–312	2010 September 2 ---	2013 September 2 ---
	September 14	H214	1741–312	2013 September 14 03:08:12	2013 September 14 13:27:58
	September 16	H214	1741–312	2013 September 16 ---	2013 September 16 ---
2014	April 1	H168	1741–312	2014 April 1 14:54:24	2014 April 1 23:38:55
	April 2	H168	1741–312	2014 April 2 13:37:58	2014 April 3 00:22:18
	June 7	EW352	1714–336	2014 June 7 08:00:50	2014 June 7 19:00:02
	September 26	H214	1714–336	2014 September 26 02:05:40	2014 September 26 12:44:31
	September 27	H214	1714–336	2014 September 27 02:10:13	2014 September 27 12:40:51

data to correct for errors and interference in measurements. To perform the data reduction, I used the MIRIAD data reduction software (Sault *et al.* (1995)). I start with flagging the data for bad data points as well as outliers and interferences. After that, several calibrations are performed. The aim of calibrations is to find out the relationship between the observed visibilities V_{obs} and the true visibilities V . For each baseline:

$$V_{obs}(t, \nu) = V(t, \nu) \cdot G(t) \cdot B(t, \nu)$$

here t is time and ν is frequency. G is the complex continuum gain, and B is the complex frequency-dependent gain (i.e., the *bandpass*).

- Bandpass calibration is a process of measuring and correcting the frequency-dependent part of the gains $B(t, \nu)$. The antenna based complex gains vary

across the passband. These need to be corrected before the visibilities from individual frequency channels are averaged. Hence bandpass calibration is performed to estimate and correct for the bandpass shape.

- Amplitude calibration: The interferometers do not measure the absolute flux densities of the sources. Thus the relative flux density scale is usually set by observing an unresolved reference source whose flux density is believed to be stable and whose intensity has previously been measured on an absolute scale. In our case, planet Uranus was used as a flux calibrator.
- Gain calibration: Antenna based complex gains vary slowly with time with variation of the order of few tens of minutes. These slow variations are measured and corrected using periodic observations of a secondary calibrator, which is not too far from the source.
- Phase calibration: The phase calibration determines the instrumental and atmospheric phase effects by observing a point-like source that is not variable and whose position is well-known.
- Self calibration: The technique of self-calibration is used to make additional corrections to the antenna gains as a function of time. This is similar to basic calibration discussed above, the main difference being that self-calibration procedure is often performed iteratively, each time with a better model, until finally the sequence converges.

After performing these calibrations, a final image is produced using following steps:

The image produced by Fourier transform of the visibilities is called the *dirty image*. Since the $u - v$ plane is not sampled completely (as seen from fig. 2.8), it causes imperfections in this image. The inverse Fourier transform of the sampling function produces a point spread function, which is referred to as *dirty beam* in radio astronomy. We assume that the dirty image is a convolution of the dirty image with the dirty beam. The CLEAN algorithm attempts to deconvolve the dirty beam from the dirty image, and convolves it with a Gaussian shaped *clean beam* to produce a clean image.

BREAKFAST HABITS OF THE BEAST: FLARING OF SAGITTARIUS A*

*“The story so far:
In the beginning the Universe was created. This has made a lot of
people very angry and been widely regarded as a bad move.”*

— Douglas Adams, *The Restaurant at the End of the Universe*

3.1 INTRODUCTION

As I have discussed in chapter 1, Sagittarius A* shines at luminosity several orders of magnitude less than the Eddington luminosity. To explain this faint emission, several theoretical models have been proposed. For the substantial mass inflow of the accreting gas that is predicted towards Sgr A*, these models require a very inefficient radiation mechanism (Narayan *et al.* (1998); Liu and Melia (2001); Melia and Falcke (2001); Yuan *et al.* (2003b); Goldston *et al.* (2005); Liu *et al.* (2006)). The advection dominated accretion flow (ADAF) model was used to model the multiwavelength spectrum of Sgr A* successfully (Narayan *et al.* (1998)). This model predicts a two-temperature radiatively inefficient flow which is advected across the event horizon. Significantly lower electron densities in the accretion region of Sgr A* are predicted from the estimates from the observations of radio and

submillimeter polarization (Bower *et al.* 2003; Marrone *et al.* 2006). This means that only small portion of the material finally reaches the central black hole. The study of the flare emission from Sgr A* allows us to contribute to the solution of this issue.

It has been known for quite a few years now that Sagittarius A* is highly variable across all wavelength bands, from radio-submillimeter to NIR-X-ray wavelengths. The NIR flares have been observed prominently where the flux can increase by up to a factor of ~ 20 above the detection limit and in X-ray by up to a factor of ~ 160 . In millimeter wavelengths, the flux variation during a flaring event up to 40% have been detected (Mauerhan *et al.* (2005)). Multiwavelength observations of the GC have shown that the NIR & X-ray flares occur simultaneously, and last for about 50 – 80 minutes (Eckart *et al.* 2004a, 2006b, 2008; Marrone *et al.* 2008; Yusef-Zadeh *et al.* 2006b, 2008), while the radio-submm flares were demonstrated to follow the brightest NIR/X-ray flares with a delay of ~ 100 minutes, with a lifetime of 90 – 150 minutes. This suggests that there is a connection between these flares at different wavelengths. It is thought that the same set of particles gives rise to the flares at different wavelengths. Since Sgr A* is embedded in thick thermal material, it is difficult to observe the intrinsic structure of the source region that gives rise to the flares. But the observations of flares can provide constraints on the source structure and emission mechanism.

Several models have been provoked to explain the flaring activity and the emission mechanism of Sgr A*. The synchrotron and synchrotron self-Compton (SSC) model has been used to explain the flare emission at the NIR/X-ray wavelengths. The model involves up-scattering of the sub-mm photons from a compact source component. The inverse Compton scattering of the THz-peaked flare spectrum by relativistic electrons gives rise to the X-ray flares while the NIR flares arise due to the synchrotron and SSC mechanism. The flares in radio and submillimeter regime are caused by the adiabatic expansion of the source components. Alternative models include the hot spot model, and the jet-outflow model. I will discuss these models in next section.

3.2 MODELS

3.2.1 The Synchrotron and SSC model

The synchrotron and SSC model assumes a uniform magnetic field B , and a power law distribution of electrons

$$N(E) = N_0 E^{-(2\alpha+1)}; (\gamma_1 m c^2 < E < \gamma_2 m c^2)$$

for a synchrotron source of angular size θ . The Schwarzschild radius of the SMBH is $R_s = 2R_g = 2GM/c^2 \sim 8\mu\text{as}$ where R_g is the gravitational radius of the SMBH. Thus at a distance of 8kpc from us, the size of one R_s corresponds to an angular size of $8\mu\text{as}$. The synchrotron spectrum has an optically thin spectral index α given by

$$S_\nu \propto \nu^{-\alpha}$$

where S_ν is the flux density at frequency ν . The synchrotron spectrum has a turnover frequency of ν_m with flux density S_m . (See section 2.1.3 for the detailed discussion of synchrotron emission mechanism). This source has a bulk velocity of $\beta = v/c$. This gives a relativistic boost factor of

$$\delta = \Gamma^{-1} [1 - \beta \cos \phi]^{-1}$$

where Γ is the bulk Lorentz factor

$$\Gamma = [1 - \beta^2]^{1/2}$$

ϕ is the angle between the velocity vector and line of sight.

The magnetic field strength is then given by

$$B = 10^{-5} b(\alpha) \theta^4 \nu_m^5 S_m^{-2} \delta \quad (3.1)$$

Synchrotron photons from the spectrum are scattered by the same population of source electrons population, giving rise to an inverse-Compton flux density

$$S_{SSC} = d(\alpha) \ln \left(\frac{\nu_2}{\nu_m} \right) \theta^{-2(2\alpha+3)} \nu_m^{-(3\alpha+5)} S_m^{2(\alpha+2)} E_X^{-\alpha} \delta^{-2(\alpha+2)} \quad (3.2)$$

Here E_X is the X-ray photon energy in keV, $d(\alpha)$ and $b(\alpha)$ are dimensionless parameters that are function of α , as shown in table 3.1, from Marscher (1983). The SSC spectrum has the same spectral index of α as the synchrotron component within the wavelengths of λ_{max} to λ_{min} corresponding to energies of E_{min} to E_{max} . To produce the observed flux in the X-ray domain, Lorentz factor of the order of $\gamma_e \sim 10^3$ of the emitting electrons is required. The upper synchrotron cut-off frequency for this lies in NIR bands. Thus, most of the NIR spectrum can be explained by synchrotron emission, while the inverse Compton emission explains the X-ray emission. The detailed derivation and discussion of this formalism can be found in Eckart *et al.* (2012).

Table 3.1: The values of dimensionless parameters $d(\alpha)$ and $b(\alpha)$ for various values of α . Source: [Marscher \(1983\)](#)

α	$d(\alpha)$	$b(\alpha)$
0.25	130	1.8
0.5	43	3.2
0.75	18	3.6
0.1	9.1	3.8

3.2.2 The adiabatic expanding plasmon model

Multiwavelength campaigns have shown that the radio/sub-mm flares follow the brightest NIR/X-ray flares by 1.5 ± 0.5 hours, and are shown to be related to the higher frequency flares. The adiabatically expanding plasmon model which was developed by [van der Laan \(1966\)](#) has been used extensively to analyze the radio and sub-mm flares of Sgr A*. This model assumes that the adiabatic expansion of the synchrotron components in the synchrotron and SSC model used in section 3.2.1 causes the flares in radio and submillimeter regime. Multiwavelength analysis of the simultaneous flaring of Sgr A* conducted in the previous studies ([Eckart et al., 2006b, 2008, 2012](#); [Yusef-Zadeh et al., 2006a, 2008](#)) have demonstrated that the peak of the light curves occurs at successively lower frequencies (starting from NIR to sub-mm to millimeter to radio frequencies). The initial event that energizes the electrons gives rise to NIR and X-ray flares, and the expanding self-absorbed synchrotron source results in flares at lower frequencies. When the synchrotron component becomes optically thin at a particular frequency, the flux reaches its peak value at the frequency. The peak value reached by the flux is determined by the size of the component, and the time period of the flare is given by the expansion speed of the blob. The model is successful in the prediction of the simultaneous flaring and declining emission occurs at NIR and X-ray wavelengths, and then successive flares occurring at lower frequencies in sum-mm and mm radio regime where the blob is initially optically thick.

This model assumes a synchrotron component of relativistic electrons which has a power-law energy spectrum, $n(E) \propto E^{-p}$. This source is situated in a magnetic field that declines as R^{-2} . As the component expands, its particle energy of each relativistic particle reduces proportional to R^{-1} and the particle density scales as

R^{-3} (van der Laan, 1966). The frequency dependence of the flux density I_ν is given as

$$I_\nu = I_0 \tilde{\nu}^{5/2} \rho^3 \xi(\tau_\nu) \quad (3.3)$$

Here $\tilde{\nu} = (\nu/\nu_0)$ is the normalized frequency, $\rho = (R/R_0)$ is the expansion factor for the expanding blob of synchrotron emitting relativistic electrons with R_0 as the initial radius, and $\xi(\tau_\nu) = \frac{1 - \exp(-\tau_\nu)}{1 - \exp(-\tau_0)}$. The optical depth of the synchrotron radiation τ_ν scales as

$$\tau_\nu = \tau_0 \tilde{\nu}^{-(p+4)/2} \rho^{-(2p+3)} \quad (3.4)$$

where τ_0 is the critical optical depth at the peak of the flux density at any particular frequency, and ν_0 is the frequency at which the flux density peaks when $R = R_0$ at time $t = t_0$. For frequencies $\geq \nu_0$ the blob is initially optically thin. The initial optical depth τ_0 depends only on the particle spectral index p through the condition

$$e^{\tau_0} - (2p/3 + 1)\tau_0 - 1 = 0. \quad (3.5)$$

Thus for a given particle spectral index p and peak flux density I_0 at the turnover frequency ν_0 , the model gives the variation in flux density at any frequency as a function of the expansion factor $\rho = (R/R_0)$.

3.2.3 The Hot Spot model

The orbiting hot-spot model is a frequently used model that has been invoked to analyze the short term NIR and X-ray variability of Sgr A* (Broderick and Loeb 2006; Eckart *et al.* 2006b). This model postulated that the accretion disk around the SMBH form bright overdensities which manifest as hot spots in the accretion disk. These hot spots revolve around the SMBH in Keplerian orbit close to the last stable orbit. Since the spots are moving at high velocities, they appear brighter while approaching than receding due to the relativistic beaming effects and Doppler shift. To estimate the parameters of the NIR & X-ray flares, a combination of the relativistic effects and the SSC modeling are used (Eckart *et al.*, 2006b; Zamaninasab *et al.*,

2010). The radio and sub-mm flares have been described by using the hot spot model combined with the radiatively inefficient accretion models. The opacity effects in the accretion disk are taken into consideration for modelling in the radio band (Broderick and Loeb 2006; Li *et al.* 2009). This model has been invoked to study the physics of accretion disks in AGNs and stellar-mass black holes in binary systems. But an absence of a standard gaseous disc near Sgr A* limits the applicability of this model (Levin and Beloborodov 2003). The $\sim 90 - 120$ minute time lag observed between the NIR and radio flares is also not explained by this model.

3.2.4 The Jet model

The Jet-ADAF model is another model which has often been invoked to analyze the flaring of Sagittarius A* (Falcke *et al.* 1993; Markoff *et al.* 2001; Yuan *et al.* 2002). The combined accretion-jet model was used to illustrate the spectral energy distribution from the quiescent emission of Sgr A*. This model states that the emission from Sgr A* comes from the interaction of the synchrotron and SSC components in the accretion disc with the short jet*. It postulates a presence of a blob of relativistic electrons in the accretion disk which are emitting synchrotron radiation. When this component gets caught up in the outflow of the jet, it gives rise to the flares. The X-ray and NIR flares are produced by the upscattering of the SSC components. The motion of the blob along the jet causes it to accelerate and expand. Because of this expansion, emission reaches its peak at successive radio wavelengths which corresponds to different sections of the jet. This model can predict the flaring in the NIR and X-ray regime without a delay, and explain the delay in the flare time of the radio/sub-mm flares, and the observed 10% linear polarization in the sub-mm bump. The jet model has been used to describe the emission of low luminosity AGNs (LLAGN) (Herrnstein *et al.* 1998; Bietenholz *et al.* 2000; Yuan *et al.* 2003a; Anderson *et al.* 2004; Liu and Wu 2013; Nemmen *et al.* 2014). And given that Sgr A* is thought of as the weakest known LLAGN, a jet outflow from Sgr A* is also postulated. Although such a jet has been assumed, any jet from Sgr A* has not been observed, but only circumstantial evidence has been found for the presence of a jet. There have been detections of some extended features at position angles 120° to 130° (Eckart *et al.* 2006b,a; Morris *et al.* 2004). These detections, suggest towards presence of a jet, when coupled together with the NIR polarization of synchrotron radiation (Shahzamanian *et al.* 2015). An upper limit of about 10^{-3} AU can be put on the size of the jet of Sgr A* by comparing with the parameters obtained from the analysis of the LLAGN. This value is significantly smaller than best resolution

available with the current telescopes (Markoff and Falcke 2003). The detection of the jet is made difficult by the possible low surface brightness and it remains hidden. Next generation telescopes with higher resolution observations will be able to resolve the neighbourhood of Sgr A*.

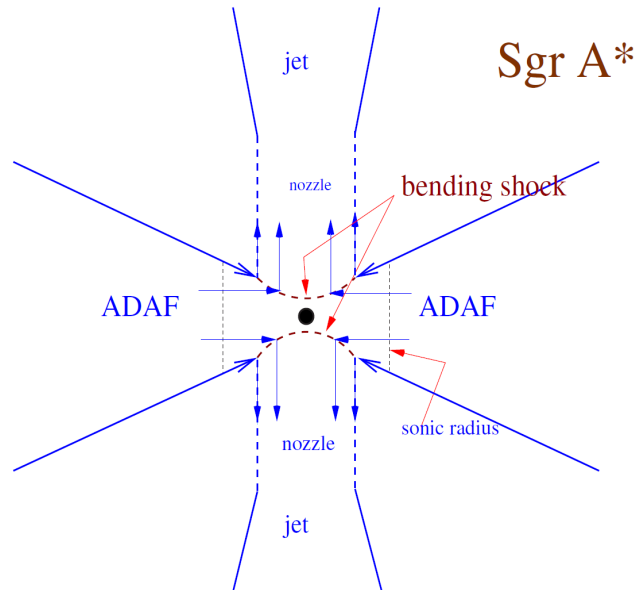


Figure 3.1: The schematic diagram of jet-disk coupling model for Sgr A*. Image: Yuan et al. (2003a).

For analyzing the emission from Sgr A*, the two qualitatively distinct models can be integrated together (Eckart et al. 2015). In the basic formulation, the orbiting or the outward traveling source has the relativistic bulk motion which is given by the Lorentz factor, but it is expected that the source may have a helical-type motion. The orbital motion of the component gives rise to the flux variations in the central plane, while the ejection of the material along the jet cause the flares from the outflow, where the bulk velocity of the component is close to the speed of light. The magnetic field lines close to the SMBH are embedded into the accreting material. They are further dragged in a toroidal motion due to the orbiting material. Further away from the black holes the magnetic field lines emerging out are tangled into a spiral which gives rise to the radial element of the blob velocity.

Recently, Mohan and Mangalam (2015) analyzed a phenomenological model of the combined orbiting hot spot component in helical motion along the surface of a

conical magnetic field embedded in the inner accretion disc. It has been proposed that an outward motion along spiraling trajectories can lead to quasi-periodic variability. Observations of the variability of Sgr A* in several different frequency bands and polarimetry can be used to test this model in the future (Broderick and Loeb, 2009).

For the purpose of this thesis, I will use the adiabatic expanding plasmon model for modeling the observed flare events in the data.

3.3 OBTAINING THE LIGHT CURVES

As the 6th antenna of ATCA does not have a receiver for 3mm observations, it is unavailable for our observations. Because of this, the maximum baseline available at 3mm is 214m for H214 configuration, which is the array configuration we have used predominantly. The resulting synthesized beam is 2 arcsec. At shorter baselines, the diffuse emission originating from the extended sources in the neighbourhood of Sgr A*, such as the mini-spiral, dominates the flux density at this angular resolution, and also a contributor at longer baselines. Table 3.2 shows the obtained lower quartile flux density from the light curves for our observations of Sgr A*. We assume that this lower quartile value represents the base flux density value of Sgr A* around which we detect flux variations. These flux density values are consistent with the values from the ATCA database, and with the recent VLA observations of Sgr A* (Sjouwerman and Chandler 2014). The flux contains contribution from the extended emission around Sgr A*. There have been indications of ~ 8 hour variability in the flux density of the Sgr A* by Witzel *et al.* (2012) and Dexter *et al.* (2014). This variation may account for the fluctuations in the flux density values from different consecutive observation days.

To find out the intrinsic flux density of Sgr A*, we need to account for these contributions*. The contributions from the extended flux and the atmospheric and instrumental variations in the flux of Sgr A* were corrected using the method developed by Kunneriath *et al.* (2010). In this method, we first extract the flux values from two orthogonal pairs of the longest baselines, and then we subtract the median baseline and time dependent flux was for each baseline from each dataset of observations. For each given baseline b , $s_b(t)$ represents its observed flux density. Then $S_b(t)$ gives the median baseline flux for each year

$$S_b(t) = \mu_{yr}(s_b(t)). \quad (3.6)$$

Table 3.2: The lower quartile flux density values of the Sgr A for the observations.*

Observation Day	Flux density [Jy]
13 May 2010	4.68
14 May 2010	4.18
15 May 2010	4.49
16 May 2010	3.62
23 May 2011	3.51
24 May 2011	3.46
25 May 2011	2.98
26 May 2011	3.43
15 May 2012	3.69
16 May 2012	3.48
17 May 2012	3.02
18 May 2012	2.84
26 June 2013	3.96
31 August 2013	3.86
14 September 2013	6.08
01 April 2014	2.29
02 April 2014	2.53
07 June 2014	2.71
26 September 2014	2.26
27 September 2014	2.21

The time dependent differential flux density $I(t)$ and the uncertainties $\delta I(t)$ were calculated using

$$I(t) = \mu_b(s_b(t) - S_b(t)) \quad (3.7)$$

and

$$\delta I(t) = \mu_b(S(t) - (s_b(t) - S_b(t))) \quad (3.8)$$

Here μ_{yr} represents the median operator where the median is taken over the all the observation days for each particular year, while μ_b is the median calculated over different baselines. The uncertainty in the differential flux density $\delta I(t)$ is given by the median of the deviation from the median flux $I(t)$. Because the differential flux takes both positive and negative values, I added or subtracted a constant flux value from the differential flux densities to model the flux densities. I attribute the residual flux density dips/excesses to variations in the intrinsic flux density of Sgr A*.

3.4 RESULTS

As the atmosphere is no longer transparent at 3mm, the observations with ATCA are very sensitive to atmospheric conditions. On several observing days, the light curves are contaminated by turbulence in the atmosphere or rainfalls. These contaminations manifest as strong and rapid fluctuations in the flux at very short timescales (~ 30 minutes). Most of the observation on 16 May 2010 were affected by turbulence. A heavy rainfall on 23 May 2011 resulted in extreme variations (~ 7 Jy) in the flux density. On 26 May 2011 and 15 May 2012 we observed similar rapid variation, as the turbulence affected large portions of the observations.

No data was obtained on 27 June, 1 September and 16 September in 2013 as heavy rainfall on these three days prevented from observing the GC (marked by '– – –' in the Table 1). Large fluctuations were also observed in part of the data on 31 August and 14 September 2013 due to turbulence and during the rest of the remaining time, the flux remained fairly stable. We did not detect any significant fluctuations on 26 June 2013 either.

The observations in 2014 were not affected by atmospheric events and the conditions were good. For all observation days, good quality flux data was obtained. But no flaring activity was detected on any day of 2014 on the time-scale of $\sim 100 - 150$ minutes within the time of the observation.

We observed flares on three occasions, 13 May 2010, and 17 May and 18 May in 2012. The light curves of the corresponding dates are shown in Fig. 1 along with the light curves of the calibrators. These flares will be discussed in the following section in detail.

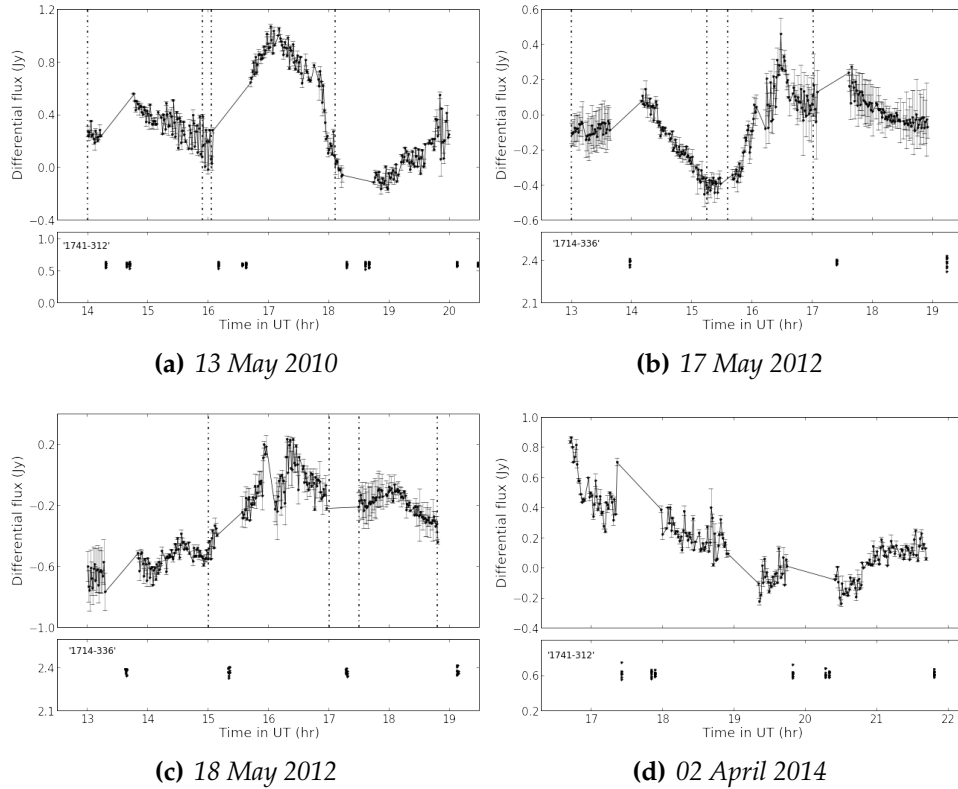


Figure 3.2: The differential light curves of Sgr A* with ATCA at 3mm for the days during which flares were detected. The top panel in each subfigure shows the differential flux density of Sgr A*, while the bottom panel shows the observed calibrator flux on that day. The data points between the vertical lines show the detected individual flares. A differential light curve from 02 April 2014 observation is shown as an example of smooth flux variation with no strong flare activity. No flares were observed during that day with their start and stop times within the observed time range and with peak amplitude in excess of 0.3 Jy.

3.4.1 Uncertainties

Given the nature of the light curves and significant spread in the values, it is necessary to distinguish between minor fluctuations and flare events. As discussed in Section 2, the uncertainties in the flux density variations were calculated by calculating the median deviation from the median flux. Hence, the resulting uncertainties characterize the estimates of the compact flux associated with Sgr A*, corrected for flux density contributions from more extended and spatially resolved structures within the mini-spiral. The derived uncertainties in the differential flux are of the order of 0.02 Jy, with the minimum value of 0.001 Jy and maximum value of 0.15 Jy, and the median value of 0.015 Jy. Thus to distinguish the significant flux excursions leading to genuine flare events, we require the variation to be of the order of at least 0.3 Jy. Smaller flux variations are considered to be too small to be significant, and are not considered flare events. The flares have characteristic timescales of ~ 100 – 150 minutes at 3mm wavelength (Mauerhan *et al.*, 2005). Thus excursions in the differential flux which last for significantly shorter or longer time periods than ~ 180 minutes are not considered as flaring events.

3.4.2 Flare events

13 May 2010:

We detected two flare events on 13 May 2010. The differential flux of Sgr A* increased by 0.4 Jy in 45 minutes, and then decreased slowly to 0.1 Jy in 1.25 hours. The flux increased again from 0.2 Jy to 1.0 Jy in 1 hour, followed by a decline back to 0 Jy. The flux variation of 0.8 Jy makes this as one of the strongest flare detected from all the observations.

17 May 2012:

Two instances of strong flux variation were detected on 17th May, 2012. For the first flare, the differential flux increased from 0.4 Jy to 0.7 Jy within 1 hour, and then decreased to 0.0 Jy. Following this was the second flare with a flux increase to 0.75 Jy in 45 minutes. The two flares are centered at 14:00 UT and 16:25 UT respectively.

18 May 2012:

We observed a strong flare was on 18 May 2012. The differential flux increased by 0.7 Jy within 1.5 hours before declining by 0.4 Jy. A slightly weaker second flare was also observed where a differential flux increase by 0.3 Jy was seen in 45 minutes which subsequently decreased to 0.0 Jy.

The 2013 and 2014 data:

We had scheduled our observations for 2013 and 2014 to monitor the flare activity of Sgr A* during the periaapse passage of the dusty S-cluster object (DSO/G2). DSO/G2 was which was discovered recently, and large flux variations were predicted during its flyby (Eckart *et al.* 2013; Valencia-S. *et al.* 2015, see Section 3.2.2 for details). During the 2013 campaign, heavy rainfall on 3 out of the 6 scheduled days caused loss of observation time, parts of the observation were affected by atmospheric turbulence on the rest of the three days, but we did not detect any significant excursion in the unaffected parts of the light curves. In 2014, we do not observe any significant flux variation on the flare time scales of ~ 100 – 150 minutes and no flares were observed with their start and end times within the observed time range.

The calibrator flux density has remained constant during all the observed flaring events. This supports our conclusions that the observed variations in the flux density originate from Sgr A*.

3.5 FLARE ANALYSIS

I have discussed various different models that have been used to explain the flaring of Sgr A* in section 3.2. For the analysis of the detected flares, I will use the expanding plasmon model, discussed in section 3.2.2

As we observe the flares as progression in time, the dependence of I_ν and τ_ν has to be converted from expansion factor to time. I assume that the blob expands uniformly at a constant speed so that the expansion radius R is a simple linear function of time, with a constant expansion speed of v_{exp} . This expansion of the radius is given by $R - R_0 = v_{\text{exp}}(t - t_0)$. The initial radius R_0 of the source component

is usually expressed in multiples of the Schwarzschild radius. One Schwarzschild radius corresponds to $R_s = 2GM/c^2 \sim 10^{10}$ m for a supermassive black hole of mass $\sim 4 \times 10^6 M_\odot$. This results in the velocity of light to be about 100 R_s per hour. At times $t < t_0$, the source optical depth is assumed to be equal to its frequency-dependent initial value τ_0 at $R=R_0$. For the optically thin part of the spectrum, there is an initial increase in flux as the source size increases at constant optical depth τ_0 and then decreases with decreasing optical depth as it expands. For $t > t_0$, an increase in the turnover frequency ν_0 or the initial source size R_0 shifts the decaying flank of the curve to later times, thus lengthening the duration of the flare. A decrease in the spectral index $\alpha_{\text{synch}} = (p-1)/2$ or peak flux density I_0 also has the same effect in the shape of the decaying flank of the curve, while increasing the adiabatic expansion velocity, ν_{exp} , shifts the peak of the light curve to earlier times. Flare timescales are longer at lower frequencies and have a slower decay rate, as a result of adiabatic expansion.

The uncertainties in the parameters values of the model are calculated from the reduced χ^2 fit values, by varying the parameters until the reduced χ^2 varied by 30%, which corresponds to 1σ uncertainty in the model parameters. For each source component, I use five parameters (I_0 , α_{synch} , R_0 , ν_0 , ν_{exp}), i.e. 5 degrees of freedom. The details of the models are described in the Table 2.

The synchrotron self-Compton (SSC) model has been used for the modeling of the NIR flares together with the adiabatically expanding plasmon model. This model assumes that the synchrotron and SSC components in the temporary accretion discs around the SMBH are upscattered by SSC processes to NIR/X-ray regime. Then the adiabatic expansion of these components results in the radio/sub-mm emission. Sabha *et al.* (2010) and Eckart *et al.* (2012) discuss the detailed formulation of this model. Using formalism, we can constrain the strength of the magnetic field as a function of the turnover frequency ν_m . The magnetic field is then given by $B \sim \theta^4 \nu_m^5 I_m^{-2}$. Here θ is the angular size of the synchrotron component, while I_m is the peak flux density at the turnover frequency.

The modeling of the 13 May 2010 flare:

I model the first flare with a source component of initial radius $1.67 R_s$. The expansion speed of the component was $0.015 c$. The obtained particle spectral index p and the turnover frequency were 2.2 and 469.2 GHz respectively.

Table 3.3: The parameters for the individual source components estimated from the adiabatically expanding plasmon model. See also [Borkar et al. \(2016\)](#) for details.

Date	Flare	v_{exp} [c]	S_{max} [Jy]	ν_{max} [GHz]	R_0 [R_s]	α_{synch}	χ^2 [G]
13 May 2010	A	0.015 ± 0.002	3.57 ± 0.21	469.2 ± 70.0	1.67 ± 0.06	0.60 ± 0.15	1.43
	B	0.021 ± 0.001	6.95 ± 0.29	378.73 ± 102.5	3.61 ± 0.03	0.77 ± 0.20	1.94
17 May 2012	C	0.0135 ± 0.002	5.19 ± 0.37	542.7 ± 67.4	1.60 ± 0.05	0.66 ± 0.21	1.76
	D	0.022 ± 0.003	7.45 ± 0.27	512.3 ± 57.1	1.67 ± 0.03	0.675 ± 0.30	2.06
18 May 2012	E	0.023 ± 0.004	7.73 ± 0.4	545.9 ± 72.0	2.27 ± 0.01	0.55 ± 0.32	1.98
	F	0.017 ± 0.003	6.25 ± 0.33	652.0 ± 81.5	1.35 ± 0.02	0.67 ± 0.23	2.16

The second flare observed on this day was modeled using a component of initial radius of $3.61 R_s$. The blob expands at the speed of $0.021 c$, and has a particle spectral index of 2.54. The turnover frequency is obtained from the fit is 378.7 GHz.

The modeling of the 17 May 2012 flare:

I observed two flaring events on this day. The first blob originates at 13:00 UT and reaches the peak intensity at 14:25 UT. From the fits, I obtain the expansion speed of the blob to be $0.0135 c$, the initial radius $1.60 R_s$ and the particle spectral index of 2.32 and the turnover frequency of 542.7 GHz.

For the second flare, the expansion speed for the source is assumed to be $0.022 c$, the particle index of 2.35. The turnover frequency was found to be 512.3 GHz and the initial radius of $1.67 R_s$.

The modeling of the 18 May 2012 flare:

The first flare detected on this day was modeled with the source component of radius $2.27 R_s$. This source has the expansion speed of $0.023 c$, particle index of 2.1 and the turnover frequency of 545.9 GHz. The second flare was fitted using a source component of size $1.35 R_s$ which expands at the speed of $0.017 c$. The spectral index and the turnover frequency of the blob was estimated to be 2.34 and 652.0 GHz respectively.

Table 3.3 shows the details of all the fitted parameters from the expanding plasmon model for all flare events. The Fig. 3.3 shows the modeled curves fitted to the

differential light curve data from our observations.

3.6 DISCUSSION

The NIR, submillimeter and radio flares of Sgr A* have been successfully explained using the adiabatically expanding plasmon model (Eckart *et al.*, 2006b, 2008; Yusef-Zadeh *et al.*, 2006a; Kunneriath *et al.*, 2010). From these modeling of the flares, it has been shown that the synchrotron emission is initially optically thick at radio & millimeter wavelengths, and optically thin at NIR and X-ray wavelengths. The turnover of the flare was shown to be occurring in the submillimeter region. The millimeter flares modeled using the adiabatically expanding modeling by Yusef-Zadeh *et al.* (2006b, 2008) predicts the turnover happening at frequencies ≥ 350 GHz. Kunneriath *et al.* (2010) and Eckart *et al.* (2012) also estimate similar values of the turnover frequency of around few hundred GHz. The turnover frequency defines the values of the initial blob radius R_0 and the particle spectral index p , which in turn determine the flux density in the optically thick and optically thin part of the spectrum. Higher values of v_0 in the THz regime have also been found which provide reasonable fits to the data. But they overestimate the particle spectral index and the peak flux densities at submillimeter wavelengths (Eckart *et al.*, 2008). The particle index of $1.5 \leq p \leq 3.5$ correctly predict the flux density at millimeter wavelength. The estimates of the parameters that I obtained from the modeling our data are fairly consistent with these values.

I obtain the expansion velocities of the blob of $0.013 - 0.025 c$. These are within the range of previous results (Eckart *et al.*, 2008; Yusef-Zadeh *et al.*, 2008; Li *et al.*, 2009). These values are an order of magnitude smaller than the values obtained from the relativistic sound speed in the absence of external pressure in the vicinity of the SMBH, which are estimated to be around $0.2 c$. The low expansion speeds that are obtained from the models imply that the expanding blob either has a higher bulk motion or it is confined to the vicinity of the SMBH in the form of a disc or a corona. The differential rotation within the accretion disk may cause shearing of the hot spot source component, which may explain the low expansion velocities.

3.6.1 No detection of DSO-induced activity

Recently, a fast moving source was detected as an infrared excess approaching the central black hole, which is called G2/DSO (Gillessen *et al.*, 2012, 2013; Eckart *et al.*,

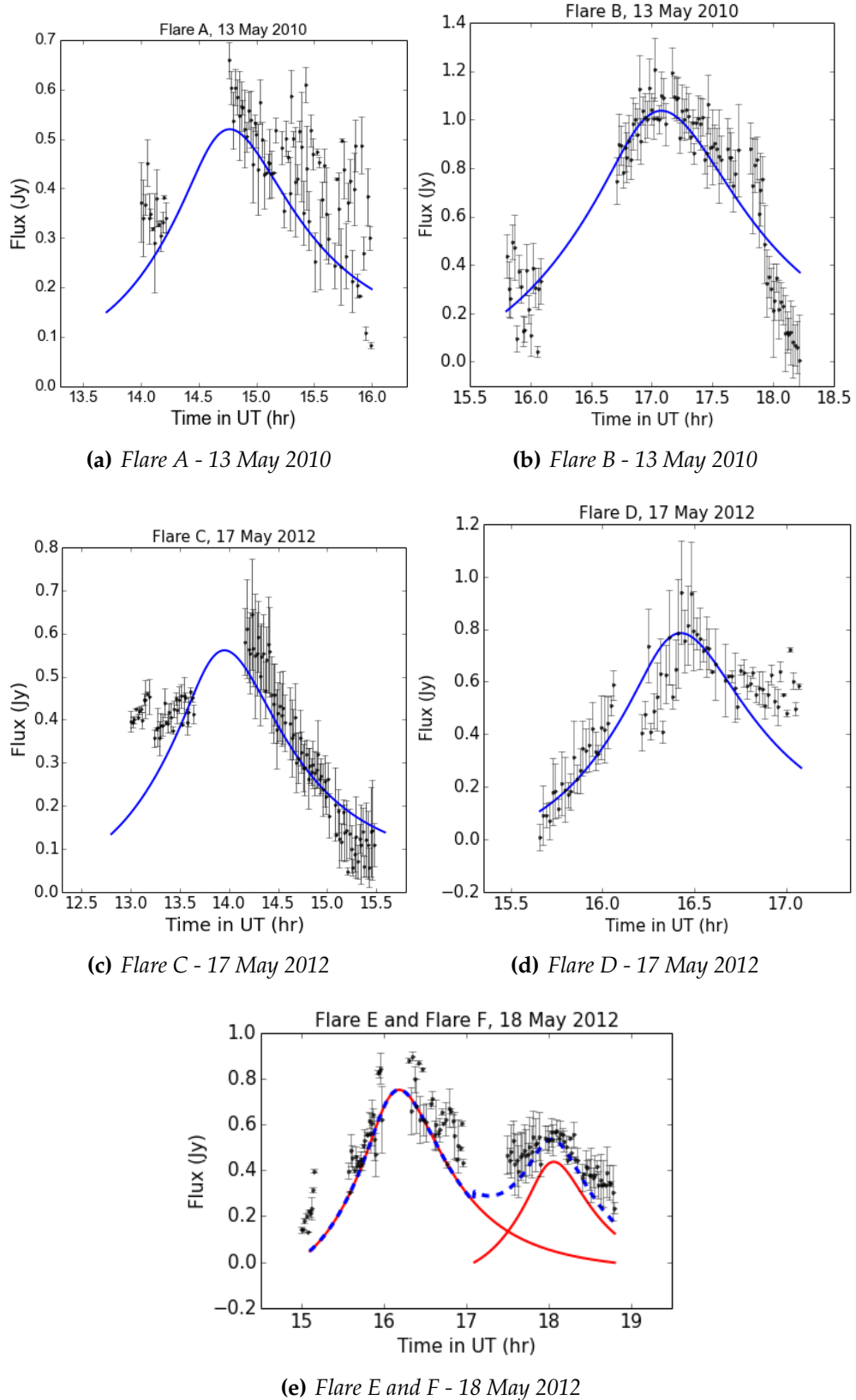


Figure 3.3: The fitted models for the detected flares. The black curve denotes observed differential flux points. The individual flares are shown by red curve. In case of multiple sub-flares, the individual flares are shown by red curve and the blue dotted curve shows the combined fitted model. See also [Borkar et al. \(2016\)](#) for details.

2013). This new visitor has renewed attention towards the GC and has sparked several multiwavelength observation campaigns of the GC. The origin and the nature of this source has been a matter of debate as several theories have been put forward to explain this enigmatic source. The infrared excess of the source has led to the postulation that this source consists of dominant fraction of gas and dust (Gillessen *et al.*, 2012, 2013; Pfuhl *et al.*, 2015). While its NIR/MIR spectrum also allow for the contribution from a stellar component which has been favored by others (Eckart *et al.* 2013; Murray-Clay and Loeb 2012; Scoville and Burkert 2013; Ballone *et al.* 2013; Phifer *et al.* 2013; Jalali *et al.* 2014). The spectroscopic measurements predicted the periape passage of the object in 2014. A blue-shifted Br- γ emission from the DSO has been detected by Pfuhl *et al.* (2015) in their April 2014 dataset. Valencia-S. *et al.* (2015) detect a blue-shifted emission in their observations after May 2014. They conclude that the DSO has remained spatially compact. The L' band observations by Witzel *et al.* (2014) also find that the DSO has maintained the compact shape and remained in a Keplerian orbit.

Given that the flyby of the DSO would lead to the extra amount of cold material that would reach the SMBH vicinity, this was predicted to affect the flaring activity of Sgr A* significantly. Computational models describing the flyby event suggested that if the DSO develops a bow shock then it may lead to shock acceleration of electrons and this in turn may cause strong flares in radio emission. The strength of the flares would depend on the size of the bow shock. The initial estimates from the computational models predicted that the excursions in the flux at centimeter wavelengths would be of the order of 1 – 20 Jy. These estimates were later revised which then put the values of the order of 0.01 – 0.2 Jy (Narayan *et al.* 2012; Sądowski *et al.* 2013; Crumley and Kumar 2013). These values are well within the range of the normal flux variations of Sgr A*, thus making it difficult to study the effects of the flyby on the flaring of Sgr A*.

So far, there have been several observational campaigns at different wavelengths during the period of the flyby. These observations did not reveal any deviation from the regular flaring activity of Sgr A*. Three flares of few mJy strength were detected during the NIR observations by Valencia-S. *et al.* (2015) with SINFONI during 2013-2014, where no exceptional flaring activity was found. A shock-heated gas would give rise to increased continuum flux density or extraordinary variability in the ≥ 2 keV band in X-ray regime, but no such variability was detected (Haggard *et al.*, 2014). Monitoring of the GC with the VLA did not provide any de-

tectable strong radio flares. The current estimated variability would be within the normal range of flux density variations of Sgr A* (Sjouwerman and Chandler 2014).

My observations of the Galactic Centre with ATCA in 2013-2014 do not lead to any detection of significant variation in the flaring activity of Sgr A* in that period. No flux density variation were detected in the light-curves within the characteristic flare time-scales for the observations taken during the approach of the DSO towards periape. This is consistent with the compact blue-shifted Br- γ emission of the DSO observed in the NIR imaging. If there is a higher mass stellar source present at the center of the DSO, then it would imply that the DSO would retain its compactness through the flyby as the dust and gaseous material surrounding the central core would be largely unaffected from the gravitational pull of Sgr A* and would not cause large excursions in flux density. On the other hand, if the central source has the mass of about one solar mass, then it may be able to lose a large part of its gas and dust to fall onto Sgr A*. However, for a very short time scale during and right after the periape passage, it is not certain whether the gas close to the central source will remain in the Roche lobe of the star. Given that the distance of approach of the DSO is very short during the periape around the SMBH, and it will take several years for the gas to fall in to the black hole, it is unclear whether the flyby would lead to any exceptional flaring activity.

(Parts of this chapter were published in the paper Borkar *et al.* (2016) *Monitoring the Galactic Centre with ATCA at 3mm.*)

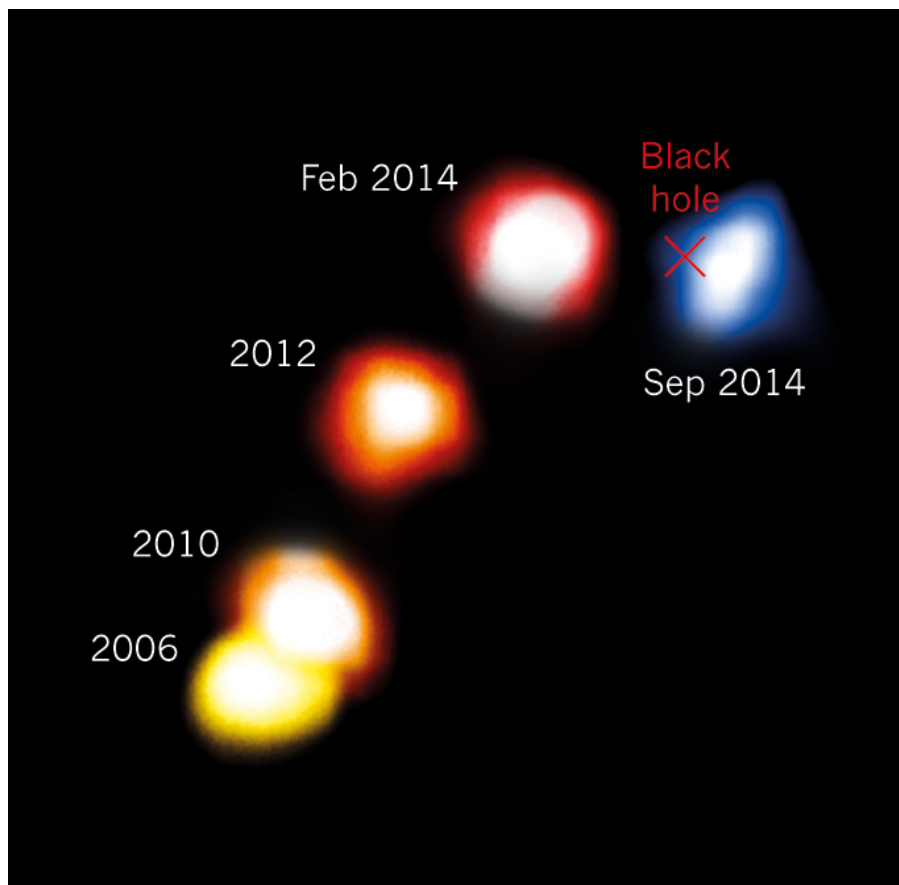


Figure 3.4: The DSO/G2 observed at different times along its trajectory towards Sgr A*, showing the detection of redshifted and blueshifted parts, as it underwent periapse in May 2014. Image: [ESO/Valencia-S. et al. \(2015\)](#)

THE VILLAIN'S MINIONS: SiO MASERS IN THE CENTRAL PARSEC

“It is known that there are an infinite number of worlds, simply because there is an infinite amount of space for them to be in. However, not every one of them is inhabited. Therefore, there must be a finite number of inhabited worlds. Any finite number divided by infinity is as near to nothing as makes no odds, so the average population of all the planets in the Universe can be said to be zero. From this it follows that the population of the whole Universe is also zero, and that any people you may meet from time to time are merely the products of a deranged imagination.”

— Douglas Adams, *The Restaurant at the End of the Universe*

4.1 INTRODUCTION

Masers are a type of line emission akin to lasers. Maser stands for Microwave Amplification by Stimulated Emission of Radiation. Stimulated emission was theorized by Albert Einstein in 1916 ([Einstein 1916](#)), and the first artificial maser was constructed by Gordon, Zieger and Townes in 1953 ([Gordon et al. 1955](#)). A maser is caused by the stimulated emission of photons when an electron in a higher energy state makes a transition to a lower energy state without absorbing the incident

photon. The emitted photon is identical to the incident photon in all respect, in phase, frequency, polarization and direction. This is an inverse process of absorption of radiation from lower level electrons to jump to the higher quantum energy level. Normally, the absorption process dominates the emission, but presence of population inversion allows for stimulated emission to dominate the absorption of radiation, and this leads to a sustained maser. The stimulated emission removes particles from the inverted population, and thus limiting the maser effect.

Astronomical masers were initially thought to be impossible, as it was thought that no natural environment existed that would produce the same effect, as the construction of maser device requires significant effort on Earth. It is now known that in astronomical objects, the population inversion is caused by pumping mechanisms such as infrared radiation and collisions, that give rise to astronomical masers. The Astrophysical masers were first discovered in 1965 (Weaver *et al.*, 1965) associated with the 1665MHz line of the OH molecule. 50 years later, we now know thousands of astronomical masers. Some of the prominent astronomical maser molecules are OH, H₂O, SiO, NH₃, HCN, SiS, H₂CO etc. These are prominently found in stellar atmospheres, star forming regions, planetary systems and comets, and extragalactic sources which result in a phenomenon called as *mega-maser*.

The SiO masers are mainly associated with stars and star forming regions. The SiO masers involve rotational energy states in the vibrational levels of the molecule. These states have energies high above the ground state, and thus high population in these states can only be sustained only close to the star where excitation levels are high. SiO maser emission has been observed in several transition lines towards oxygen rich asymptotic giant branch (AGB) stars and supergiants. The AGB phase occurs late in the life of a star when its diameter increases substantially due to helium fusion, and the star becomes a bright, red giant. The VLBI observations have shown that the SiO masers originate close to the photosphere of the star, at a distance of 10^{14} cm. Other maser sources, such as H₂, and OH masers are found in cooler outer regions of the stars. The infrared radiation from the star is the main source of pumping mechanism in these stars, though shock waves arising from nonlinear pulsation of the stars may also play a part in The SiO masers are known to be associated with long period variable stars, whose variability is of the order of few months, and the SiO emission is stable on short time scales.

Since the SiO masers are located within the innermost regions of the circum-

stellar envelopes (within few AU), they can be treated as point-like sources that are not subject to non-gravitational perturbations such as magnetic fields and stellar winds. The inner parts of the Galaxy have been surveyed for SiO maser sources extensively, especially at 43 GHz, in order to study the structure and dynamics of the stellar disk. Since SiO emission is related to the infrared radiation from the stars, they are also strong IR sources. And as these objects are strongly visible in both radio and IR wavelengths, their radio positions from Sgr A* have been used to accurately measure the astrometry of IR sources with an accuracy of ~ 1 mas (Menten *et al.*, 1997; Reid *et al.*, 2003, 2007). As Sgr A* is bright at radio wavelengths but dim at IR wavelengths, accurate measurement of its position in the IR maps is difficult, where the confusion due to surrounding stellar sources hinders the measurement of emission from Sgr A*. The SiO maser sources have been used to create accurate frame of reference in both radio and IR bands to determine the precise position of Sgr A* in IR. Measurements of three-dimensional velocities of the SiO masers at 4 GHz also provided the lower limit on the enclosed mass within the given radius.

Although the GC has been observed extensively at 43 GHz (Izumiura *et al.*, 1998; Miyazaki *et al.*, 2001; Deguchi *et al.*, 2000a,b, 2002; Sjouwerman *et al.*, 2002, 2004; Imai *et al.*, 2002; Yusef-Zadeh *et al.*, 2015a; Menten *et al.*, 1997; Reid *et al.*, 2003, 2007; Oyama *et al.*, 2008; Li *et al.*, 2010), the 86 GHz regime still remains largely unexplored. There have been few observations of the inner Galaxy at 86 GHz. Lindqvist *et al.* (1991) observed the inner Galaxy with the Nobeyama 45 m telescope, but failed to detect with significance any 86 GHz maser sources. Messineo *et al.* (2002) observed the GC with the IRAM 30 m telescope and detected 271 SiO masers, with 255 new detections. The central parsec of the Galaxy has been observed by Li *et al.* (2010) with the ATCA between 2006 and 2008, where they detected two sources at 86 GHz. Apart from this, there haven't been high resolutions radio interferometric observations of the central parsec of the Galaxy at 86 GHz.

Our observations of the GC with the ATCA telescope at 86 GHz are the most extensive observations at this wavelength, spanning 5 years, from 2010 to 2014. The telescope backend was upgraded in 2009 (see section 2.3 for details) which allows us to observe at two different bands with 2 GHz bandwidth each, as compared to 128 MHz for pre-2009 observations. The observations before the upgrade were thus restricted in velocity coverage, but the upgrade now allows us to detect high velocity stars. In the next section, I will discuss the procedure I have used to detect SiO masers, and method to obtain their positions and proper motions.

4.2 DATA ANALYSIS

After initial basic data reduction and calibrations (see section 2.3.3 for details), I created the continuum map of the central parsec from the visibilities. I found the continuum levels by fitting a 1 dimensional fit to the line-free channels. This was then subtracted from the line data using the MIRIAD task UVLIN. This is known as the continuum-subtracted data, from which I constructed a spectral-line cube. Further analysis on the data cube was performed with softwares such as QFitsView and dpuser.

Each spectral channel forms a two-dimensional image, with subtracted Sgr A* at its center, with an offset of ± 20 arcsec in right ascension (RA) and declination (DEC) on either side of the center. To detect SiO masers, I first calculated rms noise (σ) for each channel. Then I searched for all the instances where the flux density was more than 5σ . These resulted in several candidates for the SiO masers. To differentiate between the real sources from the spurious detections as well as instrumental and procedural artifacts, additional constraints were put: the candidate should be detected over several epochs, and for weaker detections, they should have a Gaussian spectral profile, i.e., they should be detected over several channels. I also referred to the lists of previously known stellar sources in the central parsec observed at 43 GHz and in IR observations (Viehmann *et al.*, 2005; Reid *et al.*, 2007; Li *et al.*, 2010) to verify the positions of detected candidates.

After rejecting spurious detections, and cross-verifying previously known sources, 11 sources were confirmed. Of these, following are known sources: IRS 1W, IRS 2L, IRS 7, IRS 9, IRS 10EE, IRS 12N, IRS 28, and IRS 34. Three new sources were also detected, which I have named as 'SiO New 1', 'SiO New 2', and 'SiO New 3'.

4.2.1 Calculating positions and proper motions

As I have discussed in section 2.3, the longest baseline available for observation with ATCA is ~ 300 m, which translates to best possible angular resolution of $0.2''$. This is significantly lower resolution than the resolution available with VLBA at 43 GHz. Thus to improve the accuracy in the position, we fit a two dimensional Gaussian to each detected source in each channel. These channels are then averaged by variance weighting to give the position of the SiO maser for the observation day.

To calculate the proper motions of the masers, I assume that the positions of the stars don't change within short period (\sim days), and thus I can average the positions I have obtained from two dimensional Gaussian fitting to deduce the precise position of the maser in that year. The mean position for a particular year is obtained by variance weighted averaging the positions obtained for each individual observation day. I then fit a variance weighted straight line through the resultant positions to obtain the proper motions. The data from Reid *et al.* (2007) has been used to improve the fit of the data. The detailed values of obtained positions, images and spectra of individual maser sources can be found in the appendix B. Since there is a large scatter and error their data, I do not include Li *et al.* (2010) position measurements in the calculations.

The following figures show the resultant proper motions of each maser source. In each image, the red triangles represent the data from Reid *et al.* (2007), while the blue squares represent the positions obtained from my data. Although I have managed to get subpixel accuracy to the positions of masers, the intrinsic instrumental low resolution (compared to Reid *et al.* (2007)) means that there is still some scatter in the obtained positions, which affects the calculations of their proper motion. For some of the sources, such as IRS 1W, and the three newly discovered sources, prior high resolution data was not available. Also, the flux density of these sources is low, and they appear elongated and extended in the maps, thus it is difficult to compute precise measurements of their positions and proper motions, resulting in large scatter. Sources with high flux density, such as IRS 7, IRS 9, IRS 10 EE, IRS 12N lie closer to the fitted line and follow the general proper motion trend, albeit the scatter. IRS 2L is has moderate flux density so that it's position can be measured with good accuracy and its proper motion can be calculated. The source IRS 34 was not detected over many observation days, thus its proper motions could not be calculated. The table 4.1 gives the detailed values of proper motions of the strong sources in mas/yr and in km/s.

4.3 DISCUSSION

The central stellar cluster of the GC has been observed at various wavelengths for long period. The multiwavelength observations, especially at NIR and mid-IR wavelength regimes, have been used for not only calculating the precise positions of the IR sources (IRs), but they have also been used to determine their SEDs, and from these, their morphology has been determined. Here I will give a brief

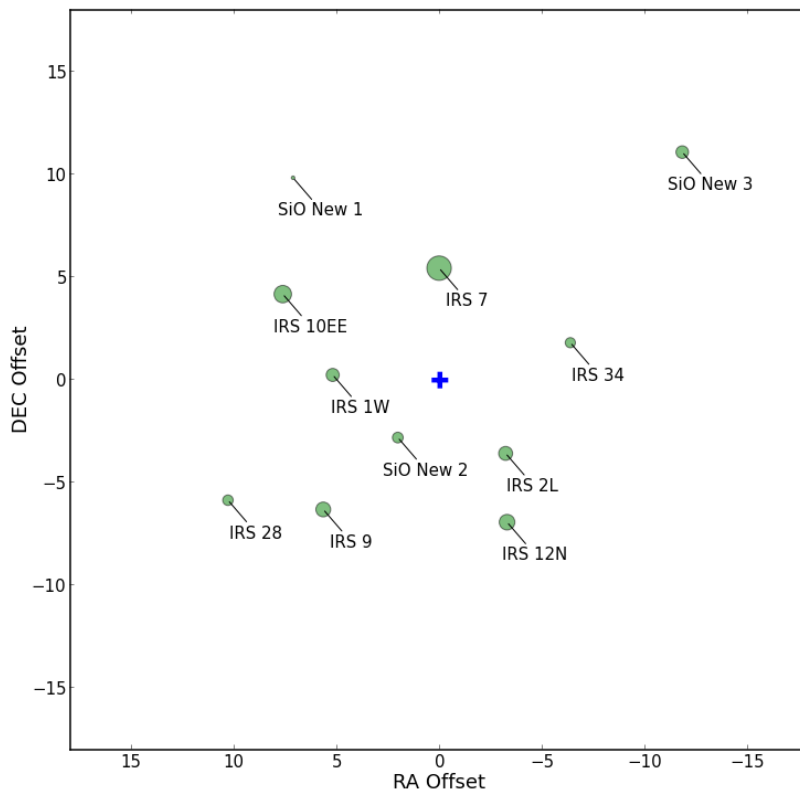


Figure 4.1: Positions of all the detected SiO masers. The size of the circle is proportional to the flux density of the corresponding SiO maser. The blue '+' marks the position of Sgr A*.

Table 4.1: SiO maser proper motions for strong sources

Source ID	V_{LSR} <i>km/s</i>	μ_{RA} <i>mas/yr</i>	μ_{DEC} <i>mas/yr</i>	v_{RA} <i>km/s</i>	v_{DEC} <i>km/s</i>
IRS 7	-114.37	-0.14	-7.26	-5.48	-241.1
IRS 9	-340.75	2.5	3.0	97.85	117.42
IRS 10EE	-27.8	0.05	-2.1	1.96	-82.19
IRS 12N	-62.59	-1.3	-2.5	-50.88	-97.85
IRS 2L	-444.43	-18.65	16.04	-729.96	627.8

overview of these studies.

IRS 1W:

IRS 1W is located in the Northern Arm of the mini-spiral and has been observed in both radio and IR bands. It is known to be a bow-shock source which might be produced by the flow of dust and gas along the northern arm encountering the wind from the central star. It is experiencing rapid mass loss, thus it is thought to be either a Wolf-Rayet star or an AGB star (Tanner *et al.*, 2002, 2005).

IRS 7:

IRS 7 is a very strong radio and IR source which has been used for pointing for IR observations. It is classified as M-type supergiant Mira variable star with high thermal radio emission from its external envelope. It has a supergiant luminosity with its SiO maser features spread over more than 20km s^{-1} , which means that its envelope is much larger than typical Mira variable stars, with strongest features spanning about 10 mas.

IRS 9:

IRS 9 is shown to have characteristics of a Mira variable star, with slow period variability (Reid *et al.*, 2007). A binary system was postulated to explain its high velocity, but Reid *et al.* (2007) show that the contribution to the velocity from the binary could not be more than 20 km s^{-1} , and thus it could not explain the high ve-

locity. They also argue that it is unlikely that IRS 9 is a newly-ejected high velocity star due to close encounter with Sgr A*.

IRS 10EE:

From the IR observations, IRS 10EE has been shown to be a long-period variable star, with variability ranging from several days to few months (Tamura *et al.*, 1996; Wood *et al.*, 1998; Ott *et al.*, 1999; Peeples *et al.*, 2007). It has also been observed at different maser lines, such as SiO, OH, and H₂O (Lindqvist *et al.*, 1990, 1992; Menten *et al.*, 1997; Sjouwerman *et al.*, 2002; Reid *et al.*, 2003, 2007; Oyama *et al.*, 2008; Peeples *et al.*, 2007). It has been proposed that it could be a binary system (Peeples *et al.*, 2007), which has been supported by VLBA observations (Oyama *et al.*, 2008). Li *et al.* (2010) detect variation on the timescale of months at 86 GHz. Since our observations are spaced every one year, this shorter variability is not detected in our data. It also has a very compact SiO emission.

IRS 12N:

IRS 12N has been observed at both IR and radio wavelengths, though it has a discrepancy between the IR and radio motions, possibly due to confusion due to blending with other stars in the IR band. Similar to IRS 10EE, it has a very compact emission, and it has been classified as a cool red giant star (Viehmann *et al.*, 2005), possibly a Mira variable star.

IRS 28:

There have been several observations of IRS 28. The infrared observations have shown that it is variable over the period of 1 – 2 years, similar to IRS 12N, which is consistent with our observations (Tamura *et al.*, 1996). This suggests that IRS 28 could also be a cool red giant star.

IRS 34:

Viehmann *et al.* (2005) classify IRS 34 as an HE I star. Although it has not been observed in our dataset for several observation days, for the days it has been observed, it does not show any significant variability.

Reid *et al.* (2007) and Li *et al.* (2010) have detected several new SiO maser sources apart from the well known IR sources (IRSs) at 43 GHz, with a combined total of 23 new sources. These sources are not detected in our images. Some of the sources are outside our field of view, and thus are not observed. For the sources that are within our field of view, the peak flux densities at 43 GHz range from 0.015 Jy to ~ 0.1 Jy. Since the 43 GHz transition is usually (though not always) stronger than the 86 GHz transition, the corresponding peak flux density for these sources would be much lower, where it would fall within $1 - 3\sigma$ of the rms noise, where $1\sigma = 0.015 - 0.020$ Jy. Thus most of these sources are not detected in our dataset.

4.3.1 Variability of SiO masers

The SiO masers are associated with long period variable stars, such as AGB stars. These stars are generally pulsating, cool giants stars belonging to the asymptotic giant branch. In general, they have been known to have the variability of from few days to thousand days or more, and the period of variability may not be strongly defined, and some times may be completely irregular. It is known that the SiO variability and the infrared variability of a maser are correlated, and these are related to the variation in the local heating rate due to underlying stellar pulsation, usually dominated by the radiative processes (Elitzur, 1992). Our continuous monitoring of the GC allows us to study the variability of the SiO masers in the central parsec.

The detailed values of the flux densities observed - for each observation day when the source was detected - are given in the appendix A. The flux values are consistent within the measurement accuracy and rms noise for the same observation period (\sim few days), but the values can be seen to vary significantly over longer periods. Some of the sources show a periodic behaviour while others show monotonic increase or decrease in the peak flux density. Sources such as IRS 7, IRS 12 N, and IRS 28 exhibit a variation period of the order of two years, while IRS 1W, IRS 9, and IRS 10EE show a gradual decrease in the peak flux density. IRS 7 is known to be a Mira variable star. The Mira variable stars show strong variability of the order of few hundred days where their flux density in IR may change by more than a magnitude. Since the SiO variability is directly correlated with the IR variability, strong changes in the peak flux density are also expected at the SiO transition lines. The remaining sources, such as IRS 2L, and the three newly detected masers show a steady stable peak flux density.

We can also see that the brighter the source, more the difference between the

highest and lowest observed peak flux density. Thus we may speculate that the weaker sources that exhibit a stable flux might have a weakly defined period or their variability may be irregular.

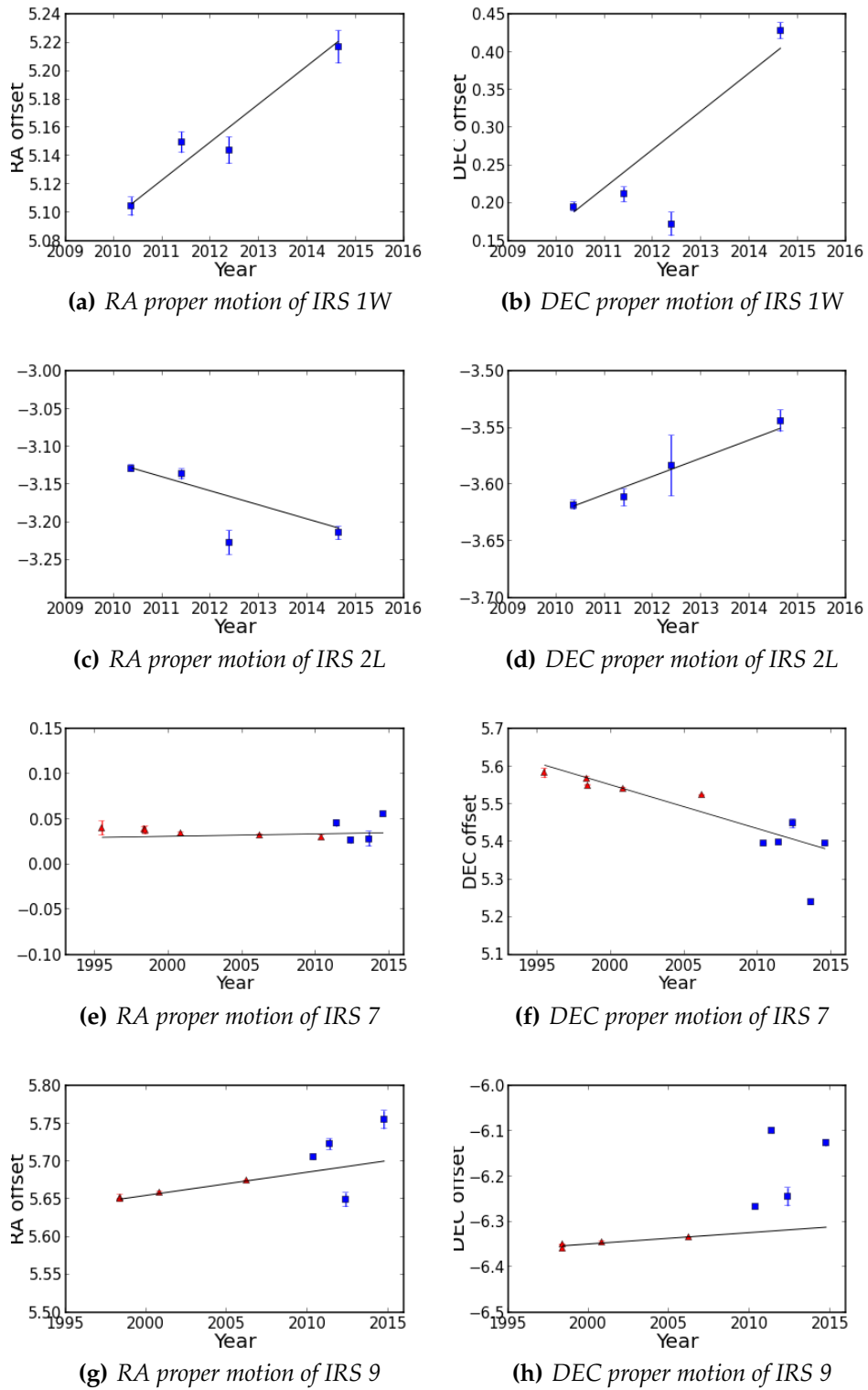


Figure 4.2: The RA and DEC proper motion of IRS 1W, IRS 2L, IRS 7 and IRS 9.

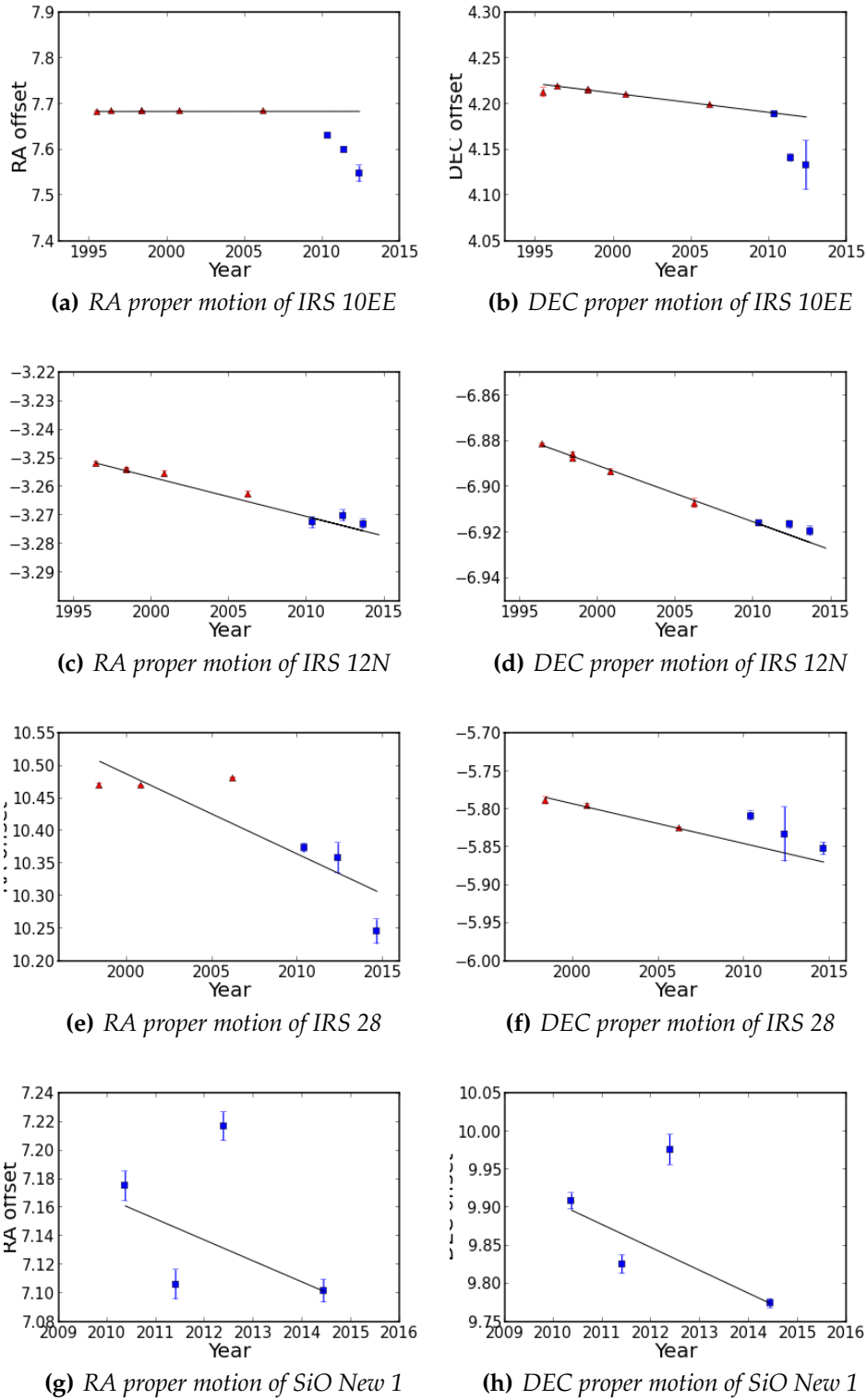


Figure 4.3: The RA and DEC proper motion of IRS 10EE, IRS 12N, IRS 28 and SiO New 1.

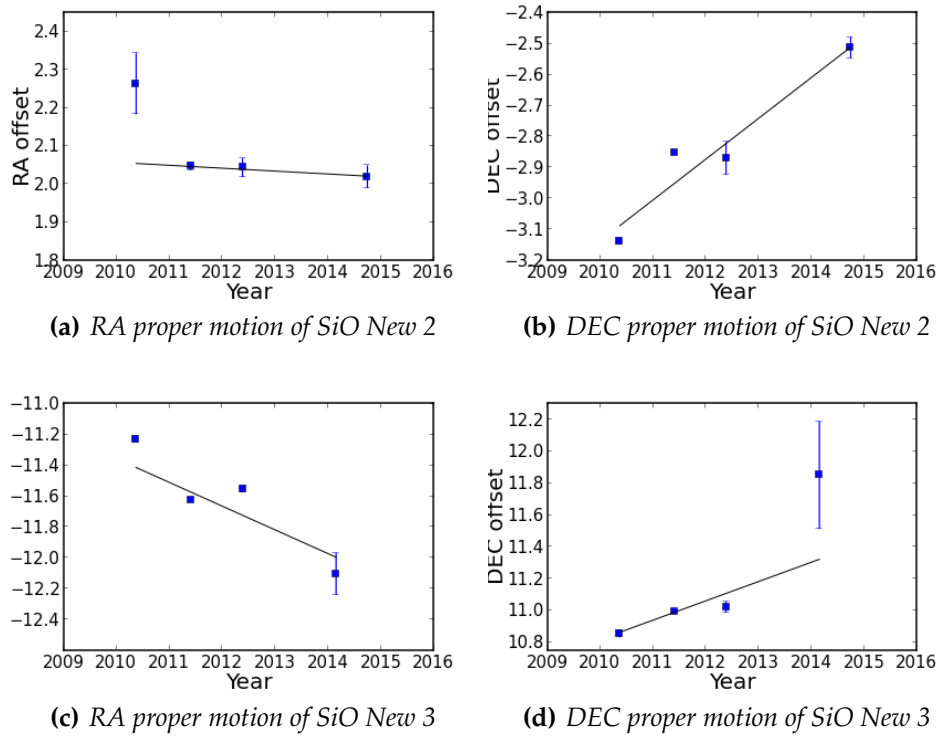


Figure 4.4: The RA and DEC proper motion of SiO New 2, and SiO New 3.

SUMMARY

“The Answer to the Great Question of Life, the Universe and Everything is 42.”

— Douglas Adams, *The Hitchhikers Guide to the Galaxy*

In this chapter I will summarize the main results of my Ph.D. thesis. The thesis was about the 3 mm observations of the Galactic Center with the ATCA telescope. Although the GC has been observed extensively at various wavelengths, the 3 mm regime has not been fully explored. Observed with the upgraded backend, and spanning 5 years, this is the largest set of interferometric observations of the at 3 mm wavelength.

I began the thesis by providing the details about observations and basic data reduction concepts. Since the antenna 6 is unavailable for 3 mm observations, the resolution of the telescope is limited, which leads to significant contribution to the flux density of Sgr A* from the diffuse emission from the surrounding extended sources, such as the mini-spiral. To avoid this contribution, and to get rid of the contributions from atmospheric and instrumental effects, I use the method developed by [Kunneriath *et al.* \(2010\)](#). Using this method, I subtract the median flux density of each year from the flux density of individual observation day. This gives

us the differential flux of Sgr A* which is largely free of aforementioned contributions, and it can be attributed to Sgr A* itself.

I detected three instances of variability in the flux density of Sgr A*. I use the adiabatically expanding model involving synchrotron source components, to obtain the spectral index values, the source size, the expansion velocities, the turnover frequencies and the magnetic field. These values are consistent with the previously published results of the variability studies. The flares occur for 1.5 – 3 hrs, with the source of size ~ 1 Schwarzschild radius expanding at the speed of $\sim 0.013 - 0.025 c$. The synchrotron emission peaks at few hundred GHz in the sub-mm region, with the spectral index of 0.5 – 0.8.

The observations in 2013 and 2014 were carried out in order to monitor the effects of the flyby of the dusty S-cluster object (DSO/G2). From our observations, we do not detect any exceptional activity during the periapse passage of DSO, which is consistent with the multiwavelength observations carried out during the same period. This result supports the hypothesis that the DSO might have a stellar nucleus. It is yet unclear as to how much effect will the flyby of DSO have on the flaring of Sgr A*, and further monitoring is necessary to study the effects.

Simultaneous observations from radio/submm to NIR/X-ray regimes are required to better constrain the parameters of expanding source. At millimeter/submillimeter wavelengths, the current telescopes, such as ATCA, ALMA, the upgraded Jansky VLA etc. can be used in combination with the NIR telescopes, such as the VLT and Keck telescope to better understand the physics of accretion and flaring of Sgr A*. The Event Horizon telescope will be able to observe the extreme details of Sgr A*, and help us understand the flaring mechanisms. It will also be useful in the search of a possible jet or an outflow from Sgr A*, and would be able to test different flaring models and theories of emission from the SMBH.

In the second part of the thesis, I presented the observations of the stellar cluster within the central parsec of the GC. The improved backend allows us to observe with 2 GHz bandwidth centered around two transition lines of the SiO molecule, and thus enables us for the observations of high velocity stars in the GC. I discussed the methods I used to detect the SiO maser sources, wherein I detected 11 SiO masers in the data, out of which 3 are new detections. I present the method used to obtain subpixel accuracy on the position measurements of the masers, and

calculating their proper motions. Although I obtain subpixel accuracy on the measurements, it is lower than the accuracy available with VLA and VLBA. Thus, there is some scatter in the position measurements. The measurements of the proper motion are in agreement with previous studies.

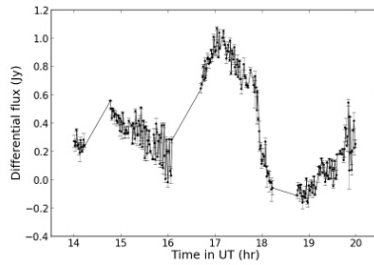
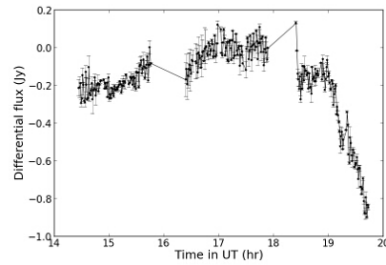
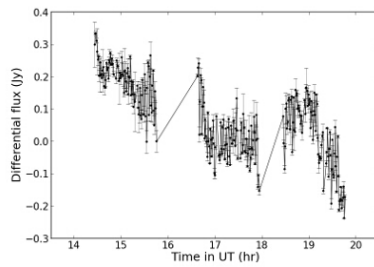
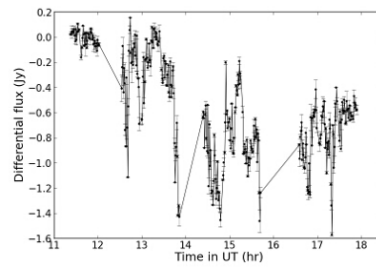
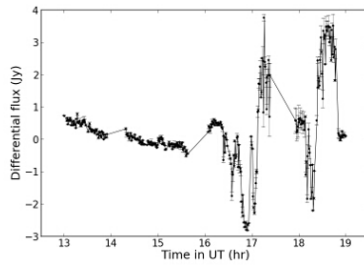
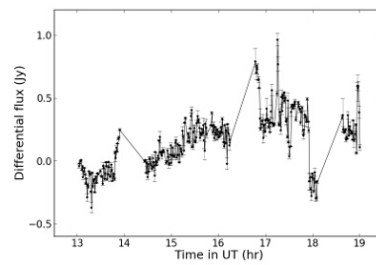
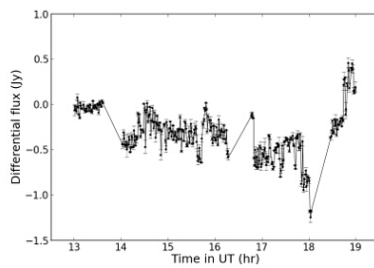
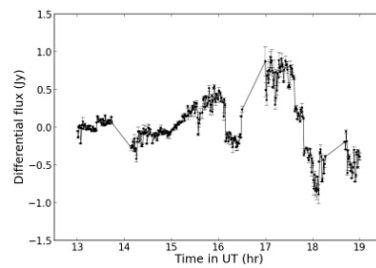
Most of the detected masers belong to the asymptotic giant branch of stars, some of which are cool red giants, Mira variable stars, and bow shock sources. The 86 GHz regime has not been fully explored with high resolution telescopes. High angular resolution observations at this wavelength would be able to identify the new sources, and discover further more sources in the central parsec. VLBI observations at 3 mm will be able to provide high accuracy on the position and proper motions of the masers, which in turn would help us to constrain the physical parameters of Sgr A*. Recently, several young stellar object (YSO) candidates were detected by [Yusef-Zadeh *et al.* \(2015b\)](#) using the VLA and ALMA. Similar observations with millimeter and submillimeter telescopes, such as ATCA, VLA, ALMA, SMA, and the upcoming SKA will be able to discover more YSO candidates, and will help us understand the nature of the central stellar disk.

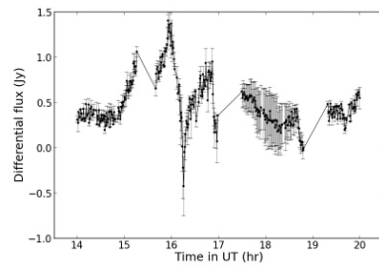


APPENDIX

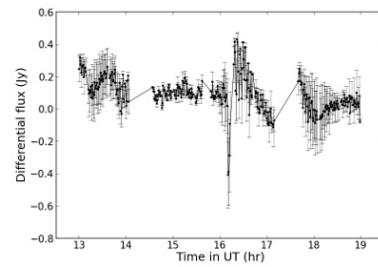
A.1 3 MM DIFFERENTIAL FLUX DENSITY CURVES OF SGR A*

The individual differential flux density curves at 3mm for all the observations from 2010 to 2014 are provided here.

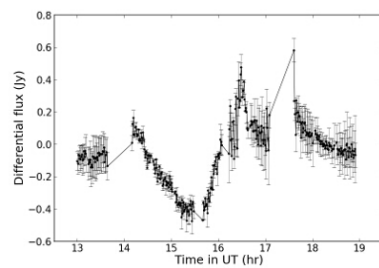
**(a)** 13 May 2010**(b)** 14 May 2010**(c)** 15 May 2010**(d)** 16 May 2010**(e)** 23 May 2011**(f)** 24 May 2011**(g)** 25 May 2011**(h)** 26 May 2011



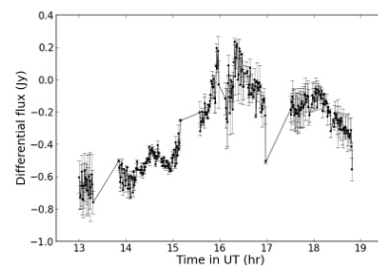
(a) 15 May 2012



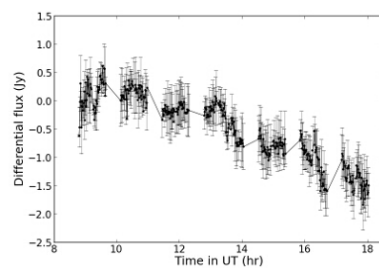
(b) 16 May 2012



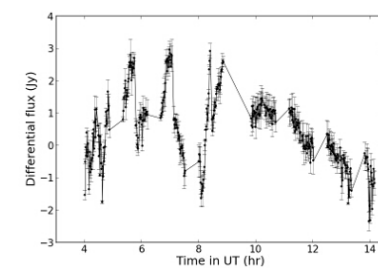
(c) 17 May 2012



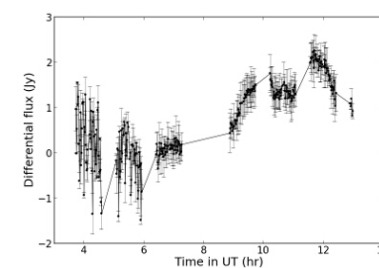
(d) 18 May 2012



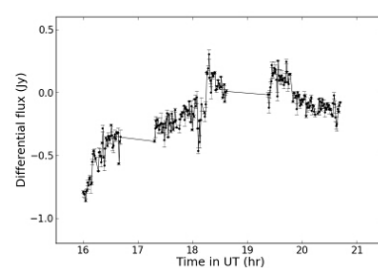
(e) 26 June 2013



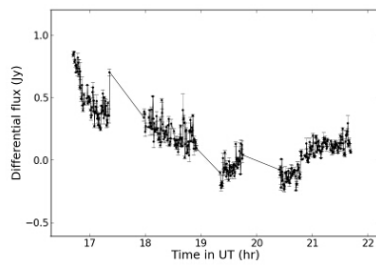
(f) 31 August 2013



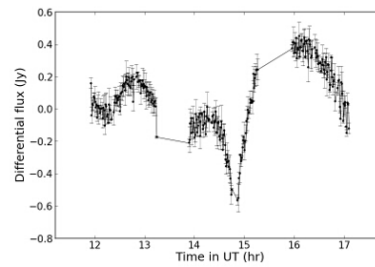
(g) 14 September 2013



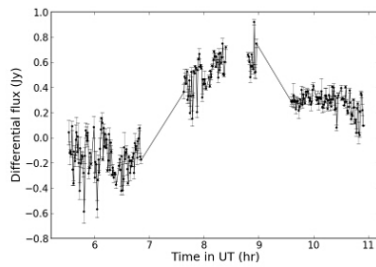
(h) 01 April 2014



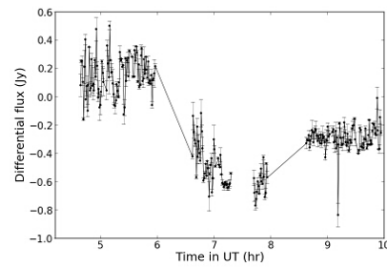
(a) 02 April 2014



(b) 07 June 2014



(c) 26 September 2014



(d) 27 September 2014

A.2 IMAGES AND SPECTRA OF SiO MASERS

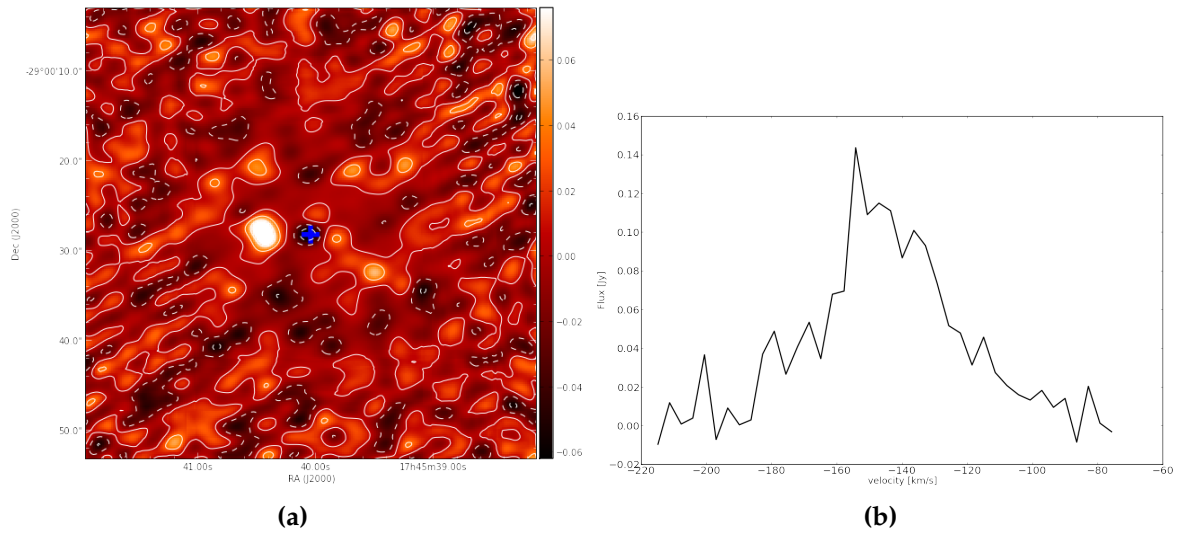


Figure A.1: Image and spectrum of IRS 1W

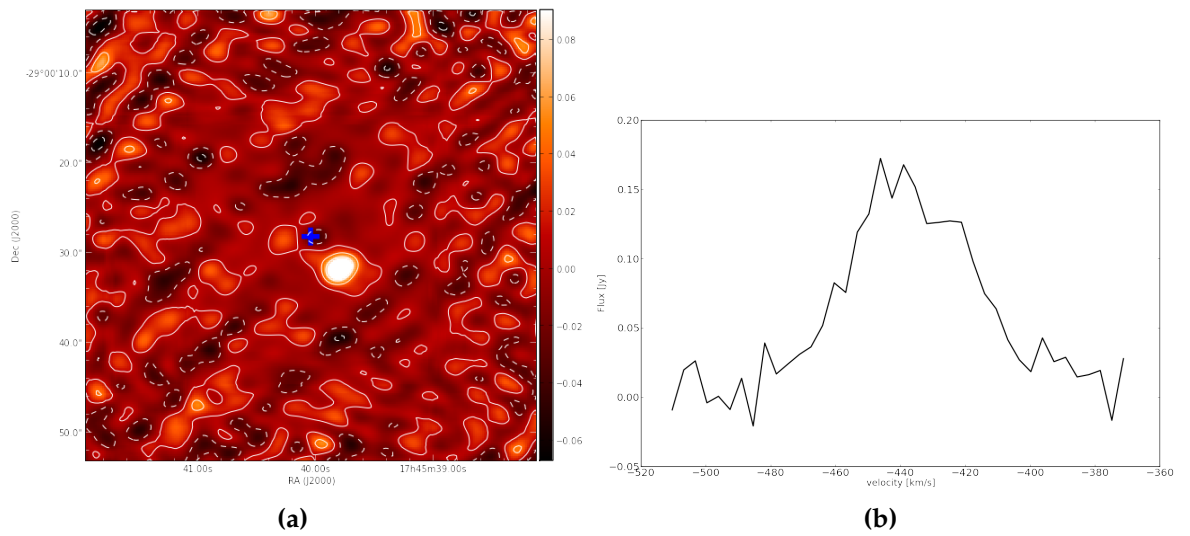


Figure A.2: Image and spectrum of IRS 2L

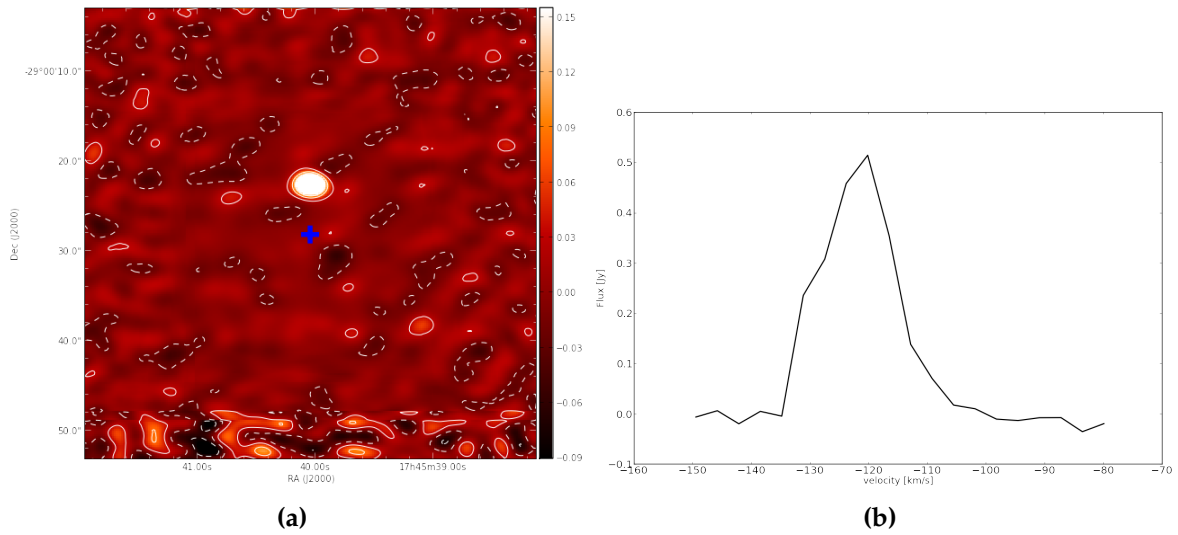


Figure A.3: Image and spectrum of IRS 7

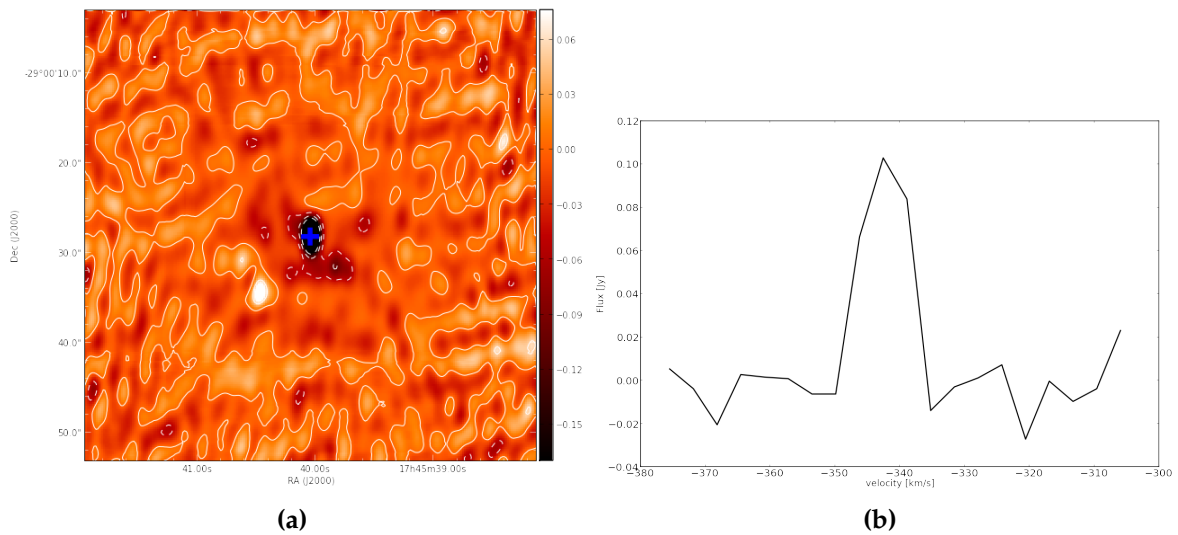


Figure A.4: Image and spectrum of IRS 9

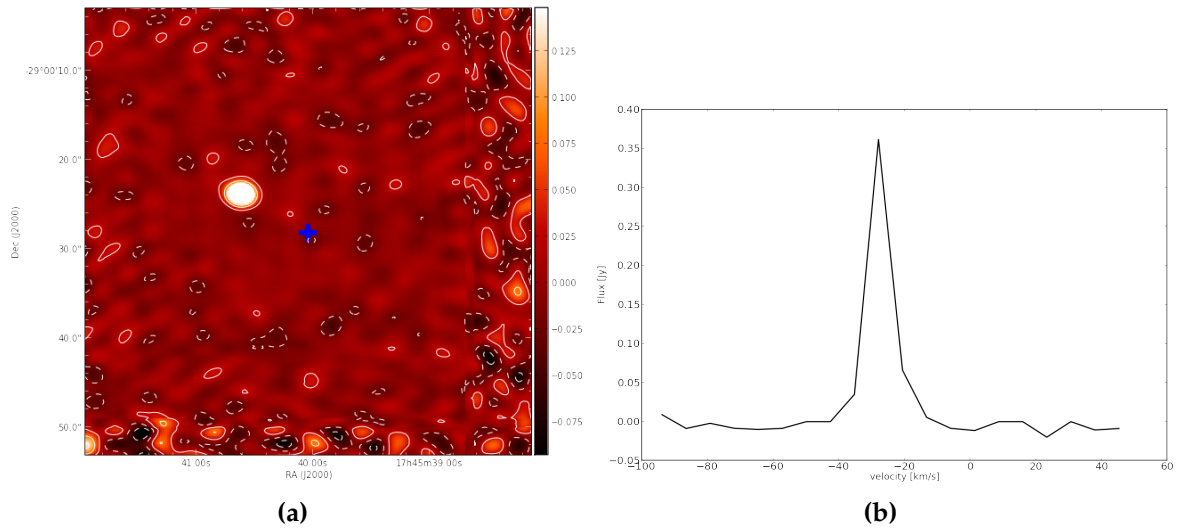


Figure A.5: Image and spectrum of IRS 10EE

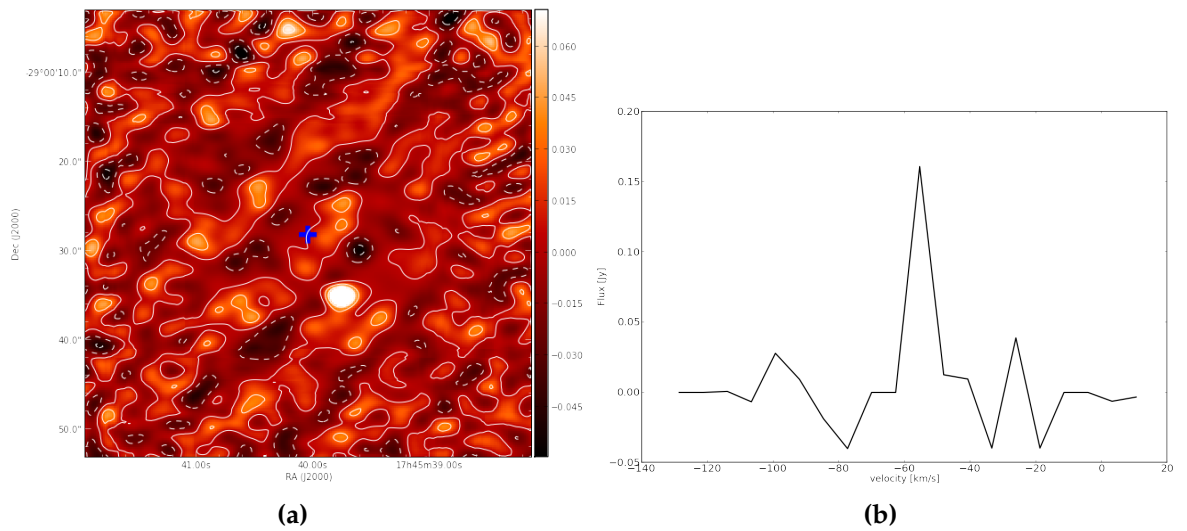


Figure A.6: Image and spectrum of IRS 12N

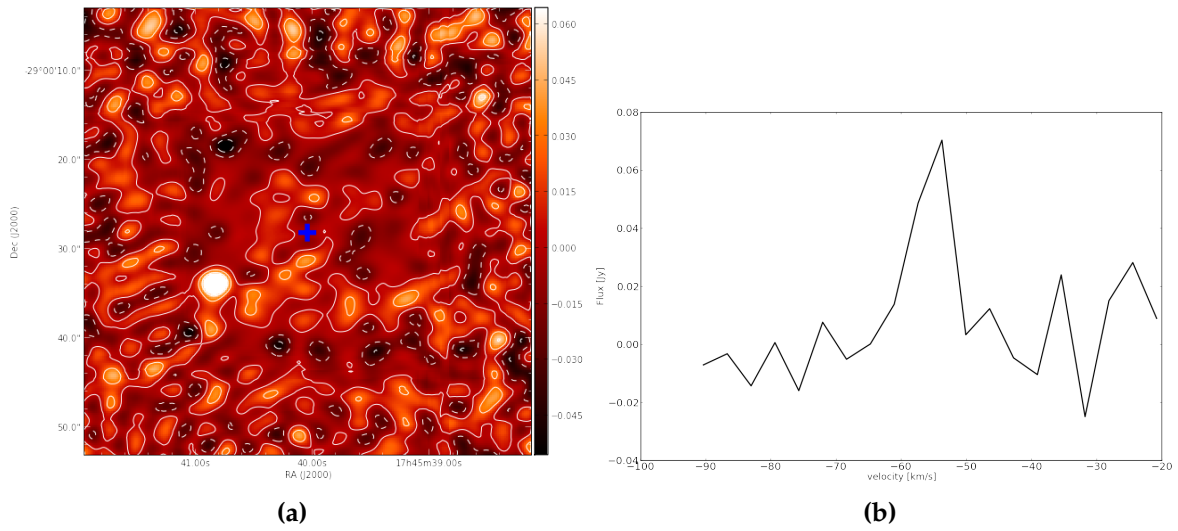


Figure A.7: Image and spectrum of IRS 28

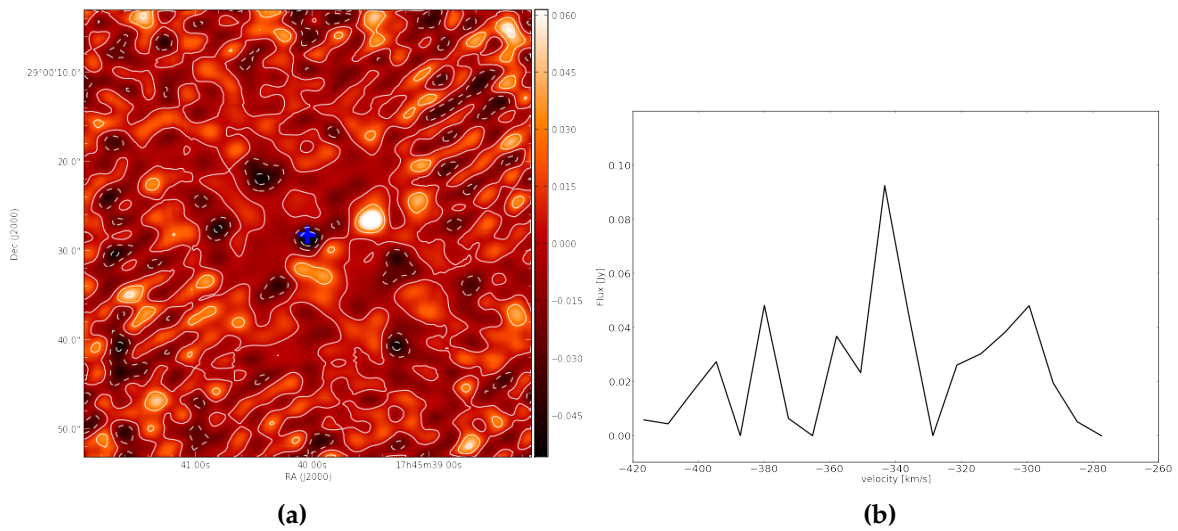


Figure A.8: Image and spectrum of IRS 34

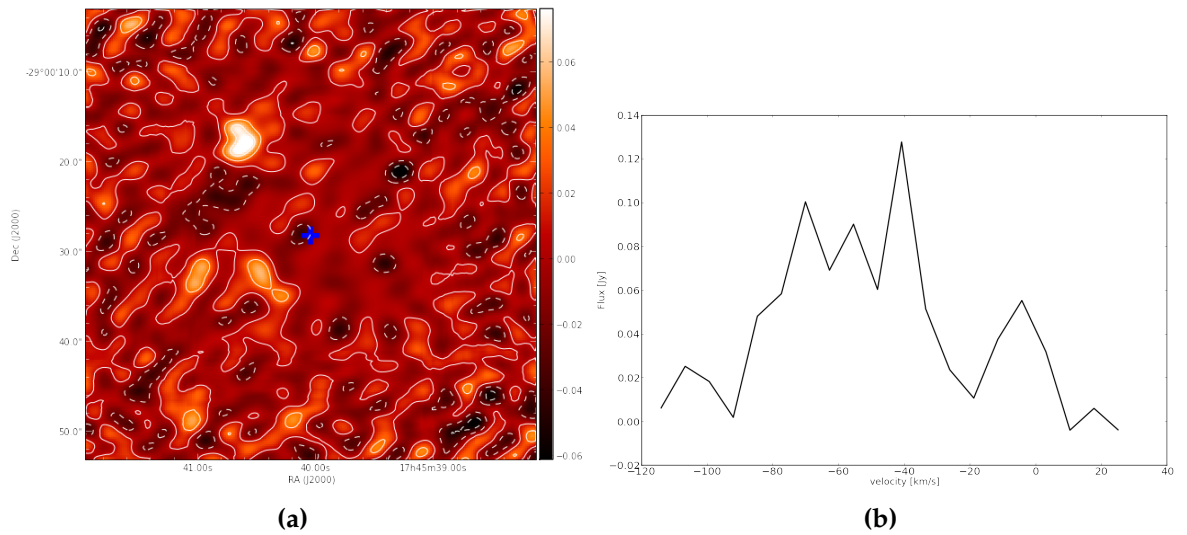


Figure A.9: Image and spectrum of SiO New 1

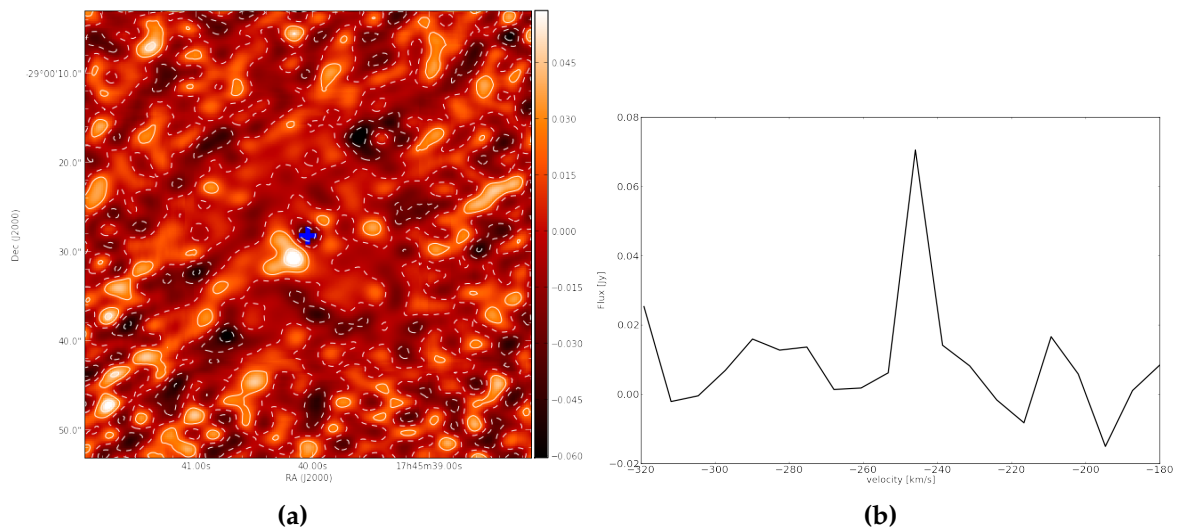


Figure A.10: Image and spectrum of SiO New 2

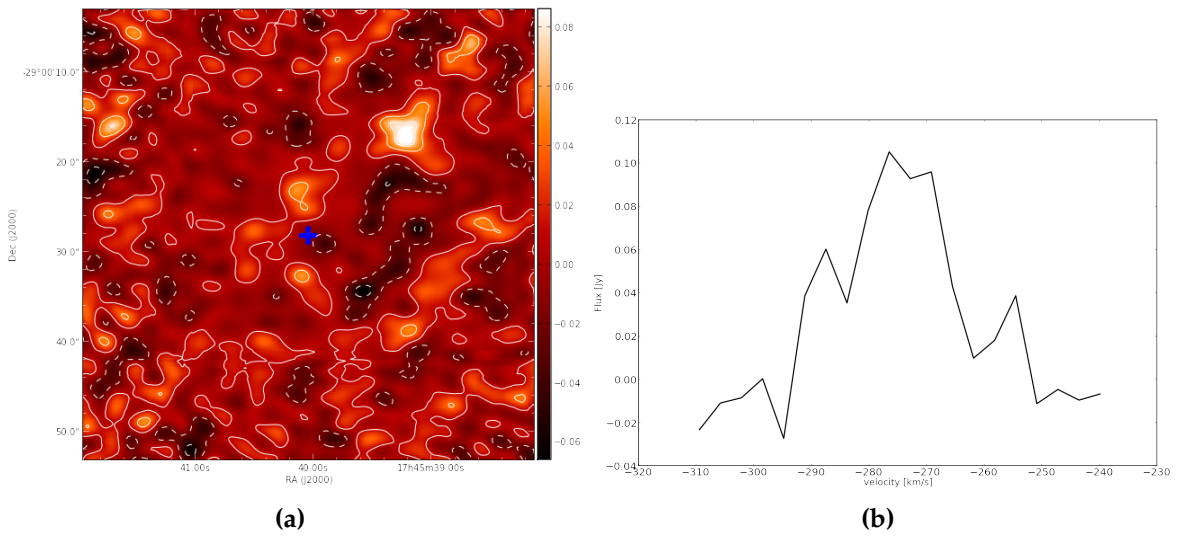


Figure A.11: Image and spectrum of SiO New 3

A.3 POSITION AND FLUX VALUES OF SiO MASERS

Epoch Year	RA "	DEC "	dRA "	dDEC "	Flux Jy
2010.36438356	5.168	0.174	0.0052	0.0051	0.171
2010.36712329	5.13	0.332	0.00822	0.00754	0.155
2010.36986301	4.954	0.106	0.0074	0.0074	0.15
2011.39452055	5.2026	0.086	0.007	0.0094	0.167
2011.39726027	5.164	0.1	0.008	0.012	0.142
2011.40000000	5.078	0.366	0.0074	0.0084	0.156
2012.37260274	5.164	-0.002	0.0118	0.0116	0.16
2012.37534247	5.2388	0.306	0.0096	0.018	0.15
2012.37808219	5.172	0.356	0.0076	0.0152	0.13
2012.38082192	4.958	0.228	0.01058	0.0256	0.144
2014.43287700	5.2756	0.93	0.024	0.066	0.1225
2014.73698600	5.178	0.554	0.0104	0.0102	0.1206
2014.73972600	5.24	0.348	0.0094	0.0078	0.1261

Table A.1: IRS 1W

Epoch Year	RA "	DEC "	dRA "	dDEC "	Flux Jy
2010.36438356	-3.154	-3.574	0.003	0.0028	0.158
2010.36712329	-3.126	-3.618	0.008	0.0072	0.16
2010.36986301	-3.048	-3.748	0.0054	0.0048	0.187
2011.39452055	-2.976	-3.636	0.0094	0.008	0.151
2011.39726027	-3.122	-3.654	0.0078	0.0084	0.175
2011.40000000	-3.188	-3.574	0.005	0.0062	0.134
2012.37260274	-3.23	-3.582	0.0118	0.0206	0.17
2012.37534247	-3.264	-3.544	0.016	0.022	0.16
2012.37808219	-3.262	-3.642	0.0224	0.0402	0.17
2012.38082192	-3.14	-3.67	0.0192	0.0424	0.163
2014.432877	-3.502	-3.206	0.014	0.025	0.148
2014.736986	-3.152	-3.694	0.006	0.008	0.14
2014.739726	-3.254	-3.428	0.012	0.008	0.1417

Table A.2: IRS 2L

Epoch Year	RA "	DEC "	dRA "	dDEC "	Flux Jy
2010.36438356	0.058	5.328	0.00246	0.00176	0.439
2010.36712329	-0.016	5.446	0.0026	0.0018	0.49
2010.36986301	0.034	5.402	0.0014	0.001	0.494
2011.39452055	-0.096	5.32	0.0046	0.0036	0.344
2011.39726027	0.092	5.37	0.0046	0.0038	0.305
2011.40000000	0.086	5.438	0.003	0.0022	0.3
2012.37260274	0.032	5.504	0.0068	0.016	0.497
2012.37534247	0.018	5.394	0.002	0.008	0.527
2012.37808219	0.06	5.508	0.004	0.01	0.475
2012.38082192	0.016	5.472	0.008	0.024	0.465
2013.48493151	-0.144	5.214	0.02	0.05	0.36
2013.66849315	0.024	5.442	0.008	0.008	0.577
2013.70684931	0.046	5.188	0.006	0.004	0.637
2014.25205000	0.164	5.384	0.002	0.002	0.373
2014.43287700	-0.114	5.234	0.032	0.068	0.4
2014.73698600	-0.08	5.398	0.002	0.002	0.59
2014.73972600	0.084	5.402	0.002	0.002	0.62

Table A.3: IRS 7

Epoch Year	RA "	DEC "	dRA "	dDEC "	Flux Jy
2010.36438356	5.6852	-6.3228	0.0025	0.0020	0.209
2010.36712329	5.7602	-6.1762	0.0037	0.0028	0.225
2010.36986301	5.6314	-6.1360	0.0111	0.0074	0.253
2011.39452055	5.8888	-5.9422	0.0198	0.0118	0.21
2011.39726027	5.7668	-6.0506	0.0096	0.0074	0.22
2011.40000000	5.7024	-6.1248	0.0047	0.0036	0.278
2012.37260274	5.6090	-6.2842	0.0085	0.0130	0.127
2012.37534247	5.6382	-6.1046	0.0294	0.0530	0.112
2012.37808219	5.5764	-6.0774	0.0206	0.0354	0.112
2012.38082192	5.6736	-6.2280	0.0058	0.0192	0.139
2014.73698600	5.8190	-6.1934	0.0112	0.0050	0.11
2014.73972600	5.6662	-5.7426	0.0132	0.0120	0.146

Table A.4: IRS 9

Epoch Year	RA "	DEC "	dRA "	dDEC "	Flux Jy
2010.36438356	7.6720	4.078	0.0034	0.0032	0.378
2010.36712329	7.6776	4.228	0.0024	0.0020	0.39
2010.36986301	7.5818	4.192	0.0020	0.0020	0.38
2011.39452055	7.6126	4.118	0.0042	0.0034	0.28
2011.39726027	7.6018	4.142	0.0054	0.0046	0.24
2011.40000000	7.5806	4.178	0.0052	0.0044	0.20
2012.37260274	7.5164	3.898	0.0140	0.0202	0.20
2012.37534247	7.6504	4.254	0.0252	0.0650	0.1
2012.37808219	7.5348	4.422	0.0152	0.0210	0.14
2012.38082192	7.5770	3.938	0.0252	0.0426	0.15
2014.24931500	7.4438	3.864	0.0051	0.0034	0.12

Table A.5: IRS 10EE

Epoch Year	RA "	DEC "	dRA "	dDEC "	Flux Jy
2010.36438356	-3.194	-7.0684	0.0114	0.0084	0.100
2010.36712329	-3.244	-6.8922	0.0076	0.0066	0.143
2010.36986301	-3.656	-7.0164	0.0078	0.0062	0.16
2012.37260274	-3.256	-6.6344	0.0050	0.0082	0.26
2012.37534247	-3.296	-6.8578	0.0038	0.0086	0.22
2012.37808219	-3.128	-6.9894	0.0035	0.0070	0.20
2012.38082192	-3.110	-6.7728	0.0238	0.0436	0.23
2014.43287700	-3.126	-6.4622	0.0274	0.0586	0.17
2014.73698600	-3.250	-6.8634	0.0030	0.0025	0.18
2014.73972600	-3.296	-6.8612	0.0050	0.0032	0.19

Table A.6: IRS 12N

Epoch Year	RA "	DEC "	dRA "	dDEC "	Flux Jy
2010.36438356	9.98780	-5.7386	0.0140	0.008	0.134
2010.36712329	10.3094	-5.7244	0.0100	0.008	0.11
2010.36986301	10.4244	-5.8432	0.0044	0.003	0.153
2012.37260274	10.4798	-5.8726	0.0168	0.022	0.075
2012.37534247	10.3314	-5.4248	0.0260	0.050	0.074
2012.37808219	10.3444	-6.1092	0.0320	0.066	0.074
2012.38082192	10.0470	-5.8776	0.0286	0.050	0.065
2014.43287700	10.2916	-5.8406	0.0124	0.004	0.103
2014.73698600	10.2344	-5.8964	0.1932	0.152	0.100
2014.73972600	10.0848	-5.9746	0.0230	0.016	0.084

Table A.7: IRS 28

Epoch Year	RA "	DEC "	dRA "	dDEC "	Flux Jy
2010.36438356	7.2528	9.8140	0.0076	0.0074	0.100
2010.36712329	7.1894	10.174	0.0122	0.0122	0.115
2010.36986301	6.8064	9.8660	0.0160	0.0260	0.08
2011.39726027	7.0324	9.9300	0.0096	0.0116	0.11
2011.40000000	7.2100	9.6980	0.0114	0.0128	0.096
2012.37260274	6.9314	10.190	0.0114	0.0214	0.103
2012.37534247	7.3500	10.074	0.0080	0.0210	0.09
2012.37808219	7.4240	10.022	0.0140	0.0160	0.085
2012.38082192	7.1374	9.4760	0.0092	0.0240	0.112
2014.43287700	7.1016	9.7740	0.0080	0.0060	0.086

Table A.8: SiO New 1

Epoch Year	RA "	DEC "	dRA "	dDEC "	Flux Jy
2010.36712329	2.226	-2.788	0.0888	0.0121	0.087
2010.36986301	2.290	-3.324	0.0740	0.0088	0.11
2011.39452055	2.090	-2.922	0.0066	0.0056	0.161
2011.39726027	2.158	-2.716	0.0120	0.0094	0.088
2011.40000000	1.982	-2.708	0.0060	0.0148	0.097
2012.37534247	2.026	-2.722	0.0194	0.0390	0.093
2012.37808219	1.898	-1.870	0.1400	0.9040	0.089
2012.38082192	2.068	-3.116	0.0216	0.0498	0.11
2014.73698600	2.004	-3.144	0.0434	0.0688	0.092
2014.73972600	2.024	-2.422	0.0240	0.0260	0.086

Table A.9: SiO New 2

Epoch Year	RA "	DEC "	dRA "	dDEC "	Flux Jy
2010.36438356	-11.312	11.076	0.0152	0.017	0.14
2010.36712329	-11.032	10.616	0.0216	0.020	0.07
2010.36986301	-11.290	10.684	0.0294	0.031	0.06
2011.39452055	-10.698	10.800	0.0360	0.032	0.10
2011.39726027	-11.932	10.732	0.0092	0.009	0.14
2011.40000000	-11.248	11.380	0.0114	0.011	0.11
2012.37260274	-10.422	10.694	0.0340	0.032	0.10
2012.37534247	-11.230	11.150	0.0240	0.022	0.12
2012.37808219	-11.652	11.326	0.0126	0.156	0.14
2012.38082192	-12.028	11.204	0.0228	0.067	0.14
2014.73698600	-12.010	11.728	0.1600	0.360	0.11
2014.73972600	-12.158	11.948	0.1200	0.320	0.09

Table A.10: SiO New 3

BIBLIOGRAPHY

- Anderson, J. M., Ulvestad, J. S., and Ho, L. C. (2004). Low-Luminosity Active Galactic Nuclei at the Highest Resolution: Jets or Accretion Flows? *ApJ*, **603**, 42–50.
- Baganoff, F. K., Bautz, M. W., Brandt, W. N., Chartas, G., Feigelson, E. D., Garmire, G. P., Maeda, Y., Morris, M., Ricker, G. R., Townsley, L. K., and Walter, F. (2001). Rapid X-ray flaring from the direction of the supermassive black hole at the Galactic Centre. *Nature*, **413**, 45–48.
- Balick, B. and Brown, R. L. (1974). Intense sub-arcsecond structure in the galactic center. *ApJ*, **194**, 265–270.
- Ballone, A., Schartmann, M., Burkert, A., Gillessen, S., Genzel, R., Fritz, T. K., Eisenhauer, F., Pfuhl, O., and Ott, T. (2013). Hydrodynamical Simulations of a Compact Source Scenario for the Galactic Center Cloud G2. *ApJ*, **776**, 13.
- Becklin, E. E., Gatley, I., and Werner, M. W. (1982). Far-infrared observations of Sagittarius A - The luminosity and dust density in the central parsec of the Galaxy. *ApJ*, **258**, 135–142.
- Bietenholz, M. F., Bartel, N., and Rupen, M. P. (2000). A Stationary Core with a One-sided Jet in the Center of M81. *ApJ*, **532**, 895–908.
- Borkar, A., Eckart, A., Straubmeier, C., Kunneriath, D., Jalali, B., Sabha, N., Shahzamanian, B., García-Marín, M., Valencia-S, M., Sjouwerman, L., Britzen, S., Karas, V., Dovčiak, M., Donea, A., and Zensus, A. (2016). Monitoring the Galactic Center with ATCA. *MNRAS*.
- Bower, G. C., Wright, M. C. H., Falcke, H., and Backer, D. C. (2003). Interferometric Detection of Linear Polarization from Sagittarius A* at 230 GHz. *ApJ*, **588**, 331–337.

- Broderick, A. E. and Loeb, A. (2006). Imaging optically-thin hotspots near the black hole horizon of Sgr A* at radio and near-infrared wavelengths. *MNRAS*, **367**, 905–916.
- Broderick, A. E. and Loeb, A. (2009). Signatures of Relativistic Helical Motion in the Rotation Measures of Active Galactic Nucleus Jets. *ApJ*, **703**, L104–L108.
- Brown, R. L., Johnston, K. J., and Lo, K. Y. (1981). High resolution VLA observations of the galactic center. *ApJ*, **250**, 155–159.
- Christopher, M. H., Scoville, N. Z., Stolovy, S. R., and Yun, M. S. (2005). HCN and HCO⁺ Observations of the Galactic Circumnuclear Disk. *ApJ*, **622**, 346–365.
- Clénet, Y., Rouan, D., Gendron, E., Montri, J., Rigaut, F., Léna, P., and Lacombe, F. (2001). Adaptive optics L-band observations of the Galactic Center region. *A&A*, **376**, 124–135.
- Crumley, P. and Kumar, P. (2013). Radio emission from the bow shock of G2. *MNRAS*, **436**, 1955–1960.
- Deguchi, S., Fujii, T., Izumiura, H., Kameya, O., Nakada, Y., Nakashima, J.-i., Ootsubo, T., and Ukita, N. (2000a). SiO Maser Survey of the Galactic Disk IRAS Sources. II., the Galactic Center Area. *ApJS*, **128**, 571–595.
- Deguchi, S., Fujii, T., Izumiura, H., Kameya, O., Nakada, Y., and Nakashima, J.-i. (2000b). SiO Maser Survey of the Galactic Disk IRAS Sources. III., a Central Part of the Galaxy. *ApJS*, **130**, 351–379.
- Deguchi, S., Fujii, T., Nakashima, J.-I., and Wood, P. R. (2002). Near-Infrared Observations of the IRAS/SiO Sources in the Galactic Bulge: a Large Scale Distribution. *PASJ*, **54**, 719–734.
- Dexter, J., Kelly, B., Bower, G. C., Marrone, D. P., Stone, J., and Plambeck, R. (2014). An 8 h characteristic time-scale in submillimetre light curves of Sagittarius A*. *MNRAS*, **442**, 2797–2808.
- Dodds-Eden, K., Porquet, D., Trap, G., Quataert, E., Haubois, X., Gillessen, S., Grosso, N., Pantin, E., Falcke, H., Rouan, D., Genzel, R., Hasinger, G., Goldwurm, A., Yusef-Zadeh, F., Clénet, Y., Trippe, S., Lagage, P.-O., Bartko, H., Eisenhauer, F., Ott, T., Paumard, T., Perrin, G., Yuan, F., Fritz, T. K., and Mascetti, L. (2009). Evidence for X-Ray Synchrotron Emission from Simultaneous Mid-Infrared to X-Ray Observations of a Strong Sgr A* Flare. *ApJ*, **698**, 676–692.

- Eckart, A., Moulataka, J., Viehmann, T., Straubmeier, C., Mouawad, N., Genzel, R., Ott, T., and Schödel, R. (2003). New MIR Excess Sources north of the IRS 13 Complex. *Astronomische Nachrichten Supplement*, **324**, 521–526.
- Eckart, A., Baganoff, F. K., Morris, M., Bautz, M. W., Brandt, W. N., Garmire, G. P., Genzel, R., Ott, T., Ricker, G. R., Straubmeier, C., Viehmann, T., Schödel, R., Bower, G. C., and Goldston, J. E. (2004a). First simultaneous NIR/X-ray detection of a flare from Sgr A*. *A&A*, **427**, 1–11.
- Eckart, A., Moulataka, J., Viehmann, T., Straubmeier, C., and Mouawad, N. (2004b). Young Stars at the Center of the Milky Way? *ApJ*, **602**, 760–769.
- Eckart, A., Schödel, R., Meyer, L., Trippe, S., Ott, T., and Genzel, R. (2006a). Polarimetry of near-infrared flares from Sagittarius A*. *A&A*, **455**, 1–10.
- Eckart, A., Baganoff, F. K., Schödel, R., Morris, M., Genzel, R., Bower, G. C., Marrone, D., Moran, J. M., Viehmann, T., Bautz, M. W., Brandt, W. N., Garmire, G. P., Ott, T., Trippe, S., Ricker, G. R., Straubmeier, C., Roberts, D. A., Yusef-Zadeh, F., Zhao, J. H., and Rao, R. (2006b). The flare activity of Sagittarius A*. New coordinated mm to X-ray observations. *A&A*, **450**, 535–555.
- Eckart, A., Schödel, R., García-Marín, M., Witzel, G., Weiss, A., Baganoff, F. K., Morris, M. R., Bertram, T., Dovčiak, M., Duschl, W. J., Karas, V., König, S., Krichbaum, T. P., Krips, M., Kunneriath, D., Lu, R.-S., Markoff, S., Mauerhan, J., Meyer, L., Moulataka, J., Mužić, K., Najarro, F., Pott, J.-U., Schuster, K. F., Sjouwerman, L. O., Straubmeier, C., Thum, C., Vogel, S. N., Wiesemeyer, H., Zamaninasab, M., and Zensus, J. A. (2008). Simultaneous NIR/sub-mm observation of flare emission from Sagittarius A*. *A&A*, **492**, 337–344.
- Eckart, A., García-Marín, M., Vogel, S. N., Teuben, P., Morris, M. R., Baganoff, F., Dexter, J., Schödel, R., Witzel, G., Valencia-S., M., Karas, V., Kunneriath, D., Straubmeier, C., Moser, L., Sabha, N., Buchholz, R., Zamaninasab, M., Mužić, K., Moulataka, J., and Zensus, J. A. (2012). Millimeter to X-ray flares from Sagittarius A*. *A&A*, **537**, A52.
- Eckart, A., Mužić, K., Yazici, S., Sabha, N., Shahzamanian, B., Witzel, G., Moser, L., Garcia-Marin, M., Valencia-S., M., Jalali, B., Bremer, M., Straubmeier, C., Rauch, C., Buchholz, R., Kunneriath, D., and Moulataka, J. (2013). Near-infrared proper motions and spectroscopy of infrared excess sources at the Galactic center. *A&A*, **551**, A18.

- Eckart, A., Valencia-S., M., Shahzamanian, B., Garcia-Marin, M., Peissker, F., Zajack, M., Parsa, M., Jalali, B., Saalfeld, R., Sabha, N., Yazic, S., Karssen, G. D., Borkar, A., Markakis, K., Zensus, J. A., and Straubmeier, C. (2015). The Center of the Milky Way from Radio to X-rays. *ArXiv e-prints*.
- Eckart, M. E., Laird, E. S., Stern, D., Mao, P. H., Helfand, D. J., and Harrison, F. A. (2005). The Serendipitous Extragalactic X-Ray Source Identification (SEXSI) Program. II. Optical Imaging. *ApJS*, **156**, 35–45.
- Einstein, A. (1916). Strahlungs-Emission und Absorption nach der Quantentheorie. *Deutsche Physikalische Gesellschaft*, **18**, 318–323.
- Eisenhauer, F., Genzel, R., Alexander, T., Abuter, R., Paumard, T., Ott, T., Gilbert, A., Gillessen, S., Horrobin, M., Trippe, S., Bonnet, H., Dumas, C., Hubin, N., Kaufer, A., Kissler-Patig, M., Monnet, G., Ströbele, S., Szeifert, T., Eckart, A., Schödel, R., and Zucker, S. (2005). SINFONI in the Galactic Center: Young Stars and Infrared Flares in the Central Light-Month. *ApJ*, **628**, 246–259.
- Ekers, R. D., Goss, W. M., Schwarz, U. J., Downes, D., and Rogstad, D. H. (1975). A full synthesis map of Sgr A at 5 GHz. *A&A*, **43**, 159–166.
- Ekers, R. D., van Gorkom, J. H., Schwarz, U. J., and Goss, W. M. (1983). The radio structure of SGR A. *A&A*, **122**, 143–150.
- Elitzur, M. (1992). Astronomical masers. *ARA&A*, **30**, 75–112.
- Falcke, H., Mannheim, K., and Biermann, P. L. (1993). The Galactic Center radio jet. *A&A*, **278**, L1–L4.
- Geballe, T. R., Rigaut, F., Roy, J.-R., and Draine, B. T. (2004). A Bow Shock of Heated Dust Surrounding Galactic Center Source IRS 8. *ApJ*, **602**, 770–775.
- Genzel, R., Thatte, N., Krabbe, A., Kroker, H., and Tacconi-Garman, L. E. (1996). The Dark Mass Concentration in the Central Parsec of the Milky Way. *ApJ*, **472**, 153.
- Genzel, R., Eckart, A., Ott, T., and Eisenhauer, F. (1997). On the nature of the dark mass in the centre of the Milky Way. *MNRAS*, **291**, 219–234.
- Genzel, R., Schödel, R., Ott, T., Eckart, A., Alexander, T., Lacombe, F., Rouan, D., and Aschenbach, B. (2003). Near-infrared flares from accreting gas around the supermassive black hole at the Galactic Centre. *Nature*, **425**, 934–937.

- Ghez, A. M., Duchêne, G., Matthews, K., Hornstein, S. D., Tanner, A., Larkin, J., Morris, M., Becklin, E. E., Salim, S., Kremenek, T., Thompson, D., Soifer, B. T., Neugebauer, G., and McLean, I. (2003). The First Measurement of Spectral Lines in a Short-Period Star Bound to the Galaxy's Central Black Hole: A Paradox of Youth. *ApJ*, **586**, L127–L131.
- Gillessen, S., Eisenhauer, F., Trippe, S., Alexander, T., Genzel, R., Martins, F., and Ott, T. (2009a). Monitoring Stellar Orbits Around the Massive Black Hole in the Galactic Center. *ApJ*, **692**, 1075–1109.
- Gillessen, S., Eisenhauer, F., Fritz, T. K., Bartko, H., Dodds-Eden, K., Pfuhl, O., Ott, T., and Genzel, R. (2009b). The Orbit of the Star S2 Around SGR A* from Very Large Telescope and Keck Data. *ApJ*, **707**, L114–L117.
- Gillessen, S., Genzel, R., Fritz, T. K., Quataert, E., Alig, C., Burkert, A., Cuadra, J., Eisenhauer, F., Pfuhl, O., Dodds-Eden, K., Gammie, C. F., and Ott, T. (2012). A gas cloud on its way towards the supermassive black hole at the Galactic Centre. *Nature*, **481**, 51–54.
- Gillessen, S., Genzel, R., Fritz, T. K., Eisenhauer, F., Pfuhl, O., Ott, T., Cuadra, J., Schartmann, M., and Burkert, A. (2013). New Observations of the Gas Cloud G2 in the Galactic Center. *ApJ*, **763**, 78.
- Goldston, J. E., Quataert, E., and Igumenshchev, I. V. (2005). Synchrotron Radiation from Radiatively Inefficient Accretion Flow Simulations: Applications to Sagittarius A*. *ApJ*, **621**, 785–792.
- Gordon, J. P., Zeiger, H. J., and Townes, C. H. (1955). The maser—new type of microwave amplifier, frequency standard, and spectrometer. *Phys. Rev.*, **99**, 1264–1274.
- Guesten, R., Genzel, R., Wright, M. C. H., Jaffe, D. T., Stutzki, J., and Harris, A. I. (1987). Aperture synthesis observations of the circumnuclear ring in the Galactic center. *ApJ*, **318**, 124–138.
- Haggard, D., Baganoff, F. K., Rea, N., Zelati, F. C., Ponti, G., Heinke, C., Campana, S., Israel, G. L., Yusef-Zadeh, F., and Roberts, D. (2014). 2014 Chandra X-ray Monitoring of Sgr A*/G2 and SGR J1745-29. *The Astronomer's Telegram*, **6242**, 1.
- Herbst, T. M., Beckwith, S. V. W., Forrest, W. J., and Pipher, J. L. (1993). Infrared imaging spectroscopy of the Galactic center - Distribution and motions of the ionized gas. *AJ*, **105**, 956–970.

- Herrnstein, J. R., Greenhill, L. J., Moran, J. M., Diamond, P. J., Inoue, M., Nakai, N., and Miyoshi, M. (1998). VLBA Continuum Observations of NGC 4258: Constraints on an Advection-dominated Accretion Flow. *ApJ*, **497**, L69–L73.
- Herrnstein, R. M. and Ho, P. T. P. (2002). Hot Molecular Gas in the Galactic Center. *ApJ*, **579**, L83–L86.
- Herrnstein, R. M. and Ho, P. T. P. (2005). The Nature of the Molecular Environment within 5 Parsecs of the Galactic Center. *ApJ*, **620**, 287–307.
- Imai, H., Deguchi, S., Fujii, T., Glass, I. S., Ita, Y., Izumiura, H., Kameya, O., Miyazaki, A., Nakada, Y., and Nakashima, J.-I. (2002). Detections of SiO Masers from the Large-Amplitude Variables in the Galactic Nuclear Disk. *PASJ*, **54**, L19–L22.
- Izumiura, H., Deguchi, S., and Fujii, T. (1998). SiO Maser Forest at the Galactic Center. *ApJ*, **494**, L89–L92.
- Jalali, B., Pelupessy, F. I., Eckart, A., Portegies Zwart, S., Sabha, N., Borkar, A., Moultaqa, J., Mužić, K., and Moser, L. (2014). Star formation in the vicinity of nuclear black holes: young stellar objects close to Sgr A*. *MNRAS*, **444**, 1205–1220.
- Krabbe, A., Genzel, R., Eckart, A., Najarro, F., Lutz, D., Cameron, M., Kroker, H., Tacconi-Garman, L. E., Thatte, N., Weitzel, L., Drapatz, S., Geballe, T., Sternberg, A., and Kudritzki, R. (1995). The Nuclear Cluster of the Milky Way: Star Formation and Velocity Dispersion in the Central 0.5 Parsec. *ApJ*, **447**, L95.
- Kunneriath, D., Witzel, G., Eckart, A., Zamaninasab, M., Gießübel, R., Schödel, R., Baganoff, F. K., Morris, M. R., Dovčiak, M., Duschl, W. J., García-Marín, M., Karas, V., König, S., Krichbaum, T. P., Krips, M., Lu, R.-S., Mauerhan, J., Moultaqa, J., Mužić, K., Sabha, N., Najarro, F., Pott, J.-U., Schuster, K. F., Sjouwerman, L. O., Straubmeier, C., Thum, C., Vogel, S. N., Teuben, P., Weiss, A., Wiesemeyer, H., and Zensus, J. A. (2010). Coordinated NIR/mm observations of flare emission from Sagittarius A*. *A&A*, **517**, A46.
- Lacy, J. H., Achtermann, J. M., and Serabyn, E. (1991). Galactic center gasdynamics - A one-armed spiral in a Keplerian disk. *ApJ*, **380**, L71–L74.
- Levin, Y. and Beloborodov, A. M. (2003). Stellar Disk in the Galactic Center: A Remnant of a Dense Accretion Disk? *ApJ*, **590**, L33–L36.

- Li, J., Shen, Z.-Q., Miyazaki, A., Huang, L., Sault, R. J., Miyoshi, M., Tsuboi, M., and Tsutsumi, T. (2009). The Variability of Sagittarius A* at 3 Millimeter. *ApJ*, **700**, 417–425.
- Li, J., An, T., Shen, Z.-Q., and Miyazaki, A. (2010). ATCA Observations of SiO Masers in the Galactic Center. *ApJ*, **720**, L56–L61.
- Lindqvist, M., Winnberg, A., and Forster, J. R. (1990). Water vapour masers in envelopes of OH/IR stars close to the Galactic centre. *A&A*, **229**, 165–170.
- Lindqvist, M., Ukita, N., Winnberg, A., and Johansson, L. E. B. (1991). SiO maser emission from OH/IR stars close to the Galactic centre. *A&A*, **250**, 431–436.
- Lindqvist, M., Habing, H. J., and Winnberg, A. (1992). OH/IR stars close to the Galactic Centre. II - Their spatial and kinematic properties and the mass distribution within 5-100 PC from the galactic centre. *A&A*, **259**, 118–127.
- Liszt, H. S. (2003). The velocity field of ionized gas near Sgr A*. *A&A*, **408**, 1009–1014.
- Liu, H. and Wu, Q. (2013). Possible Origin of Radio Emission from Nonthermal Electrons in Hot Accretion Flows for Low-luminosity Active Galactic Nuclei. *ApJ*, **764**, 17.
- Liu, S. and Melia, F. (2001). New Constraints on the Nature of Radio Emission in Sagittarius A*. *ApJ*, **561**, L77–L80.
- Liu, S., Melia, F., and Petrosian, V. (2006). Stochastic Electron Acceleration During the Near-Infrared and X-Ray Flares in Sagittarius A*. *ApJ*, **636**, 798–803.
- Lo, K. Y. and Claussen, M. J. (1983). High-resolution observations of ionized gas in central 3 parsecs of the Galaxy - Possible evidence for infall. *Nature*, **306**, 647–651.
- Lo, K. Y., Schilizzi, R. T., Cohen, M. H., and Ross, H. N. (1975). VLBI observations of the compact radio source in the center of the Galaxy. *ApJ*, **202**, L63–L65.
- Lynden-Bell, D. and Rees, M. J. (1971). On quasars, dust and the galactic centre. *MNRAS*, **152**, 461.
- Markoff, S. and Falcke, H. (2003). Jet Models for Flaring in Sgr A*. *Astronomische Nachrichten Supplement*, **324**, 445–451.

- Markoff, S., Falcke, H., Yuan, F., and Biermann, P. L. (2001). The Nature of the 10 kilosecond X-ray flare in Sgr A*. *A&A*, **379**, L13–L16.
- Marrone, D. P., Moran, J. M., Zhao, J.-H., and Rao, R. (2006). Interferometric Measurements of Variable 340 GHz Linear Polarization in Sagittarius A*. *ApJ*, **640**, 308–318.
- Marrone, D. P., Baganoff, F. K., Morris, M. R., Moran, J. M., Ghez, A. M., Hornstein, S. D., Dowell, C. D., Muñoz, D. J., Bautz, M. W., Ricker, G. R., Brandt, W. N., Garmire, G. P., Lu, J. R., Matthews, K., Zhao, J.-H., Rao, R., and Bower, G. C. (2008). An X-Ray, Infrared, and Submillimeter Flare of Sagittarius A*. *ApJ*, **682**, 373–383.
- Marscher, A. P. (1983). Accurate formula for the self-Compton X-ray flux density from a uniform, spherical, compact radio source. *ApJ*, **264**, 296.
- Mauerhan, J. C., Morris, M., Walter, F., and Baganoff, F. K. (2005). Intraday Variability of Sagittarius A* at 3 Millimeters. *ApJ*, **623**, L25–L28.
- Melia, F. and Falcke, H. (2001). The Supermassive Black Hole at the Galactic Center. *ARA&A*, **39**, 309–352.
- Menten, K. M., Reid, M. J., Eckart, A., and Genzel, R. (1997). The Position of Sagittarius A*: Accurate Alignment of the Radio and Infrared Reference Frames at the Galactic Center. *ApJ*, **475**, L111–L114.
- Messineo, M., Habing, H. J., Sjouwerman, L. O., Omont, A., and Menten, K. M. (2002). 86 GHz SiO maser survey of late-type stars in the Inner Galaxy. I. Observational data. *A&A*, **393**, 115–128.
- Miyazaki, A., Deguchi, S., Tsuboi, M., Kasuga, T., and Takano, S. (2001). SiO Maser Survey in the Galactic Center Region with a Multi-Beam Receiver. *PASJ*, **53**, 501–507.
- Mohan, P. and Mangalam, A. (2015). Kinematics of and emission from helically orbiting blobs in a relativistic magnetized jet. *ArXiv e-prints*.
- Montero-Castaño, M., Herrnstein, R. M., and Ho, P. T. P. (2009). Gas Infall Toward Sgr A* from the Clumpy Circumnuclear Disk. *ApJ*, **695**, 1477–1494.

- Morris, M., Howard, C., Muno, M., Baganoff, F. K., Park, S., Feigelson, E., Garmire, G., and Brandt, N. (2004). The Hot Interstellar Medium of the Galactic Center: Observations with Chandra. In S. Pfalzner, C. Kramer, C. Staubmeier, and A. Heithausen, editors, *The Dense Interstellar Medium in Galaxies*, page 281.
- Moultaka, J., Boisson, C., Joly, M., and Pelat, D. (2004a). Constraining the solutions of an inverse method of stellar population synthesis. *A&A*, **420**, 459–466.
- Moultaka, J., Eckart, A., Viehmann, T., Mouawad, N., Straubmeier, C., Ott, T., and Schödel, R. (2004b). Dust embedded sources at the Galactic Center. 2 to 4 μm imaging and spectroscopy in the central parsec. *A&A*, **425**, 529–542.
- Moultaka, J., Eckart, A., Schödel, R., Viehmann, T., and Najarro, F. (2005). VLT L-band mapping of the Galactic center IRS 3-IRS 13 region. Evidence for new Wolf-Rayet type stars. *A&A*, **443**, 163–173.
- Murray-Clay, R. A. and Loeb, A. (2012). Disruption of a proto-planetary disc by the black hole at the milky way centre. *Nature Communications*, **3**, 1049.
- Mužić, K., Schödel, R., Eckart, A., Meyer, L., and Zensus, A. (2008). IRS 13N: a new comoving group of sources at the Galactic center. *A&A*, **482**, 173–178.
- Narayan, R., Mahadevan, R., Grindlay, J. E., Popham, R. G., and Gammie, C. (1998). Advection-dominated accretion model of Sagittarius A*: evidence for a black hole at the Galactic center. *ApJ*, **492**, 554–568.
- Narayan, R., Özel, F., and Sironi, L. (2012). Radio Synchrotron Emission from a Bow Shock around the Gas Cloud G2 Heading toward the Galactic Center. *ApJ*, **757**, L20.
- Nemmen, R. S., Storchi-Bergmann, T., and Eracleous, M. (2014). Spectral models for low-luminosity active galactic nuclei in LINERs: the role of advection-dominated accretion and jets. *MNRAS*, **438**, 2804–2827.
- Ott, T., Eckart, A., and Genzel, R. (1999). Variable and Embedded Stars in the Galactic Center. *ApJ*, **523**, 248–264.
- Oyama, T., Miyoshi, M., Deguchi, S., Imai, H., and Shen, Z.-Q. (2008). A Measurement of Proper Motions of SiO Maser Sources in the Galactic Center with the VLBA. *PASJ*, **60**, 11–.

- Paumard, T., Maillard, J.-P., and Morris, M. (2004). Kinematic and structural analysis of the <ASTROBJ>Minispiral</ASTROBJ> in the Galactic Center from BEAR spectro-imagery. *A&A*, **426**, 81–96.
- Paumard, T., Genzel, R., Martins, F., Nayakshin, S., Beloborodov, A. M., Levin, Y., Trippe, S., Eisenhauer, F., Ott, T., Gillessen, S., Abuter, R., Cuadra, J., Alexander, T., and Sternberg, A. (2006). The Two Young Star Disks in the Central Parsec of the Galaxy: Properties, Dynamics, and Formation. *ApJ*, **643**, 1011–1035.
- Peebles, M. S., Stanek, K. Z., and Depoy, D. L. (2007). A Study of Stellar Photometric Variability Within the Central 4pc of the Galactic Center with Infrared Image Subtraction. *ACTA Astronomica*, **57**, 173–199.
- Pfuhl, O., Gillessen, S., Eisenhauer, F., Genzel, R., Plewa, P. M., Ott, T., Ballone, A., Schartmann, M., Burkert, A., Fritz, T. K., Sari, R., Steinberg, E., and Madigan, A.-M. (2015). The Galactic Center Cloud G2 and its Gas Streamer. *ApJ*, **798**, 111.
- Phifer, K., Do, T., Meyer, L., Ghez, A. M., Witzel, G., Yelda, S., Boehle, A., Lu, J. R., Morris, M. R., Becklin, E. E., and Matthews, K. (2013). Keck Observations of the Galactic Center Source G2: Gas Cloud or Star? *ApJ*, **773**, L13.
- Reid, M. J. and Brunthaler, A. (2004). The Proper Motion of Sagittarius A*. II. The Mass of Sagittarius A*. *ApJ*, **616**, 872–884.
- Reid, M. J., Readhead, A. C. S., Vermeulen, R. C., and Treuhaft, R. N. (1999). The Proper Motion of Sagittarius A*. I. First VLBA Results. *ApJ*, **524**, 816–823.
- Reid, M. J., Menten, K. M., Genzel, R., Ott, T., Schödel, R., and Eckart, A. (2003). The Position of Sagittarius A*. II. Accurate Positions and Proper Motions of Stellar SiO Masers near the Galactic Center. *ApJ*, **587**, 208–220.
- Reid, M. J., Menten, K. M., Trippe, S., Ott, T., and Genzel, R. (2007). The Position of Sagittarius A*. III. Motion of the Stellar Cusp. *ApJ*, **659**, 378–388.
- Rigaut, F., Geballe, T. R., Roy, J.-R., and Draine, B. T. (2003). A Bow Shock of Heated Dust Surrounding IRS 8. *Astronomische Nachrichten Supplement*, **324**, 551–555.
- Roberts, D. A. and Goss, W. M. (1993). Multiconfiguration VLA H92-alpha observations of Sagittarius A West at 1 arcsecond resolution. *ApJS*, **86**, 133–152.

- Sabha, N., Witzel, G., Eckart, A., Buchholz, R. M., Bremer, M., Gießübel, R., García-Marín, M., Kunneriath, D., Muzic, K., Schödel, R., Straubmeier, C., Zamaninasab, M., and Zernickel, A. (2010). The extreme luminosity states of Sagittarius A*. *A&A*, **512**, A2.
- Sault, R. J., Teuben, P. J., and Wright, M. C. H. (1995). A Retrospective View of MIRIAD. In R. A. Shaw, H. E. Payne, and J. J. E. Hayes, editors, *Astronomical Data Analysis Software and Systems IV*, volume 77 of *Astronomical Society of the Pacific Conference Series*, page 433.
- Sądowski, A., Sironi, L., Abarca, D., Guo, X., Özel, F., and Narayan, R. (2013). Radio light curves during the passage of cloud G2 near Sgr A*. *MNRAS*, **432**, 478–491.
- Schödel, R., Ott, T., Genzel, R., Hofmann, R., Lehnert, M., Eckart, A., Mouawad, N., Alexander, T., Reid, M. J., Lenzen, R., Hartung, M., Lacombe, F., Rouan, D., Gendron, E., Rousset, G., Lagrange, A.-M., Brandner, W., Ageorges, N., Lidman, C., Moorwood, A. F. M., Spyromilio, J., Hubin, N., and Menten, K. M. (2002). A star in a 15.2-year orbit around the supermassive black hole at the centre of the Milky Way. *Nature*, **419**, 694–696.
- Schwarz, U. J., Bregman, J. D., and van Gorkom, J. H. (1989). The distribution and kinematics of the ionized gas in the Galactic centre region. *A&A*, **215**, 33–47.
- Scoville, N. and Burkert, A. (2013). The Galactic Center Cloud G2 — a Young Low-mass Star with a Stellar Wind. *ApJ*, **768**, 108.
- Serabyn, E. and Lacy, J. H. (1985). Forbidden NE II observations of the galactic center - Evidence for a massive block hole. *ApJ*, **293**, 445–458.
- Serabyn, E., Lacy, J. H., Townes, C. H., and Bharat, R. (1988). High-resolution forbidden NE II observations of the ionized filaments in the Galactic center. *ApJ*, **326**, 171–185.
- Shahzamanian, B., Eckart, A., Valencia-S., M., Witzel, G., Zamaninasab, M., Sabha, N., García-Marín, M., Karas, V., Karssen, G. D., Borkar, A., Dovčiak, M., Kunneriath, D., Bursa, M., Buchholz, R., Moutaka, J., and Straubmeier, C. (2015). Polarized light from Sagittarius A* in the near-infrared K_s-band. *A&A*, **576**, A20.
- Sjouwerman, L. O. and Chandler, C. J. (2014). Monitoring observations of the interaction between Sgr A* and G2 with the Karl G. Jansky Very Large Array. In L. O.

- Sjouwerman, C. C. Lang, and J. Ott, editors, *IAU Symposium*, volume 303 of *IAU Symposium*, pages 327–329.
- Sjouwerman, L. O., Lindqvist, M., van Langevelde, H. J., and Diamond, P. J. (2002). H₂O and SiO maser emission in Galactic center OH/IR stars \$O and SiO maser emission in Galactic center OH/IR stars. *A&A*, **391**, 967–978.
- Sjouwerman, L. O., Messineo, M., and Habing, H. J. (2004). 43 GHz SiO Masers and Astrometry with VERA in the Galactic Center. *PASJ*, **56**, 45–50.
- Su, M., Slatyer, T. R., and Finkbeiner, D. P. (2010). Giant Gamma-ray Bubbles from Fermi-LAT: Active Galactic Nucleus Activity or Bipolar Galactic Wind? *ApJ*, **724**, 1044–1082.
- Tamura, M., Werner, M. W., Becklin, E. E., and Phinney, E. S. (1996). Detection of Stellar Variability in the Central Parsec of the Galaxy. *ApJ*, **467**, 645.
- Tanner, A., Ghez, A. M., Morris, M., Becklin, E. E., Cotera, A., Ressler, M., Werner, M., and Wizinowich, P. (2002). Spatially Resolved Observations of the Galactic Center Source IRS 21. *ApJ*, **575**, 860–870.
- Tanner, A., Ghez, A. M., Morris, M. R., and Christou, J. C. (2005). Stellar Bow Shocks in the Northern Arm of the Galactic Center: More Members and Kinematics of the Massive Star Population. *ApJ*, **624**, 742–750.
- Tanner, A., Figer, D. F., Najarro, F., Kudritzki, R. P., Gilmore, D., Morris, M., Becklin, E. E., McLean, I. S., Gilbert, A. M., Graham, J. R., Larkin, J. E., Levenson, N. A., and Teplitz, H. I. (2006). High Spectral Resolution Observations of the Massive Stars in the Galactic Center. *ApJ*, **641**, 891–904.
- Tanner, A. M., Ghez, A. M., Morris, M., and Becklin, E. E. (2003). Resolving The Northern Arm Sources at the Galactic Center. *Astronomische Nachrichten Supplement*, **324**, 597–603.
- Valencia-S., M., Eckart, A., Zajaček, M., Peissker, F., Parsa, M., Grosso, N., Mossoux, E., Porquet, D., Jalali, B., Karas, V., Yazici, S., Shahzamanian, B., Sabha, N., Saalfeld, R., Smajic, S., Grellmann, R., Moser, L., Horrobin, M., Borkar, A., García-Marín, M., Dovčiak, M., Kunneriath, D., Karssen, G. D., Bursa, M., Straubmeier, C., and Bushouse, H. (2015). Monitoring the Dusty S-cluster Object (DSO/G2) on its Orbit toward the Galactic Center Black Hole. *ApJ*, **800**, 125.

- van der Laan, H. (1966). A Model for Variable Extragalactic Radio Sources. *Nature*, **211**, 1131.
- Viehmann, T., Eckart, A., Schödel, R., Moutaka, J., Straubmeier, C., and Pott, J.-U. (2005). L- and M-band imaging observations of the Galactic Center region. *A&A*, **433**, 117–125.
- Weaver, H., Williams, D. R. W., Dieter, N. H., and Lum, W. T. (1965). Observations of a Strong Unidentified Microwave Line and of Emission from the OH Molecule. *Nature*, **208**, 29–31.
- Witzel, G., Eckart, A., Bremer, M., Zamaninasab, M., Shahzamanian, B., Valencia-S., M., Schödel, R., Karas, V., Lenzen, R., Marchili, N., Sabha, N., Garcia-Marin, M., Buchholz, R. M., Kunneriath, D., and Straubmeier, C. (2012). Source-intrinsic Near-infrared Properties of Sgr A*: Total Intensity Measurements. *ApJS*, **203**, 18.
- Witzel, G., Ghez, A. M., Morris, M. R., Sitarski, B. N., Boehle, A., Naoz, S., Campbell, R., Becklin, E. E., Canalizo, G., Chappell, S., Do, T., Lu, J. R., Matthews, K., Meyer, L., Stockton, A., Wizinowich, P., and Yelda, S. (2014). Detection of Galactic Center Source G2 at 3.8 μm during Periapse Passage. *ApJ*, **796**, L8.
- Wood, P. R., Habing, H. J., and McGregor, P. J. (1998). Infrared monitoring of OH/IR stars near the Galactic Center. *A&A*, **336**, 925–941.
- Wright, M. C. H., Coil, A. L., McGary, R. S., Ho, P. T. P., and Harris, A. I. (2001). Molecular Tracers of the Central 12 Parsecs of the Galactic Center. *ApJ*, **551**, 254–268.
- Yuan, F., Markoff, S., and Falcke, H. (2002). A Jet-ADAF model for Sgr A*. *A&A*, **383**, 854–863.
- Yuan, F., Markoff, S., and Falcke, H. (2003a). A Jet-ADAF Model for Sgr A*. *Astronomische Nachrichten Supplement*, **324**, 453–458.
- Yuan, F., Quataert, E., and Narayan, R. (2003b). Nonthermal Electrons in Radiatively Inefficient Accretion Flow Models of Sagittarius A*. *ApJ*, **598**, 301–312.
- Yusef-Zadeh, F., Bushouse, H., Dowell, C. D., Wardle, M., Roberts, D., Heinke, C., Bower, G. C., Vila-Vilaró, B., Shapiro, S., Goldwurm, A., and Bélanger, G. (2006a). A Multiwavelength Study of Sgr A*: The Role of Near-IR Flares in Production of X-Ray, Soft γ -Ray, and Submillimeter Emission. *ApJ*, **644**, 198–213.

- Yusef-Zadeh, F., Roberts, D., Wardle, M., Heinke, C. O., and Bower, G. C. (2006b). Flaring Activity of Sagittarius A* at 43 and 22 GHz: Evidence for Expanding Hot Plasma. *ApJ*, **650**, 189–194.
- Yusef-Zadeh, F., Wardle, M., Heinke, C., Dowell, C. D., Roberts, D., Baganoff, F. K., and Cotton, W. (2008). Simultaneous Chandra, CSO, and VLA Observations of Sgr A*: The Nature of Flaring Activity. *ApJ*, **682**, 361–372.
- Yusef-Zadeh, F., Bushouse, H., Schödel, R., Wardle, M., Cotton, W., Roberts, D. A., Nogueras-Lara, F., and Gallego-Cano, E. (2015a). Compact Radio Sources within 30' of Sgr A*: Proper Motions, Stellar Winds, and the Accretion Rate onto Sgr A*. *ApJ*, **809**, 10.
- Yusef-Zadeh, F., Wardle, M., Sewilo, M., Roberts, D. A., Smith, I., Arendt, R., Cotton, W., Lacy, J., Martin, S., Pound, M. W., Rickert, M., and Royster, M. (2015b). Signatures of Young Star Formation Activity within Two Parsecs of Sgr A*. *ApJ*, **808**, 97.
- Zamaninasab, M., Eckart, A., Witzel, G., Dovciak, M., Karas, V., Schödel, R., Gießübel, R., Bremer, M., García-Marín, M., Kunneriath, D., Mužić, K., Nishiyama, S., Sabha, N., Straubmeier, C., and Zensus, A. (2010). Near infrared flares of Sagittarius A*. Importance of near infrared polarimetry. *A&A*, **510**, A3.
- Zhao, J.-H., Morris, M. R., Goss, W. M., and An, T. (2009). Dynamics of Ionized Gas at the Galactic Center: Very Large Array Observations of the Three-dimensional Velocity Field and Location of the Ionized Streams in Sagittarius A West. *ApJ*, **699**, 186–214.
- Zylka, R., Mezger, P. G., Ward-Thompson, D., Duschl, W. J., and Lesch, H. (1995). Anatomy of the Sagittarius A complex. 4: SGR A* and the Central Cavity revisited. *A&A*, **297**, 83–97.

LIST OF FIGURES

1.1	The Milky Way across the night sky as seen at the ATCA site. Image credit: Alex Cherney (terraastro.com).	2
1.2	A sketch of our Galaxy showing different structural components, the disk, the bulge, and the halo. Image: Ka Chun Yu, Introduction to Astronomy.	3
1.3	A combined image of the Galactic Center as seen from the Hubble Space Telescope in near-infrared, Spitzer Space Telescope in infrared, and Chandra X-ray Observatory in X-ray light. (Image credit: NASA/ESA/Spitzer/CXC/STScI).	4
1.4	Integrated 8.3 GHz image of the mini-spiral with marked components, the Western arc, the Northern and Eastern arms, and the extended bar. (Image: Zhao <i>et al.</i> (2009)).	6
1.5	Schematic diagram of the Sgr A Complex as seen in the plane of the sky. (Image: Herrnstein and Ho (2005)).	7
1.6	A composite NIR image ($\lambda = 1.5 - 4\mu m$) of the GC environment within the central parsec with the most prominent sources. The image is taken with NACO instrument at European Southern Observatory's Very Large Telescope. Image: GC webpage of I. Physikalisches Institut, University of Cologne.	8
1.7	Inferred orbits of S-cluster objects around the supermassive black hole Sgr A* obtained from the data from Eisenhauer <i>et al.</i> (2005).	9
1.8	The figure shows apparent motion of Sgr A* on the plane of the sky. Position residuals of Sgr A* relative to extragalactic source J1745 - 283 is plotted along with $1 - \sigma$ error bars. The dashed line represents the variance-weighted best-fit proper motion, and the solid line gives the orientation of the Galactic plane. Image: Reid and Brunthaler (2004). . .	12
1.9	Spectrum of Sgr A*. Image: Yuan <i>et al.</i> (2003b).	13

2.1	Electromagnetic transmittance of the atmosphere of the Earth over different parts of the electromagnetic spectrum. Image: NASA/jpl.nasa.gov	19
2.2	Blackbody radiation curves at different temperatures. Image: astronomy.swin.edu.au.	20
2.3	Log-log plot of the blackbody curves for different temperatures. The straight line slope of the curve below THz (10^{12} Hz) frequency shows that the Rayleigh-Jeans approximation for the Planck law is valid for the radio frequencies. Image: web.njit.edu.	21
2.4	The spectrum of a homogeneous cylindrical synchrotron source for optically thick and thin region, with the turnover frequency ν_1 . Image: ifa.hawaii.edu	23
2.5	The illustration of the Gamma-ray bubbles arising from the GC. Image: Fermi telescope website.	24
2.6	A simple sketch showing different components of a single dish radio telescope. Image: http://www.haystack.edu/	25
2.7	A block diagram showing a simple two element interferometer. Image: gmrt.ncra.tifr.res.in	27
2.8	As an example of the $u-v$ coverage of telescope array – the $u-v$ coverage of Sgr A* with ATCA	29
2.9	The Australia Telescope Compact Array during observations in 2013. . .	31
3.1	The schematic diagram of jet-disk coupling model for Sgr A*. Image: Yuan <i>et al.</i> (2003a).	41
3.2	The differential light curves of Sgr A* with ATCA at 3mm for the days during which flares were detected. The top panel in each subfigure shows the differential flux density of Sgr A*, while the bottom panel shows the observed calibrator flux on that day. The data points between the vertical lines show the detected individual flares. A differential light curve from 02 April 2014 observation is shown as an example of smooth flux variation with no strong flare activity. No flares were observed during that day with their start and stop times within the observed time range and with peak amplitude in excess of 0.3 Jy.	45
3.3	The fitted models for the detected flares. The black curve denotes observed differential flux points. The individual flares are shown by red curve. In case of multiple sub-flares, the individual flares are shown by red curve and the blue dotted curve shows the combined fitted model. See also Borkar <i>et al.</i> (2016) for details.	51

3.4	The DSO/G2 observed at different times along its trajectory towards Sgr A*, showing the detection of redshifted and blueshifted parts, as it underwent periape in May 2014. Image: ESO/ Valencia-S. et al. (2015)	54
4.1	Positions of all the detected SiO masers. The size of the circle is proportional to the flux density of the corresponding SiO maser. The blue '+' marks the position of Sgr A*	60
4.2	The RA and DEC proper motion of IRS 1W, IRS 2L, IRS 7 and IRS 9.	65
4.3	The RA and DEC proper motion of IRS 10EE, IRS 12N, IRS 28 and SiO New 1.	66
4.4	The RA and DEC proper motion of SiO New 2, and SiO New 3.	67
A.1	Image and spectrum of IRS 1W	77
A.2	Image and spectrum of IRS 2L	77
A.3	Image and spectrum of IRS 7	78
A.4	Image and spectrum of IRS 9	78
A.5	Image and spectrum of IRS 10EE	79
A.6	Image and spectrum of IRS 12N	79
A.7	Image and spectrum of IRS 28	80
A.8	Image and spectrum of IRS 34	80
A.9	Image and spectrum of SiO New 1	81
A.10	Image and spectrum of SiO New 2	81
A.11	Image and spectrum of SiO New 3	82

LIST OF TABLES

2.1	The Log of observations of Sgr A* taken during 2010 to 2014. The dashes represent the days on which observations were not made. See section 3.4 for details.	32
3.1	The values of dimensionless parameters $d(\alpha)$ and $b(\alpha)$ for various values of α . Source: Marscher (1983)	38
3.2	The lower quartile flux density values of the Sgr A* for the observations.	43
3.3	The parameters for the individual source components estimated from the adiabatically expanding plasmon model. See also Borkar <i>et al.</i> (2016) for details.	49
4.1	SiO maser proper motions for strong sources	61
A.1	IRS 1W	83
A.2	IRS 2L	84
A.3	IRS 7	85
A.4	IRS 9	86
A.5	IRS 10EE	86
A.6	IRS 12N	87
A.7	IRS 28	87
A.8	SiO New 1	88
A.9	SiO New 2	88
A.10	SiO New 3	89

LIST OF ACRONYMS

ADAF	Advection dominated accretion flow
AGB	Asymptotic giant branch
AGN	Active galactic nuclei
ALMA	Atacama Large Millimeter Array
ATCA	Australia Telescope Compact Array
ATNF	Australia Telescope Natinal Facility
AU	Astronomical Unit
CABB	Compact Array Broadband Backend
cm	centimeter
CND	Circumnuclear disk
CSIRO	Commonwealth Scientific and Industrial Research Organisation
CXC	Chandra X-ray Observatory
DSO	Dusty S-cluster Object
ESA	European Space Agency
GC	Galactic Center
GMCs	Giant molecular clouds
HF	High frequency
IF	Intermediate frequency
IR	Infrared
IRS	Infrared source
JD	Julian Date
kpc	kilo parsecs
LBV	Luminous blue variable
LLAGN	Low luminosity active galactic nuclei
mm	millimeter
μ s	microarcsecond

mas	milliarcsecond
MIR	Mid-infrared
NACO	Nasmyth Adaptive Optics System (NAOS) Near-Infrared Imager and Spectrograph (CON
NASA	National Aeronautics and Space Administration
NIR	Near infrared
NRAO	National Radio Astronomy Observatory
pc	parsecs
RIAF	Radiatively inefficient accretion flow
SED	Spectral Energy Distribution
Sgr A*	Sagittarius A*
SINFONI	Spectrograph for INtegral Field Observations in the Near Infrared
SiO	Silicon Oxide
SKA	Square Kilometer Array
SMA	Submillimeter Array
SMBH	Supermassive black hole
SSC	Synchrotron self-Compton
STScI	Space Telescope Science Institute
submm	sub-millimeter
UHF	Ultra high frequency
UT	Universal Time
VHF	Very high frequency
VLA	Very Large Array
VLBA	Very Long Baseline Array
VLBI	Very Large Baseline Interferometry
YSO	Young Stellar Objects

ACKNOWLEDGEMENTS

I would like to conclude the thesis by expressing my gratitude to all the people who have made the thesis possible, and my life in last few years enjoyable.

Firstly, I would like to thank my supervisor, Prof. Dr. Andreas Eckart for his support and guidance. He was always patient and ready to discuss. I am very grateful to have him as advisor.

I want to thank Prof. Dr. Anton Zensus for his support throughout my PhD. I would like to thank the International Max Planck Research School (IMPRS), the Max Planck Institut für Radioastronomie (MPIfR) and Prof. Zensus for the financial support for my PhD. I also want to express my gratitude to Dr. Emmanouil Angelakis, the former IMPRS coordinator, for his help and assistance, and many discussions on IMPRS matters, and Dr. Simone Pott, the secretary of IMPRS, for assisting in any problems I faced during my 3 years. Thanks also to all the members of my thesis committee, Prof. Eckart, Prof. Zensus, Prof. Prof. Yaping Shao, Dr. Macarena Garcia-Marin, and Dr. Behrang Jalali.

Many thanks also to my professors during my M.Sc., Prof. Dr. Jayaram Chennu, Prof. Dr. Rajeev Pathak, and Prof. Dr. Kiran Adhi, for encouraging and motivating me to explore, without whom, I would not be here.

I also want to thank *COST* (European Cooperation in Science and Technology) for funding my observations trip to Australia. And many thanks also to Dr. Alina Donea of Monash University, Melbourne, for hosting me.

Special thanks to all the current and former people belonging to the `aegroup` and `hires` group for all the fun, the international political conferences during lunch, the regular and spontaneous outings, all the amazing cakes, sweets and

snacks from all over the world, the discussions during the group meetings, for the technical, scientific and moral support. Thanks also to the secretaries at the institute for their assistance, and making the bureaucratic matters simpler.

My Indian friends in Cologne, Prasanna, Ketki, Jayesh, Sharwari, Rahul, Shradha, Vedhas, Rohini, Sandip, Nandita, and Megha, thank you for being such amazing people, for creating a homely atmosphere in the foreign land, especially cooking amazing food, and celebrating festivals together! My non-Indian friends in Cologne-Bonn, Mohammad, Nadeen, Eric, Behrang, Ati, Banafsheh, Gerold, Nas-taran, Marcus, Angela, Lydia, Sebastian, Maca, Fabio, Jan, Juan Andres, Balaji, and Rebekka for all the scientific discussions, hangouts, cinemas, food, football and beer together. Thanks also to my Fergusson (& associated) friends living in Germany (and Europe), Rohit, Pradyumna, Chaitanya, Sandesh, Abhijit, Mrunmayee, Indrajeet, Rishikesh, and Hemant for the travels and great time together. Special thanks also to my Melbourne friends, Monish, Neeraj, Anurag and Ajinkya for hosting me, and for making the two months in Melbourne memorable. I also want to thank all my friends from back in India, and all over the world. Special thanks to Behnam, Kostas and Vassilis, for the amazing time as IMRS student representatives, and discussions on IMPRS life and otherwise.

I also want to thank all the officemates I had, Peter, Behrang, Yasir, Daniel, Juan Andres (Juanito) and Rebekka. You were all amazing and helpful.

Most importantly, my deepest gratitude for my family: my parents, my sister, my brother-in-law, and my nephew, for their unconditional support always and especially during my PhD. Without their backing, I couldn't have come this far.

ERKLÄRUNG

Ich versichere, daß ich die von mir vorgelegte Dissertation selbständig angefertigt, die benutzten Quellen und Hilfsmittel vollständig angegeben und die Stellen der Arbeit -- einschließlich Tabellen, Karten und Abbildungen -, die anderen Werken im Wortlaut oder dem Sinn nach entnommen sind, in jedem Einzelfall als Entlehnung kenntlich gemacht habe; daß diese Dissertation noch keiner anderen Fakultät oder Universität zur Prüfung vorgelegen hat; daß sie -- abgesehen von unten angegebenen Teilpublikationen -- noch nicht veröffentlicht worden ist sowie, daß ich eine solche Veröffentlichung vor Abschluß des Promotionsverfahrens nicht vornehmen werde. Die Bestimmungen dieser Promotionsordnung sind mir bekannt. Die von mir vorgelegte Dissertation ist von Prof. Dr. Andreas Eckart betreut worden.

Köln, 07.09.2015

Teilpublikationen

Borkar, A., Eckart, A., Straubmeier, C., Kunneriath, D., Jalali, B., Sabha, N., Shahzamanian, B., García-Marín, M., Valencia-S, M., Sjouwerman, L., Britzen, S., Karas, V., Dovčiak, M., Donea, A., Zensus, A. (2016) Monitoring the Galactic Center with ATCA at 3mm. *Accepted to MNRAS*

Borkar, A., Eckart, A., Straubmeier, C., Kunneriath, D., Jalali, B., Sabha, N., Shahzamanian, B., García-Marín, M., Valencia-S, M., Sjouwerman, L., Britzen, S., Karas, V., Dovčiak, M., Donea, A., Zensus, A. (2016) SiO maser in the central parsec at 86 GHz *To be submitted to MNRAS*

Weitere Publikationen

Eckart, A., Britzen, S., Horrobin, M., Zamaninasab, M., Muzic, K., Sabha, N., Shahzamanian, B., Yazici, S., Moser, L., Zuther, J., Garcia-Marin, M., Valencia-S., M., Bursa, M., Karssen, G., Karas, V., Jalali, B., Vitale, M., Bremer, M., Fischer, S., Smajic, S., Rauch, C., Kunneriath, D., Moulataka, J., Straubmeier, C., Rashed, Y. E., Iserlohe, C., Busch, G., Markakis, K., Borkar, A., and Zensus, A. J. (2012). The Galactic Center as a paradigm for low-luminosity nuclei? What can be learned from SgrA* for the central engine and conditions of star formation in nuclei of Seyfert galaxies and low luminosity nearby QSOs; The K-band identification of the DSO/G2 source from VLT and Keck data. In *Proceedings of Nuclei of Seyfert galaxies and QSOs - Central engine & conditions of star formation (Seyfert 2012)*. 6-8 November, 2012. Max-Planck-Institut für Radioastronomie (MPIfR), Bonn, Germany. Online at <http://pos.sissa.it/cgi-bin/reader/conf.cgi?confid=169>, id.4, page 4.

Eckart, A., Horrobin, M., Britzen, S., Zamaninasab, M., Mužić, K., Sabha, N., Shahzamanian, B., Yazici, S., Moser, L., García-Marin, M., Valencia-S., M., Borkar, A., Bursa, M., Karssen, G., Karas, V., Zajaček, M., Bronfman, L., Finger, R., Jalali, B., Vitale, M., Rauch, C., Kunneriath, D., Moulataka, J., Straubmeier, C., Rashed, Y. E., Markakis, K., and Zensus, A. (2014). The infrared K-band identification of the DSO/G2 source from VLT and Keck data. In L. O. Sjouwerman, C. C. Lang, and J. Ott, editors, *IAU Symposium*, volume 303 of *IAU Symposium*, pages 269–273.

Eckart, A., Valencia-S., M., Shahzamanian, B., Garcia-Marin, M., Peissker, F., Zajaček, M., Parsa, M., Jalali, B., Saalfeld, R., Sabha, N., Yazic, S., Karssen, G. D., Borkar, A., Markakis, K., Zensus, J. A., and Straubmeier, C. (2015). The Center of the Milky Way from Radio to X-rays. *ArXiv e-prints*.

Jalali, B., Pelupessy, F. I., Eckart, A., Portegies Zwart, S., Sabha, N., Borkar, A., Moulataka, J., Mužić, K., and Moser, L. (2014a). Star formation in the vicinity of nuclear black holes: young stellar objects close to Sgr A*. *MNRAS*, **444**, 1205–1220.

Jalali, B., Pelupessy, F. I., Eckart, A., Portegies Zwart, S., Sabha, N., Borkar, A., Moulataka, J., Mužić, K., and Moser, L. (2014b). Young stellar objects close to Sgr

A*. In L. O. Sjouwerman, C. C. Lang, and J. Ott, editors, *IAU Symposium*, volume 303 of *IAU Symposium*, pages 144–146.

Moser, L., Eckart, A., Borkar, A., García-Marin, M., Kunneriath, D., Jalali, B., Sabha, N., Shahzamanian, B., Valencia-S., M., Zamaninasab, M., Bronfman, L., and Finger, R. (2014). Sgr A West in the light of molecules: cold and dense gas east of the circumnuclear disk. In L. O. Sjouwerman, C. C. Lang, and J. Ott, editors, *IAU Symposium*, volume 303 of *IAU Symposium*, pages 86–88.

Shahzamanian, B., Eckart, A., Valencia-S., M., Witzel, G., Zamaninasab, M., Sabha, N., García-Marín, M., Karas, V., Karssen, G. D., Borkar, A., Dovčiak, M., Kunneriath, D., Bursa, M., Buchholz, R., Moulataka, J., and Straubmeier, C. (2015). Polarized light from Sagittarius A* in the near-infrared K_s-band. *A&A*, **576**, A20.

Valencia-S., M., Eckart, A., Zajaček, M., Peissker, F., Parsa, M., Grosso, N., Mossoux, E., Porquet, D., Jalali, B., Karas, V., Yazici, S., Shahzamanian, B., Sabha, N., Saalfeld, R., Smajic, S., Grellmann, R., Moser, L., Horrobin, M., Borkar, A., García-Marín, M., Dovčiak, M., Kunneriath, D., Karssen, G. D., Bursa, M., Straubmeier, C., and Bushouse, H. (2015). Monitoring the Dusty S-cluster Object (DSO/G2) on its Orbit toward the Galactic Center Black Hole. *ApJ*, **800**, 125.

Lebenslauf

Persönliche Angaben

Name: Abhijeet Pramod Borkar
Anschrift: I. Physikalisches Institut, Universität zu Köln
Zülpicher Str. 77, 50937 Köln
Anschrift (privat): Bernhard Feilchenfeld Str. 13, Zollstock, 50969 Köln
Email: borkar@ph1.uni-koeln.de
Geburtsdatum und -ort: 27.05.1990 in Pune, Indien
Staatsangehörigkeit: Indien

Ausbildung und Berufserfahrung

2012 - 2015 Promotionstudent an der Universität zu Köln und dem
Max Planck Institut für Radioastronomie
wiss. Betreuer: Prof. Dr. Andreas Eckart
2010 - 2012 Master der Physik, Department of Physics,
University of Pune, Pune, Indien
wiss. Betreuer: Prof. Dr. Jayaram Chengalur,
NCRA-TIFR, Pune, Indien
Titel: "Relating Star Formation Rate in the Galaxies
with the Gas Distribution"
2007 - 2010 Bachelor der Physik, Fergusson College,
University of Pune, Pune, Indien
2005 - 2007 Higher Secondary School, Fergusson College, Pune, Indien
1999 - 2005 Secondary School, New English School Ramanbaug, Pune, Indien

Stipendium und Auszeichnungen

2012 - 2014 Stipendium der
International Max Planck Research School (IMPRS)
und der *Max Planck Institut für Radioastronomie (MPIfR)*,
an der Universität zu Köln
2014 - 2015 Stipendium der
Max Planck Institut für Radioastronomie (MPIfR),
an der Universität zu Köln

Datum

Unterschrift